TU TECHNISCHE UNIVERSITÄT WIEN
WIEN

DISSERTATION

Electrochemical stability of Li-ion conducting lithium lanthanum zirconate (LLZO) and lithium lanthanum titanate (LLTO) solid electrolytes

Ausgeführt zur Erlangung des akademischen Grades eines Doktors der Naturwissenschaften unter der Leitung von

Univ.-Prof. Dipl.-Phys. Dr. Jürgen Fleig

E164

Institut für Chemische Technologien und Analytik,

Fachbereich Elektrochemie,

der Technischen Universität Wien

Fakultät für Chemie

von

Dipl. Ing. Joseph Ring

Matrikelnummer 01268490

Maria-Lassnig-Straße 38/26

A-1100 Wien

Wien, am 25.01.2023

Abstract

Rechargeable Li-ion batteries have become essential energy storage devices for mobile applications. Especially for applications in electro-mobility, higher energy densities and better safety are demanded. Inorganic, solid state Li-electrolytes could pave the way towards Li-metal anodes and high voltage cathodes while being non-flammable. However, despite extensive research efforts over the last years, the integration of solid state Li-electrolytes into all solid state systems remains challenging. A detailed understanding of the electrochemical stability of solid state Li-electrolytes is key for the development of all solid state Li-ion batteries. The main goal of this work is to gain further insights into the limits of electrochemical stability of the solid state electrolytes $Li_{0.29}La_{0.57}TiO_3$ (LLTO) as well as $Li_7La_3Zr_2O_{12}$ (LLZO), and on the effects when exceeding these limits.

The electrochemical properties of LLTO were investigated using DC-techniques and electrochemical impedance spectroscopy (EIS) while polarizing the samples with ion-blocking electrodes. This stoichiometry polarization leads to a redistribution of Li inside LLTO and possibly also to additional reactions at the electrodes. Chemical changes resulting from this polarization were analyzed by laser ablation inductively coupled plasma mass spectrometry (LA-ICP-MS). A novel model was developed to describe the processes taking place beyond the stability limit of ca. 2.5 V. At the terminal with high Li chemical potential a coloration front appears, which indicates Li insertion and some enhanced electronic conductivity. At low Li chemical potentials, however, oxidation processes cause oxygen evolution and an effective Li_2O depletion in the LLTO phase. This decomposition process is rate limiting and probably involves oxygen ion transport in LLTO. Further, the ionic and electronic properties of LLTO were investigated at various states-of-charge (SOC) by means of EIS, galvanostatic intermittent titration (GITT), DC-conductivity measurements and chronoamperometry. Chemical Li-diffusion coefficients and electronic conductivities were calculated and the electron mobility was estimated. It was shown that an overlithiation

offset of about $\delta = 4 \cdot 10^{-4}$ per formula unit is required until significant electron conduction sets in and this is attributed to electron traps in the band gap, which first have to be filled before Ti^{3+} is formed. The corresponding electrolytic window ends at about 2.05 V vs. Li metal.

In the case of cubic LLZO, two aspects of the electrochemical stability were analyzed. First, the processes are studied taking place when polarizing a polycrystalline sample with two ion-blocking electrodes (analogous to the studies on LLTO). In-situ synchrotron X-ray diffraction (XRD) experiments were conducted to elucidate the structural changes of LLZO upon polarization. By means of transmission electron microscopy (TEM) and electron energy loss spectroscopy (EELS), further chemical and structural information about polarized LLZO samples was gathered. Second, the reactivity between LLZO and a highly important cathode material, namely $LiCoO_2$ (LCO), was studied by secondary ion mass spectrometry (SIMS). The kinetics of Co diffusion in LLZO at elevated temperatures was in the focus of this part. Here, it was essential to produce LCO thin films and a novel magnetron sputter device was built for this purpose. The processes of designing, fabricating and operating this sputtering device are shown. Technical peculiarities and details are provided, which may prove useful for researchers and engineers working on similar projects.

Kurzfassung

Sekundäre Li-Ionen-Batterien gehören zu den wichtigsten und meist eingesetzten mobilen Energiespeichern unserer Zeit. Besonders für Anwendungen in der Elektromobilität sind noch höhere Energiedichten, Laderaten und Sicherheit von großer Bedeutung. Anorganische, Festkörper-Li-Elektrolyte könnten der Schlussstein zur Anwendung von Li-Metall-Anoden zusammen mit Hochspannungskathoden in neuartigen Festkörper-Li-Ionen-Batterien sein. Zudem sind anorganische Festkörper nicht brennbar und somit den herkömmlichen, organisch basierten Li-Elektrolyten in puncto Sicherheit überlegen. Trotz der weltweit angestrengten Forschung vergangener Jahre ist die Implementierung von Festkörper-Li-Elektrolyten in galvanische Zellen problematisch. Detaillierte Informationen über elektrochemische Stabilität von anorganischen Festkörper-Li-Elektrolyten sind damit essentiell für die Entwicklung einer neuen Generation von Li-Ionen-Batterien. Diese Arbeit beschäftigt sich mit der elektrochemischen Stabilität der Festkörper-Elektrolyte $Li_7La_3Zr_2O_{12}$ (LLZO) und $Li_{0.29}La_{0.57}TiO_3$ (LLTO), sowie deren Grenzen und den Auswirkungen, wenn diese überschritten werden.

Die Auswirkungen auf die elektrochemischen Eigenschaften von LLTO unter elektrischer Feldbelastung mit ionen-blockierenden Elektroden wurden mittels DC-Techniken und elektrochemischer Impedanzspektroskopie (EIS) untersucht. Die angelegte Spannung führt dabei zu einer Stöchiometriepolarisation, also einer Umverteilung von Li im Material und eventuell auch zu weiteren Reaktionen an den Elektroden. Etwaige chemische Änderungen wurden mittels Laserablation-Massenspektrometrie (LA-MS) untersucht. Es wurde ein neuartiges Modell entwickelt, um die Prozesse zu beschreiben, die jenseits des Stabilitätslimits von ca. 2.5 V stattfinden. An der Elektrode mit hohem Li chemischen Potenzial erscheint eine dunkle Zone, die von einer erhöhten Li-Konzentration hervorgerufen wird und auch eine Erhöhung der elektronischen Leitfähigkeit zur Folge hat. Bei niedrigem Li chemischen Potenzial hingegen findet eine Oxitationsreaktions statt, die mit Sauerstoffentwicklung und formal mit einer Li_2O-Verarmung der LLTO Phase einhergeht. Darüber hinaus wurden die ionischen und elektronischen Eigenschaften von LLTO bei verschiedenen Ladezustände (SOC) mittels EIS, galvanostatischer intermittenter

Titration (GITT), DC-Leitfähigkeitsmessungen und Chronoamperometrie beleuchtet. So wurden chemische Li-Diffusionskoeffizienten und elektronische Leitfähigkeiten bestimmt und die Elektronenmobilität abgeschätzt. Es wurde gezeigt, dass eine Überlithiierung von mindestens $\delta = 4 \cdot 10^{-4}$ pro Formeleinheit überschritten werden muss, bevor signifikante Elektronenleitfähigkeit auftritt. Diese Untergrenze wird stark gebundenen elektronischen Zuständen zugeschrieben, die erst besetzt werden müssen bevor Ti^{3+} entstehen kann. Entsprechend dieser Konzentration an gebundenen Elektronen ist der Bereich, in dem LLTO als Elektrolyt benutzt werden kann, bei etwa 2.05 V gegen Li begrenzt.

Im Falle des kubischen LLZO wurden zwei Aspekte der elektrochemischen Stabilität untersucht. Erstens wurden die Prozesse, die bei Polarisation mit blockierenden Elektroden stattfinden, untersucht (analog zu den Arbeiten an LLTO). Es wurden in-situ am Synchrotron Röntgenbeugungsexperimente durchgeführt, um strukturchemische Änderungen zu beleuchten. Dann wurden ^{18}O-tracer-Austauschexperimente mit anschließender Sekundärionen-Massenspektroskopie (SIMS) durchgeführt, um Informationen über etwaige lokale Stöchiometrie Änderungen zu gewinnen. Transmissions-Elektronenmikroskopie (TEM) gekoppelt mit Elektronen-Energieverlust-Spektroskopie (EELS) wurde eingesetzt um weitere strukturelle und chemische Details zu beleuchten. Zweitens wurde die Stabilität zwischen LLZO und einem sehr wichtigen Kathodenmaterial, nämlich $LiCoO_2$ (LCO), mittels SIMS untersucht. Die Kinetik von Co – Diffusion in LLZO bei verschiedenen, hohen Temperaturen war hier im Fokus. Dazu war es erforderlich, LCO-Dünnschichten herzustellen. Zu diesem Zweck wurde eine neue Sputteranlage gebaut. Die Prozesse von Design, Fertigung, Aufbau und Inbetriebnahme dieser Sputteranlage sind im letzten Teil gezeigt. Technische Details, die hier beschrieben werden können sich für Forscher und Ingenieure mit ähnlichen Projekten als hilfreich erweisen.

INHALTSVERZEICHNIS

1 Introduction

It has become evident and generally accepted that renewable and sustainable energy is a necessity for a modern society. Challenges revolving around clean, reliable and sustainable energy are numerous and complex. Storage and distribution of renewable energy is one aspect of great importance, which stimulates diverse research efforts and technological development.

Energy storage is particularly challenging, when high energy densities are demanded, which is the case in mobility applications. Storing energy chemically, e.g. in hydrocarbons, can offer very high volumetric and gravimetric energy densities. However, conversion, storage and release of chemical energy is often non-trivial. Hydrogen is considered a suitable carrier of renewable energy, but poses its own set of problems, including a low volumetric energy density, a demand for a distribution infrastructure and limited energy efficiency during energy conversion.

Rechargeable batteries provide a very practical and efficient way of storing electrochemical energy. Especially when it comes to mobility applications, Li-ion batteries (LIB) seem promising due to their high energy density, efficiency and flexibility. Due to these properties, LIBs have revolutionized mobile electronics and electric vehicles. However, especially for the latter, vital safety issues are yet to overcome. These are primarily related to the flammability of organic based electrolytes, which are predominantly used in LIBs today. Consequently, alternatives to these classic, organic electrolytes are required. Inorganic solids (e.g. oxides) are typically inflammable and mechanically stable. Provided a high Li-ion conductivity and negligible electron conductivity, this could make inorganic solids ideal candidates for a safer new generation of LIBs.

Beside high Li-ion and low electron-conductivity, electrochemical stability is a key requirement for a Li-electrolyte. The combination of high reductive and oxidative stress at the different terminals is the fundamental principal of energy storage and is directly related to the voltage of the battery. However, the electrochemical stability of an electrolyte against reduction and oxidation limits the voltage of the used anode and cathode, respectively.

Consequently, the voltage of the galvanic cell is limited by the difference between the oxidative and reductive stability limits, the so-called electrochemical stability window. For a cell arrangement to be thermodynamically stable, the electrode voltages must not exceed this electrochemical stability window. This compatibility requirement poses a great challenge for possible solid state Li-electrolyte materials.

The compatibility of electrolyte and electrode materials can be described by means of the Li chemical potential μ_{Li}. Considering basic thermodynamics, Li seeks a state of lowest possible μ_{Li}. Consequently, when a material A has vacant Li-states with lower μ_{Li} than the μ_{Li} of occupied states of an adjacent material B, there is a thermodynamic driving force for Li-transfer from A to B. Please note that Li-states usually consist of the combination of Li ion sites and electronic states, e.g. at transition metals (e.g. Co^{3+}/Co^{4+}). Furthermore, if the involved phases can be rearranged into new phases with lower μ_{Li}, a reaction is thermodynamically favorable. Thermodynamic stability windows of common solid Li-electrolytes are shown in Figure 1a[1].
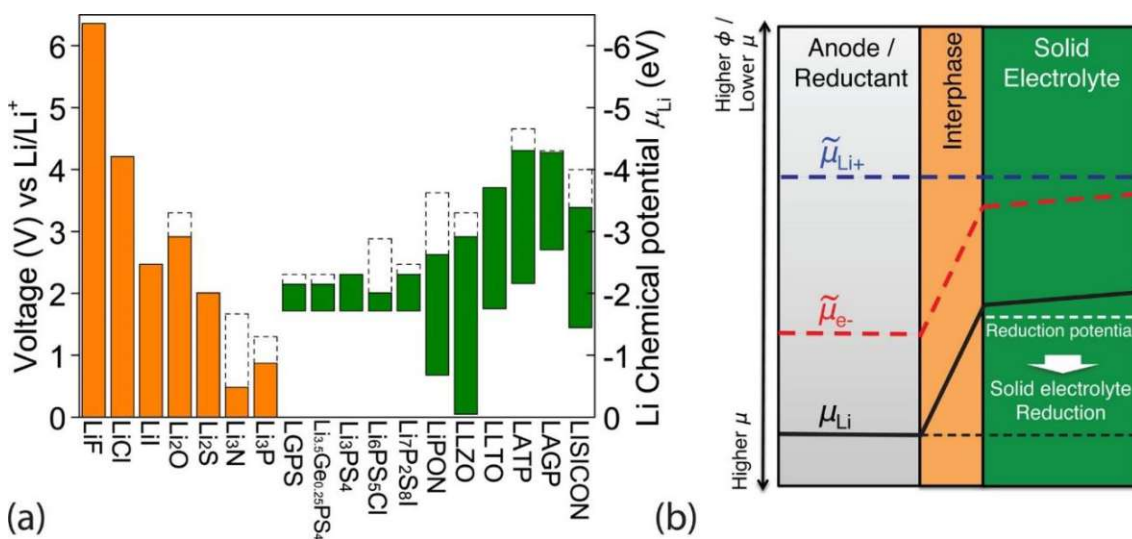

Figure 1: (a) Electrochemical window (solid color bar) of solid electrolytes and other materials. The oxidation potential to fully delithiate the material is marked by the dashed line. Orange bars indicate binary compounds, while green bars indicate non-binary materials. While binary compounds are all stable against Li metal (i.e. 0 V), low oxidative stability and/or low ionic conductivity holds them back as suitable electrolytes. (b) Schematic diagram about the change of Li chemical potentials μ_{Li} (black line), the electrochemical potential of Li-ions $\tilde{\mu}_{Li+}$ (blue dashed line), and of electrons $\tilde{\mu}_{e-}$ (red dashed line) across the interface between the anode and the solid

electrolyte. Since the actual profile of $\tilde{\mu}_{e^-}$ determined by the charge carrier distribution may be complicated, the profiles of chemical and electrochemical potential shown here are schematic and may not be linear. The vertical scale is for the electrostatic potential or the voltage referenced to Li metal and is reversed for the chemical potential or electrochemical potential. Reproduced with permission of the copyright owner[1].

The chemical potential of neutral Li μ_{Li} can be described by the sum of the chemical potentials of Li-ions and electrons, μ_{Li+} and μ_{e-}. These chemical potentials of Li$^+$ and e$^-$ are further affected by the electrostatic potential φ, which is combined in the electrochemical potentials $\tilde{\mu}_{Li+}= \mu_{Li+}+\mathcal{F}\varphi$ and $\tilde{\mu}_{e-}= \mu_{e-}-\mathcal{F}\varphi$. Since all materials integrated in a LIB should have high Li-ion conductivities, $\tilde{\mu}_{Li+}$ is often considered close to constant, since any gradient of $\tilde{\mu}_{Li+}$ would result in a migration of Li$^+$ to equalize the gradient. Since $\mu_{Li}=\tilde{\mu}_{Li+}+\tilde{\mu}_{e-}$ and $\tilde{\mu}_{Li+}$ is considered constant, many aspects can be discussed by considering only differences in $\tilde{\mu}_{e-}$. Since $\tilde{\mu}_{e-}$ is influenced by electric fields as well as chemically, electric bias can be used to precisely tune the local $\tilde{\mu}_{e-}$ of any electrolyte material.

This leads to a powerful experimental tool for the investigation of electrochemical stability windows. If a bias, exceeding the width of the stability window, is applied to an electrolyte, electrochemical decomposition, i.e. oxidation at the anodic terminal and reduction at the cathodic terminal, becomes thermodynamically favorable. Naturally, if chemically inert electrodes (e.g. Au, Pt) are used, the decomposition of the electrolyte only involves phase transitions of its constituents.

Thermodynamic data, however, only reflect equilibrium states and does not account for possible kinetic barriers of decomposition reactions. At room temperature, which is the usual operating temperature of Li-ion batteries, crystallization of new (decomposition) phases is often held back by activation barriers. This can extend the stability of an electrolyte material beyond its thermodynamic limits, therefore experimental data about empirical stability windows is essential.

Further, if decomposition phases do not have sufficient electronic and/or ionic conductivity, they can form a meta-stable interface and prevent further decomposition by changing the locally relevant Li chemical potential. This is sketched in Figure 1b for a solid electrolyte in contact with an anode material of high μ_{Li}. On the other hand, if an interface between

electrolyte and electrode has a low ionic conductivity, it poses a kinetic barrier for charge/discharge processes, thus increasing the internal resistance of the cell. Since the formation and quality of interface layers is of such great importance, experimental data is essential for the application of solid state electrolytes.

Ideally, an electrolyte is both compatible with low-voltage anodes (such as Li-metal → 0 V) and high-voltage cathodes (such as $LiNi_{1-x-y}Mn_xCo_yO_2$ → 4.5 V). Oxides may exhibit a particularly high stability against oxidation (> 4 V [2]) as well as high Li-ion conductivities (>1 mS/cm) [3]. The garnet-type electrolyte $Li_7La_3Zr_2O_{12}$ (LLZO) is especially interesting with Li-ion-conductivities ranging from 10^{-4} up to 10^{-3} S/cm, while also being (meta-)stable against Li-metal, possibly enabling Li-metal anodes [1,4–13]. The questions and problems of the compatibility with Li-metal are subject of extensive research efforts[14–21].

The stability of LLZO towards high voltage cathodes, however, is less investigated. According to DFT calculations, the thermodynamic stability window of LLZO ranges only up to 3-3.3 V vs. Li^0 [1,22], whereas experimental studies with ion blocking electrodes report a stability window up to 5-6 V vs Li^0 [12]. Recent studies have shown that LLZO undergoes electrochemical decomposition when voltages above 2 V are applied between Li-blocking Au-electrodes at 300 °C[23]. At the positive electrode, release of oxygen gas alongside with Li depletion takes place. Subsequent structural instability results in the formation $La_2Zr_2O_7$ and La_2O_3. At the negative electrode, Li-ions and electrons react with the atmosphere forming Li-salts such as LiOH, Li_2O or Li_2CO_3. Prior to the structural collapse of LLZO and crystallization of $La_2Zr_2O_7$ and La_2O_3, intermediate Li-deficient phases at the anode may play a role in the decomposition mechanism. However, investigations of such intermediates by in-situ experiments (such as XRD) remain to be done.

Also the A-site deficient perovskite $Li_{0.29}La_{0.57}TiO_3$ (LLTO) has a high Li-conductivity (>0.1 mS/cm[24]) and is stable up to 4.2 V[25]. In contrast to many other Li-ion conducting materials like thiosulfates or garnets, LLTO is usually considered chemically stable in ambient conditions. Nonetheless, the thermodynamically stable potential range is limited, and first-principles calculations predict an electrochemical stability window of 1.75-3.7 V vs. Li metal[1,26,27]. Consequently, application of more than 2 V bias may result in electrochemical decomposition. These first-principles calculations predict O_2 evolution and formation of

La$_2$Ti$_2$O$_7$ and Li$_4$Ti$_5$O$_{12}$ at the anode, whereas Li-rich phases that contain Ti^{3+}, like Li$_7$Ti$_{11}$O$_{24}$, La$_2$Ti$_2$O$_7$ and Li$_4$Ti$_5$O$_{12}$ are suggested as the most stable phases at the cathode.

The practically usable potential window may be larger, particularly when the kinetics of electrolyte decomposition is sluggish (which is expected for processes that involve movement of La and Ti ions at room temperature). On the other hand, also within the phase stability window of the electrolyte, an increase of the electron or electron hole concentration may lead to a breakdown of the electrolytic domain, when the ionic transference number drops significantly below one. Hence, the mentioned calculations can only serve as a rough guidance for the real operational potential window of LLTO, and additional experimental studies are required to understand the practical stability window which limits the applicability in real devices.

Some discrepancy is between thermodynamic calculations and experimental data are already known. For example, experiments showed that LLTO does not decompose, when subjected to Li potentials lower than 1.7 V vs. Li, but rather reversibly inserts Li into vacant A-sites[28,29] or even interstitial 3c sites at potentials lower than 1.2V vs. Li metal[29,30]. Due to the charge compensation by conduction band electrons, the material thereby becomes a mixed ionic electronic conductor (MIEC) and behaves then more like an electrode material than as an electrolyte. Li can be reversibly incorporated until full occupancy of the A-site is reached at potentials as low as 1.2 V[28]. During Li insertion, charge neutrality is preserved primarily by the reduction of Ti^{4+} to Ti^{3+}, since the conduction band of LLTO has predominant Ti-3d character. Indeed, experimental studies confirmed the change of Ti^{4+} to Ti^{3+} in LLTO upon reduction via in-situ XPS[31]. Accordingly, LLTO does not undergo phase decomposition below 1.7 V, but is disabled as an electrolyte nonetheless, since it becomes an electronic conductor. This overlithiation process is usually not included in thermodynamic and first-principles calculations on stability limits. The oxidative stability limit of LLTO is less investigated. However, it was demonstrated that LLTO can improve the stability of the cathode material LiNi$_{0.8}$Co$_{0.15}$Al$_{0.05}$O$_2$, enhancing cycling performance and charge transfer kinetics at potentials up to 4.2 V[25]. This indicates that the operational oxidative stability window is also larger than suggested by thermodynamic calculations.

The processes upon voltage load may be limited by chemical Li-diffusion and the chemical diffusion coefficient $\widetilde{D}$ can be obtained from galvanostatic intermittent titration technique

(GITT) measurements[28]. Under certain conditions, $\widetilde{D}$ can also be calculated from electrochemical impedance (EIS) data[32]. Throughout the stoichiometry range (from $\delta=0$ to $\delta=0.14$), $\widetilde{D}$ -values of $Li_{0.29+\delta}La_{0.57}TiO_3$ change by less than one order of magnitude[28]. However, there are no detailed reports about the electronic conductivity of LLTO at various degrees of reduction.

Not only the thermodynamic stability of electrolytes at room temperature is crucial, but also manufacturing conditions of solid state cells have to be considered. In order to obtain an interface between solid state electrolytes and electrode materials with sufficient physical content, sintering is a commonly applied technique. Another way to reach this goal is to directly coat one material onto the other by deposition techniques, such as pulsed-laser deposition (PLD), sputtering or chemical vapor deposition (CVD). While sintering requires high temperatures (800-1600 °C) to enable reasonable mass transport, deposition techniques require elevated temperatures (typically 300-800 °C) to ensure the formation of the desired crystalline phase. Either way, these heat treatments can lead to undesired cross-diffusion between the materials[33–35], thus forming phases with low Li-conductivity at the interface.

The goal of this PhD thesis was to further investigate the (electro-)chemical stability of LLTO and LLZO and to understand the processes taking place beyond the electrolytic domain boundary or outside the electrochemical stability window. A main approach was to polarize the solid state Li-electrolytes by two ion-blocking electrodes and to investigate the resulting phenomena by electrochemical tools (DC- and AC-techniques, i.e. electrochemical impedance spectroscopy, galvanostatic titration, spatially resolved Li activity measurements), optically (movement of color fronts), by synchrotron XRD studies and by laser ablation inductively coupled plasma mass spectroscopy (LA-ICP-MS).

In Chapter 2, the main focus is laid on the processes taking place in polarized LLTO. The cathodic breakdown mechanism was investigated primarily by the observation of an electrocoloration front under DC load, spatially resolved Li activity measurements and localized conductivity measurements. The spatially more confined Li depletion next to the anode was more closely investigated by synchrotron XRD studies and laser ablation inductively coupled plasma mass spectroscopy (LA-ICP-MS) for measuring changes in the local Li stoichiometry induced by DC bias. It is shown that a very strongly Li depleted zone

is formed directly under the anode, while at the cathode a very broad, but only slightly Li enhanced colored region develops. In Chapter 3, the transition of LLTO from a Li-conducting electrolyte to a mixed conductor is considered in more detail. Galvanostatic titration and impedance spectroscopy are used to determine the electronic conductivity, the ionic transference number and the Li chemical diffusion coefficient as a function of δ in $Li_{0.29+\delta}La_{0.57}TiO_3$. Owing to the absence of structural transformations during the Li insertion up to δ=0.14, LLTO proves to be an excellent model material for such investigations.

Chapter 4 and Chapter 5 deal with the stability of LLZO. In Chapter 4, the effect of electric field stress on LLZO using Li-blocking electrodes was analyzed by various ex-situ (including XRD, SIMS, TEM and EELS) and in-situ experiments (XRD), revealing details about the decomposition at the oxidative electrode. The heat-induced reaction between LLZO and a cathode material was investigated with the widely-used cathode material $LiCoO_2$ (LCO). So far, only some preliminary results are available, showing that Co is incorporated into, and transported through LLZO at surprisingly high rates. The reactions between LLZO and LCO thin films at elevated temperatures were investigated by SIMS (see Ch. 5). In Chapter 6, the process of building a sputtering device for deposition of LCO is shown.

2 Electrochemical stability window and electrolyte breakdown mechanisms of Li-ion conduction $Li_{0.29}La_{0.57}TiO_3$

2.1 Abstract

Perovskite-type $Li_{0.29}La_{0.57}TiO_3$ (LLTO) is a promising solid electrolyte material with a high Li-ion conductivity. However, its experimental electrochemical stability window is not well established and thus the compatibility with potential electrode materials is partly unclear. In this contribution, we present results from electrochemical and analytical experiments to elucidate the stability of LLTO when being polarized with Li-ion-blocking Pt electrodes. For voltages above ca. 2.4-2.5 V, a darkened color front starts moving from the cathode to the anode and marks decomposition of the electrolyte. The electrochemical phenomena occurring at the two electrode interfaces during this electrocoloration are discussed in detail. Instead of the thermodynamically predicted decomposition phases, we find zones in LLTO with modified defect chemical properties. In the partly very broad electrocoloration zone originating at the cathode, the high mobility of electronic charge carriers leads to a mixed ion-electron conductivity and a very small Li excess concentration. Next to the anode, a spatially very confined, weakly conductive Li depletion zone forms. Oxygen evolution rather than electron hole formation dominates the corresponding anodic reaction. Ion transport in this zone also causes most of the kinetic overpotential during electrocoloration, supposedly via slow oxygen vacancy transport. This very confined but strong Li depletion in the anodic zone could be quantified by analytical laser ablation inductively coupled plasma mass spectrometry (LA-ICP-MS) and was correlated with the charge measured in the electrical experiments.

2.2 Introduction

Lithium lanthanum titanate (LLTO) is a promising Li-ion conducting solid electrolyte for Li-ion batteries, due to its high bulk Li-ion conductivity in the range of almost 10^{-3} S/cm[36–41]. It is a weakly distorted tetragonal perovskite-type material with pronounced A-site cation disorder[42–46]. The A-sites are partially occupied by Li^+, La^{3+} and vacancies. The average charge of the A-site cations must be 2+, so the general A-site occupancy in LLTO is $La_{0.666-x}Li_{3x}TiO_3$, which yields 0.333-2x A-site vacancies per formula unit. Compositions around x = 0.1 ($La_{0.57}Li_{0.29}TiO_3$) have the highest Li-ion conductivity by a vacancy hopping mechanism.

In contrast to many other Li-ion conducting materials like thiosulfates or garnets, LLTO is usually considered chemically stable in ambient conditions and even in water. This enables application e.g. in lithium-air batteries, or lithium extraction from aqueous sources like seawater[47,48]. Nonetheless, the thermodynamically stable potential range is limited, and first-principles calculations predict an electrochemical stability window of 1.75-3.7 V vs. Li metal[1,26,27]. Consequently, application of more than 2 V bias may result in electrochemical decomposition. These first-principles calculations predict O_2 evolution and formation of $La_2Ti_2O_7$ and $Li_4Ti_5O_{12}$ at the anode, whereas Li-rich phases that contain Ti^{3+}, like $Li_7Ti_{11}O_{24}$, $La_2Ti_2O_7$ and $Li_4Ti_5O_{12}$ are suggested as the most stable phases at the cathode.

The practically usable potential window may be larger, particularly when the kinetics of electrolyte decomposition is sluggish (which is expected for processes that involve movement of La and Ti ions at room temperature). On the other hand, also within the phase stability window of the electrolyte, an increase of the electron or electron hole concentration may lead to a breakdown of the electrolytic domain, when the ionic transference number drops significantly below one. Hence, the mentioned calculations can only serve as a rough guidance for the real operational potential window of LLTO, and additional experimental studies are required to understand the practical stability window which limits the applicability in real devices.

Some discrepancy is between thermodynamic calculations and experimental data are already known. For example, experiments showed that LLTO does not decompose, when subjected to Li potentials lower than 1.7 V vs. Li, but rather reversibly inserts Li into vacant

A-sites[28,29] or even interstitial 3c sites at potentials lower than 1.2V vs. Li metal[29,30]. Due to the charge compensation by conduction band electrons, the material thereby becomes a mixed ionic electronic conductor (MIEC) and behaves then more like an electrode material than as an electrolyte. Li can be reversibly incorporated until full occupancy of the A-site is reached at potentials as low as 1.2 V[28]. During Li insertion, charge neutrality is preserved primarily by the reduction of Ti^{4+} to Ti^{3+}, since the conduction band of LLTO has predominant Ti-3d character. Indeed, experimental studies confirmed the change of Ti^{4+} to Ti^{3+} in LLTO upon reduction via in-situ XPS[31]. Accordingly, LLTO does not undergo phase decomposition below 1.7 V, but is disabled as an electrolyte nonetheless, since it becomes an electronic conductor. This overlithiation process is usually not included in thermodynamic and first-principles calculations on stability limits. The oxidative stability limit of LLTO is less investigated. However, it was demonstrated that LLTO can improve the stability of the cathode material $LiNi_{0.8}Co_{0.15}Al_{0.05}O_2$, enhancing cycling performance and charge transfer kinetics at potentials up to 4.2 V[25]. This indicates that the operational oxidative stability window is also larger than suggested by thermodynamic calculations.

In this study, electrochemical experiments are performed on LLTO polycrystals with Li-ion-blocking Pt electrodes to investigate the electrochemical phenomena taking place under voltage load, to determine the practical electrochemical stability limits and to explore the reactions taking place in/at LLTO when exceeding these limits. The cathodic breakdown mechanism was investigated primarily by the observation of an electrocoloration front under DC load, spatially resolved Li activity measurements and localized conductivity measurements. The spatially more confined Li depletion next to the anode was more closely investigated by synchrotron XRD studies and laser ablation inductively coupled plasma mass spectroscopy (LA-ICP-MS) for measuring changes in the local Li stoichiometry induced by DC bias. It is shown that a very strongly Li depleted zone is formed directly under the anode, while at the cathode a very broad but only slightly Li enhanced colored region develops.

2.3 Experimental

A large polycrystalline LLTO-sheet (0.5 mm thick) with nominal stoichiometry $Li_{0.29}La_{0.57}TiO_3$ was used for sample preparation (Toho Titanium Co., Ltd., Japan). Rectangular samples, with typical dimensions 5x12 mm², were prepared by cleaving. Li-blocking Pt electrodes (200 nm thick) were deposited onto the sample surface by magnetron sputtering (Baltec Med 020) at room temperature, unless noted otherwise. Potentiostatic field-stress was applied to samples using platinum needles and a Keithley 2611B Source-Meter-Unit, which was also used to measure open circuit voltages (OCVs). Different sample and electrode geometries were employed in various types of experiments. This is sketched in Figure 2. In experiment type I, voltages of 1-20 V were applied between stripe electrodes (ca. 2 mm wide) and time-dependent currents as well as appearance and movement of a color front were measured. In experiment type II (see Figure 2), the voltage was applied between an extended counter electrode and a small circular working electrode (800 μm in diameter). After a certain time, the external load was removed and the OCV was measured between the working electrode and another small circular electrode in some distance. Moreover, impedance spectra were measured with a Novocontrol Alpha-A High Performance Frequency Analyzer (Novocontrol Technologies GmbH & Co. KG, Germany), between several electrode pairs to get information on the corresponding local conductivity. This coloration and characterization sequence was reported several times. Both types of experiments were conducted in an evacuated ($p<10^{-5}$ mbar) sample chamber at room temperature, unless otherwise described.

The local chemical composition of LLTO after voltage load was measured by laser ablation inductively coupled plasma mass spectrometry (LA-ICP-MS). An excimer-based laser ablation system (ESL193, Elemental Scientific Lasers, United States) was used which utilizes argon, fluorine and helium (buffer gas) as laser medium and operates at a wavelength of 193 nm in the UV range. Laser pulses with durations of nanoseconds were produced by this LA instrument. The laser was controlled via the software "Active View 2", which had been delivered together with the instrument. As ablation chamber an analytical cup (TwoVol2, Elemental Scientific, United States) was used. As ICP-MS device (iCAP Q, ThermoFisher Scientific, Germany) equipped with a quadrupole mass analyzer was employed. The data evaluation was conducted by the software "Qtegra". The connection between the LA device

and the ICP-MS instrument was achieved by using a polymeric tube (Tygon®, inner diameter: 1.6 mm) and a dual concentric injector (DCI, Elemental Scientific, United States). All operating parameters are summarized in Table 1. In the corresponding experiment type III two circular electrodes (1 mm diameter) were sputtered on small (ca. 2x6 mm^2) LLTO sheets and polarized in vacuum (10^{-5} mbar) at 100-150 °C. Samples were polarized at 4-8 V for up to 90 minutes. LAMS measurements were performed ex-situ after polarization (see sketch in Figure 2).

Table 1: Operating parameters of the LA- and ICP-MS instruments.

Laser ablation		Inductively coupled plasma mass spectrometry	
Laser fluence	1.25 J cm^{-2}	RF power	1550 W
Beam size	20 µm	Auxiliary gas flow	0.80 mL min^{-1}
Repetition rate	100 Hz	Cool gas flow	14.0 mL min^{-1}
Overlap	10 µm	Nebulizer gas flow	0.72 L min^{-1}
Scan speed	1000 µm s^{-1}	Dwell time per mass	10 ms
He flow	800 mL min^{-1}	Measured isotopes	^{6}Li, ^{46}Ti, ^{138}La
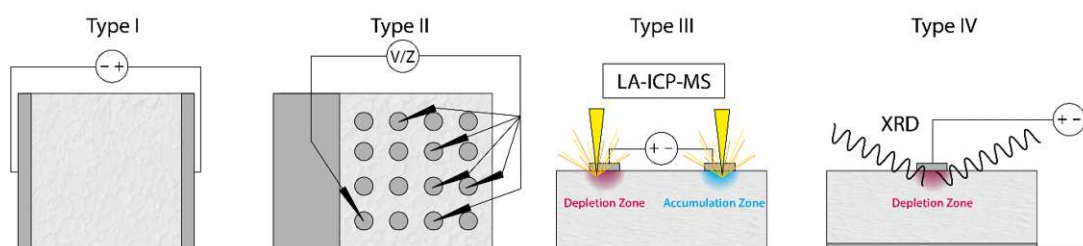
Figure 2: Sketches of the experimental setups: 2-electrode electrocoloration (Type I), recording current over time; multiple electrode coloration (Type II), where OCVs and impedance spectra of multiple electrodes were measured repeatedly during electrocoloration; LA-ICP-MS depth profiles of field-stressed LLTO samples (Type III) and in-situ micro focused XRD (Type IV).

Experiment type IV was performed at the synchrotron DESY, beamline P08. Therein, a highly collimated (30x30 μm) X-ray spot with 11.8 keV was focused on a Au electrode in shallow incidence (5° angle of incidence) mode, which results in a mean X-ray penetration depth of 2 μm. Diffraction patterns were collected by movement of a 2-d detector (Pilatus100K, 195x487 pixels) along the Θ axis at constant angle of incidence.

2.4 Electrocoloration of LLTO

In experiments of type I (cf. sketch in Figure 2), LLTO sheets with Li-ion blocking Pt electrodes were subjected to a DC voltage at room temperature inside a vacuum chamber with a base pressure of 10^{-5} mbar. Above a bias voltage of about 2.4-2.5 V a colored zone appears at the cathode and propagates towards the anode. The intensity of the colored zone increases with voltage. As an example, the movement of a color front is shown in Figure 3a-d for an applied potential of 5 V; the corresponding current is given in Figure 3f. The velocity of the color front decreases with time, as can be seen by the time-dependent location of the color front plotted in Figure 3f. However, such coloration of LLTO is only observed in an oxygen-, CO_2- and moisture-free environment like a glove-box or vacuum chamber pumped by a turbo molecular pump. Once a colorized sample is exposed to air, the color disappears (see Figure 3e). It is also remarkable that, in contrast to electrocoloration experiments on $SrTiO_3$[49], no color front originates at the anode. Rather, the cathodic color front appears to reach the anode of the sample, which suggests that only a spatially very confined zone with changed properties exists at the cathode. Experiments of type III and IV in Figure 2 deal with the properties of this anodic zone. Please note that we use the terms "anode" and "cathode" with their common electrochemical meanings, i.e. representing an oxidation reaction (anode) or a reduction (cathode) in our LLTO sample. In terms of Li chemical potential, the cathode is thus much closer to Li metal than the anode.

The electrical characteristics of experiments with voltages from 1 to 20 V is shown in Figure 4a. Figure 4b displays the voltage dependent currents after 100 and 300 seconds, respectively. Already between 1 V and 2 V, we find a non-linearity of the current. However, from 2 to 3 V the current increase is very pronounced (factor of 27 at 100 s), suggesting that something changes qualitatively at such voltages, and indeed this is the voltage range,

where the visible color front appears. Moreover, at high voltages we find a current minimum after some time and this minimum coincides with the time needed by the visible color front to pass the entire sample and to reach the anode. The different times of the minimum (5 V: 2700 seconds, 20 V: 520 seconds, see Figure 4a) also show that the velocity of the color front increases with voltage.
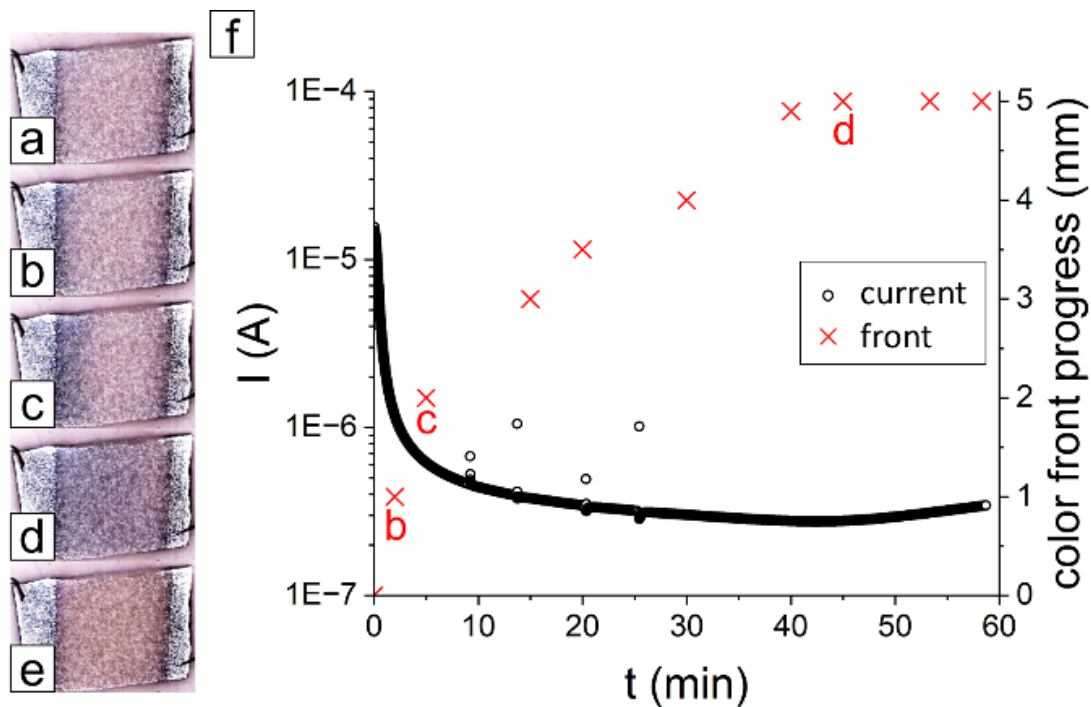

Figure 3: Photographs of the LLTO sample before (a) and during (b-d) an electrocoloration at 5 V. After complete coloration, air was introduced to the sample chamber (e). Panel (f) shows the current over time (black circles, left axis) and the progression of the coloration front (red crosses, right axis), with times corresponding to (b-d) marked by red letters. The current shows a minimum at approximately 45 minutes, when the coloration front reaches the anodic terminal, as shown in photograph (d).

It is well known that DC experiments on mixed conducting materials with blocked majority charge carrier lead to a so-called stoichiometry polarization[50,51]. In case of a predominantly ion conducting material with blocked ion transport at the electrodes, a redistribution of ions takes place with depletion on one side and accumulation on the other. Both concentration changes are accompanied by corresponding changes of electronic charge carrier

concentrations. For two blocking electrodes this was described by Yokota or Miyatani [52,53], while for one reversible and one blocking electrode we refer to it as Hebb-Wagner experiments[54,55]. In such measurements the ionic current decreases towards zero and finally only the electronic current remains.

It is thus reasonable to assume that at low voltages stoichiometry polarization also takes place in LLTO, i.e. Li accumulation at the cathode (via Li-ions and electrons) and Li depletion at the anode (via additional Li vacancies and holes). However, the Li concentration changes are very small, due to the very small intrinsic concentration of electronic defects in LLTO. Consequently, the DC current continuously decreases with time to very small values, see Figure 4. For higher voltages, on the other hand, and particularly above the electrochemical stability window, further processes come into play during the voltage-driven Li redistribution and those are in the focus of our study. First, we consider the extended coloration front that emerges from the cathode. This has to be related to Li accumulation (as in a Hebb-Wagner experiment).

Table 2: Experimental data from polarizations with 1-20 V, including the estimated coloration zone volumes and corresponding Li-excess, calculated via integration of current over time.

U (V)	t (s)	Q (C)	$V_{colored\ zone}$ (mm³)	$\Delta nLi^+/V_{colored\ zone}$ (mol/cm³)	$\Delta nLi^+_{colored\ zone}$ (p.f.u)
1	300	$1.6 \cdot 10^{-6}$	0	no coloration	no coloration
2	300	$8.2 \cdot 10^{-6}$	0	no coloration	no coloration
3	300	$1.8 \cdot 10^{-4}$	1.6	$1.2 \cdot 10^{-6}$	$4.4 \cdot 10^{-5}$
5	300	$6.3 \cdot 10^{-4}$	2.9	$2.3 \cdot 10^{-6}$	$8.4 \cdot 10^{-5}$
20	300	$1.7 \cdot 10^{-3}$	8.0	$2.2 \cdot 10^{-6}$	$8.3 \cdot 10^{-5}$

When we assume that the current in the uncolorized zone of the LLTO sheet is primarily ionic, which is reasonable as long as the current minimum is not reached, we may determine the amount of Li-ions accumulated in the reduced zone (and thus removed from the

oxidized zone). This was done by integrating the current over time plotted in Figure 4, and values for several voltages and times are summarized in Table 2. From this calculation we can conclude that the Li-excess in the colorized zone is very small and in the order of $<10^{-4}$ per formula unit (p.f.u), which is much smaller than the concentration of vacant A-sites (0.14 p.f.u.). The charge of these additional Li-ions is at least partly compensated by the reduction of Ti^{4+} to Ti^{3+}, and this introduces mixed ion and electron conductivity, as already suggested from previous studies on the electrochemical and thermal reduction of LLTO[31,56]. The high speed of the coloration front propagation indicates high mobility of these electronic carriers.
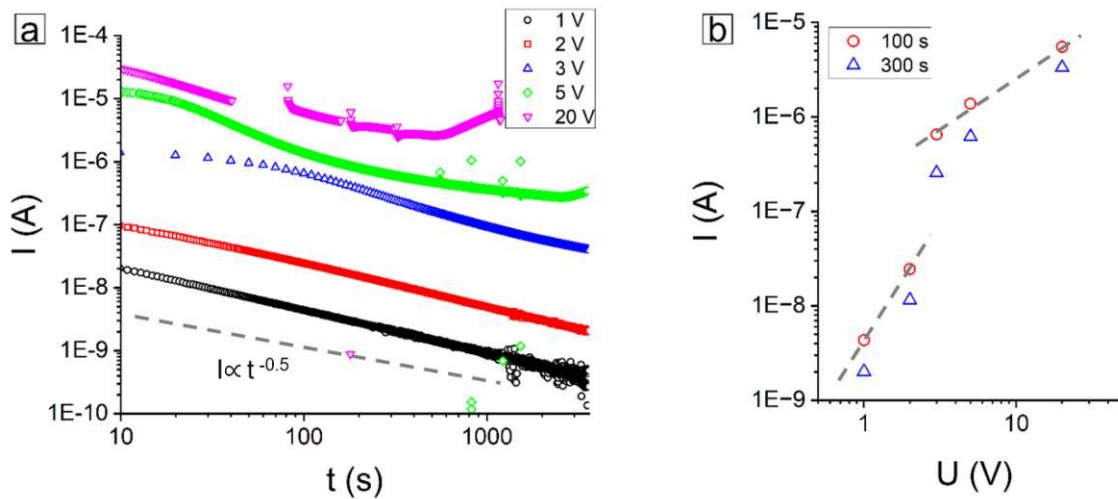
Figure 4: (a) Current over time of various electrocoloration experiments. At 1 V and 2 V no coloration is apparent at all. At 3 V the coloration front is very slow and does not reach the anodic terminal during the course of the experiment. At 5 V and 20 V the current shows a minimum when the coloration front reaches the anodic terminal. (b) Current with respect to voltage at 100 s (red circles) and 300 s (blue triangles). Between 2 V and 3 V, a drastic increase of current is apparent, whereas a further voltage increase to 5 V and 20 V shows less changes.

2.5 Local Li chemical potentials and conductivities during electrocoloration

To further investigate the mechanisms behind the electrocoloration, multiple small electrodes were used in experiment type II (see Figure 2) to probe electrochemical properties at various sample positions and different times. Herein, a constant voltage of 5 V was applied between a large rectangular anode (CE) ($\sim$30 mm^2) and a small circular cathode (WE) (850 μm diameter) as shown in Figure 5a. In this configuration, the coloration front propagates almost concentrically around the circular cathode. The bias load was paused after several minutes and open circuit voltages (OCVs) were measured between various circular electrodes and a reference electrode outside the colored zone. Then, the electrocoloration process was continued. This procedure was repeated several times. In order to get also information on the conductivity changes during electrocoloration, impedance spectra were measured between different circular electrodes before and after coloration, shown in Figure 5b. These exhibit an incomplete high frequency feature, an x-axis intercept at ca 25 kΩ, and a low frequency feature that is associated with the ion blocking electrodes. The real axis intercept resistance represents the charge transport resistance of LLTO and corresponds to a total conductivity of roughly $5\cdot10^{-4}$ S/cm, according to the spreading resistance equation. This is in line with the ionic conductivity according to the manufacturer's statement and own measurements with co-planar electrodes (not shown).
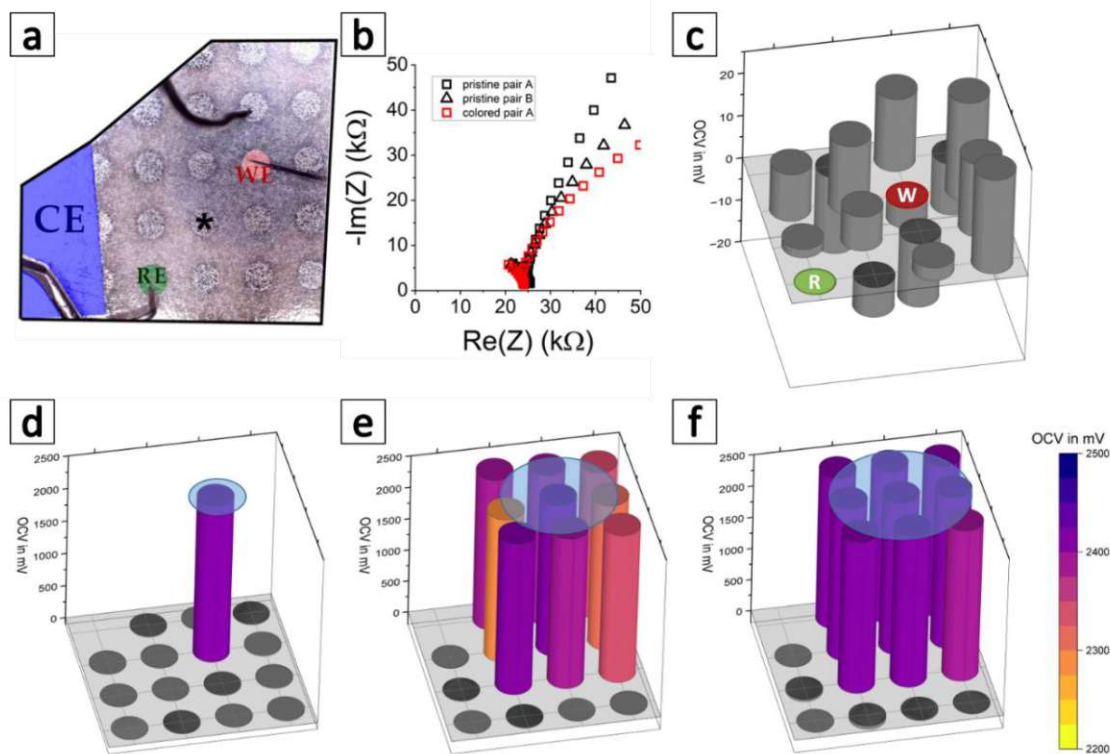
Figure 5: Electrocoloration experiment with multiple electrodes. (a) Experimental setup, after 52 minutes of coloration with 5 V. The working (WE) and counter (CE) electrodes are marked red and blue, respectively. The circular electrode marked green (RE) was used as a reference electrode to determine OCVs of various circular electrodes repeatedly. (b) Impedance spectra of neighboring circular electrode pairs. Black squares and triangles indicate the impedance response prior to coloration, whereas the red squares indicate the impedance response after both electrodes were within the coloration zone. The electrode pair "A" is marked by (*) and (WE) in panel (a). (c) shows the OCVs of various circular electrodes before electrocoloration was started. All OCVs were measured with respect to the reference electrode marked green. (d-f) shows the development of OCVs over the course of the coloration experiment. The progression of the coloration front is indicated as a blue overlay.

Remarkably, this resistance does not change after coloration, indicating that the total conductivity remains the same and any electronic conductivity introduced by the coloration is still significantly lower than the ionic conductivity. A virtually unchanged ionic conductivity during overlithiation is also in accordance with literature[28]. The low frequency electrode features show some changes during coloration but their mechanistic discussion is beyond the scope of this paper. Figure 5 d) to g) indicates, how the individual OCVs

develop with time. This OCV reflects the Li chemical potential difference between the investigated electrodes. Before any DC voltage was applied, the voltages between the different circular electrodes and the reference electrode were in the 10 to 20 mV range, which indicates that the sample was chemically equilibrated. After 4 minutes the working electrode has reached 2.4 V, while all other electrodes are still close to zero. All neighboring electrodes were above 2 V after 20 minutes and after 95 minutes those electrodes are essentially equipotential at 2.4 V. It is noteworthy that a voltage of roughly 2.5 V also marks the onset of a weak cathodic coloration.

2.6 Discussion of coloration, voltage distribution and rate limiting region

A strong darkening of LLTO was reported in literature after reductive sintering[56] or electrochemical lithiation through an organic electrolyte with an external Li source[28]. The latter represents an over-lithiation and we are confident that also in our case such an over-lithiation takes place in the colored zone. This means that during electrocoloration, Li^+ is introduced into vacant A-sites, while the charge is balanced by the reduction of Ti^{4+} to Ti^{3+}. Accordingly, instead of decomposition and formation of new phases, over-lithiation is assumed to be the predominant electrochemical reaction at the cathode, also under high voltages. As a result, significant electron conduction can be expected in this zone, particularly due to the reported high electron mobility in LLTO[56]. Still the impedance measurements showed that electronic conductivity does not exceed the ionic one under most conditions.

Mixed conductivity in the colorized region also explains the observation that in type II experiments electrodes within the colored region have almost zero voltage relative to the cathode. Their rather large OCV voltage of 2.4 V with respect to the reference electrode in the uncolored region indicates a sharp drop of the electronic conductivity in the uncolored region. The latter thus remains intact as an electrolyte. From the almost unchanged ionic conductivity, even in the colored zone, we can also conclude that Li vacancy concentrations are hardly changed and thus the chemical potential of Li ions μ_{Li+} is almost constant.

Therefore changes of the lithium chemical potential, given by the relation $\Delta\mu_{Li} = \Delta\mu_{Li^+} + \Delta\mu_{e^-}$, are directly linked to the electron chemical potential μ_{e^-}, or Fermi level ($\Delta\mu_{Li} \approx \Delta\mu_{e^-}$). Consequently, the onset of coloration of LLTO corresponds to the Fermi level caused by the partial reduction of Ti^{4+} to Ti^{3+}.

When a voltage of 5 V is applied to LLTO, the OCV between anode and cathode remains at about 2.4 V after switching off the external voltage source. The rest of the applied voltage - roughly 2.6 V must therefore be a kinetic overpotential that is associated to ion conduction in LLTO and/or electrochemical reactions near the cathode and the anode. This raises the questions regarding the origin and location of such a large kinetic overpotential in polarized LLZO. In experiment type I, upon 5 V the current density in the in-plane part of the sample is less than about $5 \cdot 10^{-4}$ A/cm^2 after 10 seconds and decreases to less than $3 \cdot 10^{-5}$ A/cm^2 beyond 200 s. With a total conductivity in the range of $5 \cdot 10^{-4}$ S/cm, we can thus estimate the ohmic overpotential across the bulk part of the sample as about 1 V (10 s) and <60 mV (>200 s) – meaning that soon only a small fraction of the kinetic overpotential is due to Li-ion conduction.

Hence, the majority of the overpotential (2.6 V) has to be consumed by an electrode process rather than by bulk charge transport. Moreover, the kinetics of this electrode process becomes significantly worse with time, and the decay rate of the current resembles a diffusion limited process (although not perfectly). The growth rate of the colorized zone, shown in Figure 3, also resembles a diffusion limited process. However, Ti^{3+} ions in the colored zone can only increase but not decrease the conductivity in this region. We thus conclude that the major part of the kinetic overpotential has to be associated with the Li depletion reaction at the anode, rather than with the overlithiation at the cathode.

Some further conclusions can be drawn from these experiments: i) With blocking electrodes, only the width of the stability window is accessible, while knowledge of absolute values of Li chemical potentials or activities need further experiments. According to a study by Birke et al.[28] the reduction onset of LLTO is in the range of 1.7-1.8 V vs. Li metal. We may assume the same chemical potential in our colored zone. In our measurements, we determine the width of the stability window as 2.4-2.5 V (onset of electrocoloration front movement), and thus the oxidative stability limit is in the range of about 4.1-4.3 V vs. Li

metal. This is significantly higher than 3.7 V[1] obtained from first-principles DFT calculations.

ii) The concentration of excess lithium in the colored zone can be calculated from the amount of the Li-excess and the estimated volume of the colored zone, assuming that the entire charge flows as Li-ions (see Table 2). We obtain a mere 10^{-6} mol/cm^3, or less than 10^{-4} excess Li$^+$ and Ti^{3+} ions per formula unit. Consequently, the concentrations of Li-occupied and vacant A-sites remains virtually unchanged, which leaves the Li-ion chemical potential constant, cf. assumption above. Please note that in the presence of electronic trap states in the band gap, those are also filled and even less Ti^{3+} ions are formed. Interestingly, for 5 V and 20 V the over-lithiation concentration is almost the same, see slope of the coloration volume vs. charge curve in Figure 6. This may indicate the presence of electron traps in our LLTO.
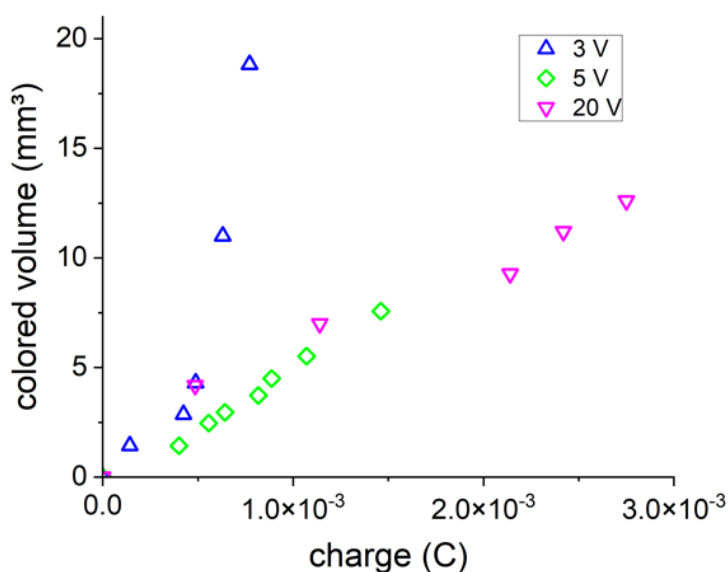
Figure 6: Accumulated charges (calculated by integration of currents over time) and corresponding volumes of the colored zones from electrocoloration experiments at 3 V (blue triangles), 5 V (green diamonds) and 20 V (pink triangles).

iii) It was discussed above that absence of gaseous oxygen is required to see electrocoloration and that oxygen, CO_2 and water vapor annihilate existing colored zones. The standard equilibrium voltage for the formation of Li_2O_2 is 2.9 V vs. Li metal. The Li chemical potential in the colorized LLTO corresponds to 1.7-1.8 V vs Li metal, which is much below the typical discharge potential of Li-air batteries[57]. The discoloration reaction

$$2\,Li^+ + 2\,Ti^{3+} + O_2 \rightarrow 2Ti^{4+} + Li_2O_2 \tag{2.1}$$

has thus an energy gain > 2x1 eV. Owing to fast chemical diffusion of Li, this LLTO oxidation reaction may thus take place at the surface at a rate that is sufficient for fast discoloration. Additional humidity and CO_2 may further lead to LiOH and Li_2CO_3 formation at the surface of LLTO.

2.7 Quantification of the chemical composition by laser ablation mass spectroscopy

As discussed above, the kinetic overpotentials for Li-ion and/or electron conduction in the reduced and uncolored zones are rather small, and therefore the largest part of the kinetic overpotential is located in the oxidized zone, at least after some time. Since the oxidized zone is optically not observable, we assume that it is spatially strongly confined to a volume directly underneath the anodic terminal. In order to validate this hypothesis, laser ablation inductively coupled plasma mass spectroscopy (LA-ICP-MS) was employed to determine the chemical composition in localized zones of the LLTO samples: a focused laser with a beam size of 20 μm was used to remove material, and by appropriate laser parameters (see Experimental) a depth resolution of about 100 nanometers could be achieved.

In the corresponding experiments of type III we first polarized a sample for some time and then performed the depth resolved quantitative elemental analysis. In the course of these experiments it became obvious that at the surface of LLTO a Li enriched phase is present, supposedly Li_2CO_3 or $Li(OH)_2$, formed due to interaction with the ambient atmosphere. Even in synthetic gases and at lower gas pressures we could not avoid a rather quick

(re)formation of this layer after its mechanical (grinding) or chemical (leaching in pure H_2O) removal. This hampers the quantitative analysis of the Li content in LLTO before and after polarization. In order to enhance the amount of Li depletion in the anodic range, we therefore increased temperature during polarization to 100-150 °C. Figure 7a shows that also under these conditions a strong coloration front originates at the cathode.

In Figure 7b Li depth profiles in the depleted zone beneath the anode are shown after 80 minutes polarization at 150 °C using voltages between 4 and 8 V. Already for 4 V a very strong Li depletion by more than 50 % is found in the first few 100 nm; the Li content increases with depth and reaches the bulk value in about 4 µm depth. For 6 V the situation is even more pronounced, with almost complete Li depletion up to a depth of ca. 2.5 µm, followed by an increase to the bulk value at ca. 6 µm. For 8 V an almost complete Li depletion is detected in the entire depth measured, i.e. to 9 µm. These measurements showed that indeed the zone beneath the anode exhibits very strong Li depletion and is confined to a rather thin layer. For room temperature measurements and thus much lower currents than those used in this type IV experiments, we may expect Li depletion layers in the µm or sub-µm range.
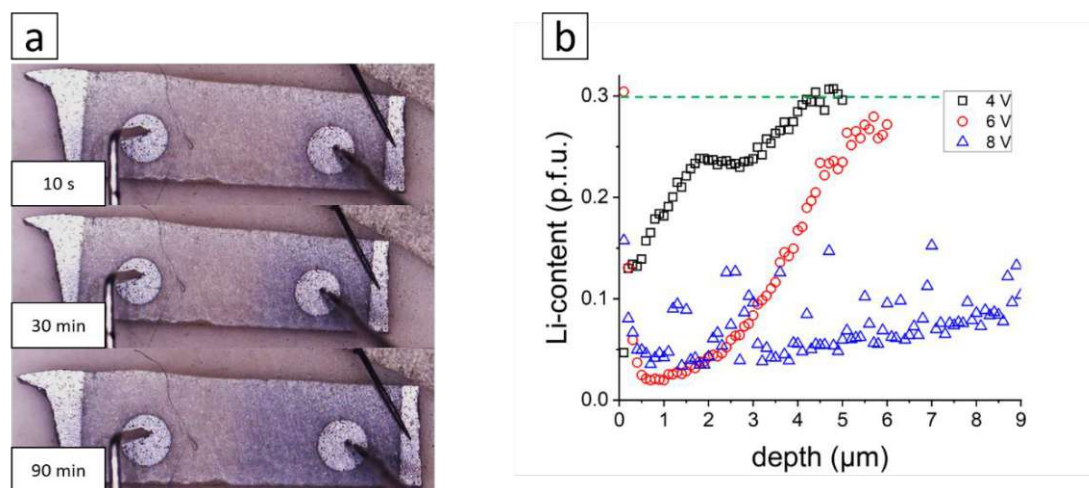
Figure 7: (a) Photographs of a sample, which was polarized at 100 °C with 5 V for 90 minutes. (b) shows the Li-concentration depth-profiles of anodes, polarized with 4 V (black squares), 6 V (red circles) and 8 V (blue triangles) at 150 °C for 80 minutes, respectively.

We can also calculate the cumulative charge of the depleted Li-ions by

$$Q_{dep} = \frac{FA_{el}}{V_m} \int 0.29 - c(Li^+)\, dz. \tag{2.2}$$

Therein, V_M is the molar volume of LLTO (37.5 cm^3/mol), and A_{el} is the area of the anodic electrode. The calculated charges are $4 \cdot 10^{-4}$ C for 4V, $1.4 \cdot 10^{-3}$ C for 6V and $> 3 \cdot 10^{-3}$ C for 8V. These values are roughly twice the electrically measured charge, indicating that the current is partly also electronic under these conditions.

In order to better understand the mechanism of Li depletion at the anode, in-situ synchrotron XRD measurements of the oxidized LLTO zone were performed (experiment type IV). Therein, a sample of LLTO (cut from the 0.5 mm thick sheet) was subjected to oxidative field stress (up to 7 V) with a small working electrode (Au, 0.6 mm^2) and a larger counter electrode (Au, 10 mm^2) in a cross-plane geometry at 25 °C for several hours, see Figure 2. Even with a bright synchrotron X-ray source, no new phases were found during field stress, even though formation of amorphous phases cannot be excluded. However, the splitting of LLTO reflexes increases considerably, as shown in Figure 8. This indicates a stronger distortion of the perovskite structure, which is a common phenomenon when point defect concentrations change. Due to the small X-ray spot size, only few crystallites randomly produce reflexes, so a structural refinement is not possible. As the exact supercell size is not known, reflexes were indexed according to a unit cell containing a single ABO$_3$ formula unit.
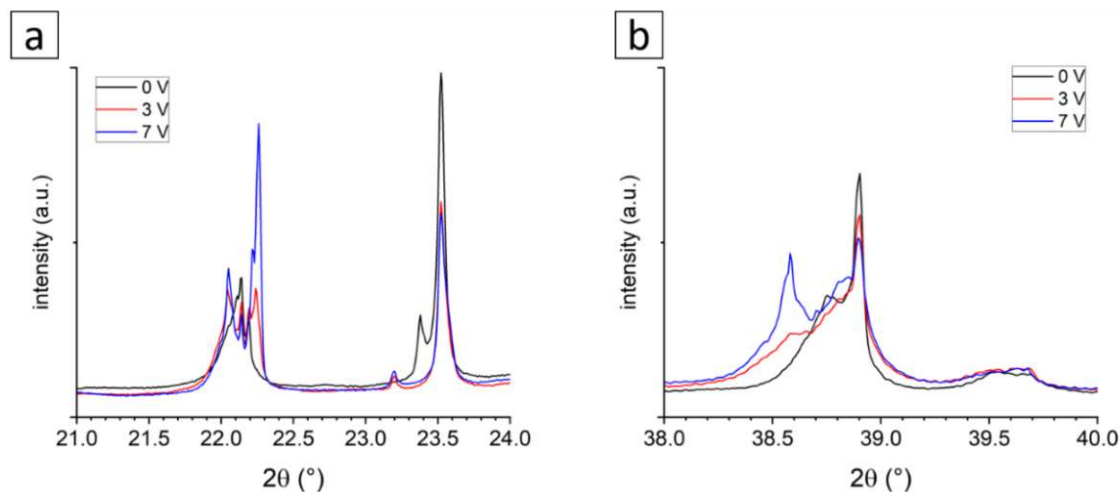
Figure 8: Exemplary diffractograms from in-situ synchrotron XRD measurements. The effect of oxidative field-stress up to 7 V is indicated by slight shifts of LLTO-reflexes only. There is no evidence of newly formed crystalline phases throughout the measurement range. The intensities of all diffractograms were normalized to the integral of the Au(111)-reflex at about 26° (originating from the electrode), not shown here. (a) shows the (122)/(-122) and (021)/(201)-reflexes at 22.3° respectively 23.5 °, whereas (b) shows the (123)/(321)-reflexes at 39°. All reflexes split further apart due to polarization, indicating an increasing lattice distortion from the ideally cubic perovskite structure.

2.8 Discussion of the anodic reaction

We now know that during coloration the largest part of the kinetic overpotential is confined to a rather narrow, heavily Li-depleted zone. The LA-ICP-MS results after polarization at 150 °C revealed depletion zones in the μm-range. We may estimate the thickness of this zone also for our room temperature measurements by assuming that the entire electrical charge corresponds to depleted Li-ions under the anode, and that on average 0.15 Li atoms are missing per unit cell. After polarization with 5 V for 5 minutes at room temperature, the charge of $6 \cdot 10^{-4}$ C (see Table 2) corresponds to a Li depletion thickness of 0.8 μm. In this case, the kinetic overpotential is in the range of 2.5 V and the total current is $5 \cdot 10^{-7}$ A. A homogeneous electric field in the Li depleted zone is thus as large as 30 kV/cm, provided the rate limiting conduction process takes place in this zone. This corresponds to a rather

low conductivity of about $4 \cdot 10^{-10}$ S/cm. Interestingly, this value is within the (admittedly rather large) error when extrapolating the oxide ion conductivity of slightly oxygen deficient $SrTiO_3$ from Ref.[58] to room temperature. Based on the observed strongly confined Li depletion and the calculated low conductivity in the depleted zone, we may now discuss the type and mechanism of the oxidation reaction at the anode. The Li-ion depletion requires the appearance of a relative positive counter charge. We consider three mechanisms or anodic reactions that may establish the required charge balancing, see sketch in Figure 9.
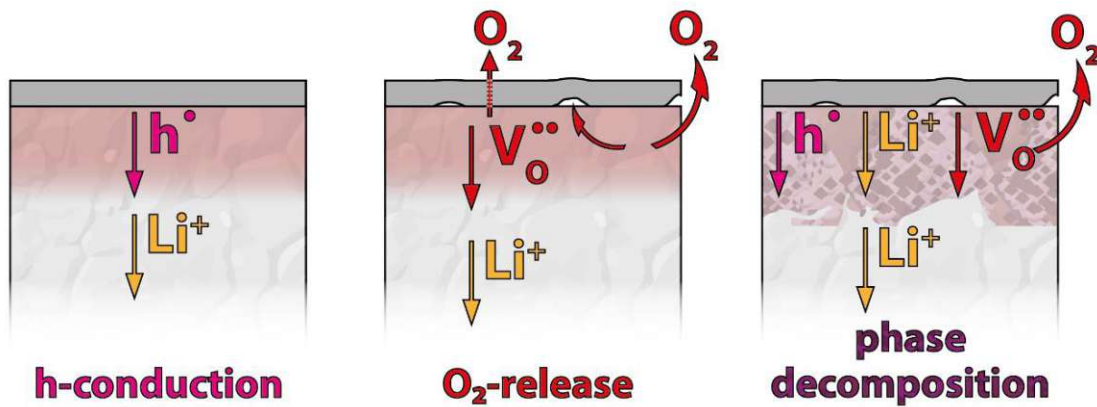
Figure 9: Schematics of the three suggested anode mechanisms: oxidation at the anode leads to either hole-conduction in LLTO (left), oxygen conduction via oxygen vacancies, written in Kroeger-Vink notation, (middle) or decomposition into secondary phases (right) with Li, oxygen and possibly hole conduction. The latter two include evolution of O_2, which leaves the solid either via the triple phase boundary, via grain boundaries[59] or by formation of oxygen bubbles underneath the metal electrode.

The first possible mechanism is simply Li stoichiometry polarization with electron holes as charge balancing point defect – corresponding to an electron chemical potential that approaches the valence band maximum. This is the common delithiation process of many oxide electrodes of lithium ion batteries. However, a significant electron hole concentration should also induce significant electron hole conduction in the oxidation zone. This would in turn lead to a more extended oxidized zone, which builds up with low kinetic overpotential – similar to the near-cathode reduction of our LLTO. This obviously contradicts our

observations. Hence, we think that this mechanism may be present for lower voltages (at least to a certain extent), but does not dominate the electrocoloration phase at higher voltages. Please note: This (reversible) Li depletion with charge balancing by electron holes is not a true decomposition and does not limit the electrochemical stability in terms of decomposition, though it may certainly limit the applicability of the electrolyte due to electron conduction.

However, also for only moderate changes of the Fermi level, the Li chemical potential is closely linked to the oxygen chemical potential, due to the relations

$$\mu_{Li} = \mu_{Li^+} + \mu_{e^-} \tag{2.3}$$

and

$$\mu_{O_2} = 2\mu_{O^{2-}} - 4\mu_{e^-} \tag{2.4}$$

Let us now consider the initial phase of delithiation (for small or moderate voltages), caused by a decrease of the Li chemical potential. Since μ_{Li^+} is still rather constant, see above, μ_{e^-} decreases accordingly. Owing to Nernst's equation, a decrease of μ_{e^-} by only 59 meV corresponds to an increase of the equivalent $p(O_2)$ by 4 orders of magnitude, cf. Equation (2.4). From the absence of significant electronic conductivity in LLTO equilibrated in air we know that the electron chemical potential at which μ_{O2} corresponds to 1 bar (according to Equation (2.4)) is considerably above the valence band maximum. When an applied voltage decreases the electron chemical potential beyond this point, the oxygen chemical potential becomes very high and we get a strong driving force for formation of oxygen gas at the LLTO surface. This oxygen evolution hinders the building up of a substantial electron hole concentration. We can therefore summarize the anodic reaction as

$$2\,O^{2-} + 4Li^+ \rightarrow 2V_O + 4V_{Li} + O_2 + 4Li_{LLTO,cath} \tag{2.5}$$
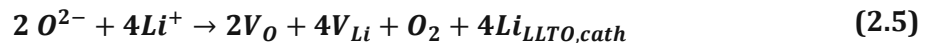
with $Li_{LLTO,cath}$ indicating that the extracted Li ends up in the overlithiated region of LLTO near to the cathode (symbol V indicates vacancies of the respective ions, relative charges are not given due some ambiguity in defining it for Li on A-sites). Such a nominal Li_2O depletion in the perovskite, is similar to the mechanism proposed for Garnet type Li conductors[23], in which high oxygen anion mobility was observed, which indicates a

considerable amount of oxygen vacancies[60]. Also, the stronger lattice distortion found in LLTO during anodic bias supports this hypothesis of defect formation. Further, the calculated conductivity of the Li depleted zone is in line with the assumption of rate limiting oxygen ion conduction. Moreover, the growth of such an oxidized zone would be diffusion limited, in accordance with the decaying DC current. This oxygen loss is most probably largely irreversible at low temperatures and the corresponding material would thus be beyond its electrochemical stability limit.

The third possible mechanism involves secondary phase formation as indicated by DFT calculations, which suggest appearance of TiO_2, $La_2Ti_2O_7$, and O_2[26] at a voltage > ca. 3.8 V vs. Li metal. Indeed, $La_2Ti_2O_7$-impurities may form in LLTO, likely due to Li-loss during synthesis[61]. Progression of this process would require O^{2-} and/or Li^+ and/or hole transport in the respective phases. At room temperature, the kinetics of the required phase transitions is probably too sluggish to happen even though we cannot exclude it: Almost complete depletion of Li_2O in LLTO may cause structural instability and amorphization of the Li depleted zone. This would be hardly detectable by XRD.

2.9 Model of electrocoloration and electrochemical stability of LLTO

Altogether, we suggest the degradation model sketched in Figure 10a. In the colorized zone next to the cathode, slight Li-excess stoichiometry is balanced by a small concentration of Ti^{3+}, which causes mixed ion and electron conductivity at a Li chemical potential around 1.7-1.8 V vs. Li metal. Above ca. 4.2 V vs. Li metal, the Li^+ depletion is balanced by oxygen release at the anode, which requires oxygen vacancy formation and conduction. Owing to the low ambipolar conductivity of Li^+ and O^{2-} ions, this process is rate limiting during electrocoloration and limits the kinetics of the electrolyte decomposition. Actually, nominal Li_2O diffusion in LLTO determines the entire kinetics of our polarization experiments and thus indirectly also the velocity of the cathode color front movement.

Hence, we can also suggest a qualitative picture of the overpotential and Li activity distribution. Due to the high ionic conductivity and low current density within the uncolored and reduced zones, the electrical potential is almost constant there, as illustrated in Figure 10b. Moreover, the total Li content varies only marginally within the reduced region and also the Li-ion chemical potential is virtually homogeneous. Nonetheless, the electron and lithium chemical potentials vary due to the different Ti^{3+} concentrations of colorized and uncolored zones. In the oxidized zone, on the other hand, most of the kinetic overpotential drops which corresponds to a steep electrical potential gradient in a weakly conductive, heavily Li depleted zone with charge balancing oxygen vacancies. Please note that due to our definition of anode (= oxidation reaction) our anodic reaction takes place at a very high voltage vs. Li metal, while the cathode is much closer to Li metal. When using LLTO as an electrolyte in batteries, our anodic, i.e. oxidized side is in contact with typical battery cathode materials. High voltage cathode materials are this most probably problematic when using LLTO as an electrolyte. Altogether, an electrochemical stability window of about 2.4-2.5 V results for two ion-blocking electrodes. However, only the oxidation is an irreversible decomposition reaction and limits the overall phase stability. The overlithiation process is still reversible and also voltages < 1.7 V vs. Li metal are possible without decomposition as long as the other electrode does not reach ca. 4.2 V.
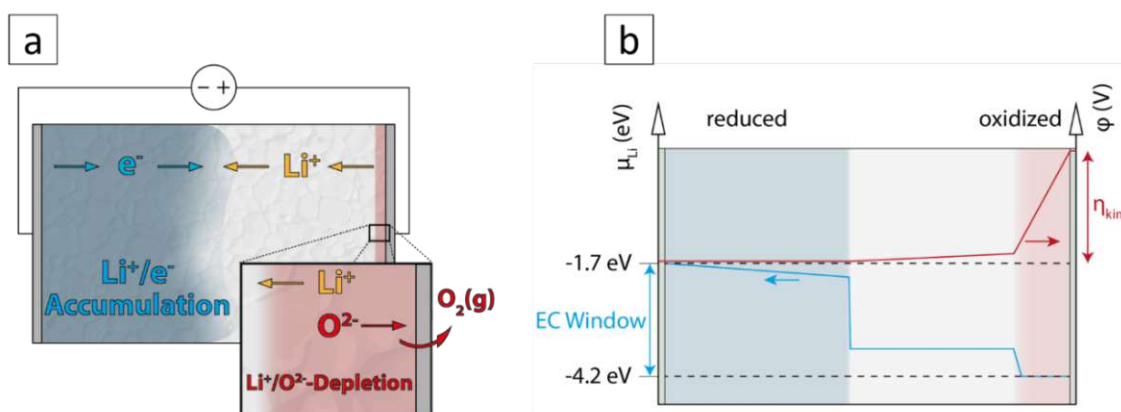
Figure 10: a: Schematic of the proposed electrocoloration mechanism at the limit of about 2.5 V. b: Schematic representation of Li chemical potential μ_{Li} (blue line, left y-axis), electrical potential φ (red line, right y-axis) and electrochemical (EC) stability window. Not drawn to scale.

2.10 Conclusions

The electrochemical stability window and the decomposition mechanisms of LLTO were investigated by electrochemical and analytical experiments. Above a voltage of about 2.4-2.5 V between two ion blocking electrodes a coloration front starts moving from the reduction side (cathode) towards the anode. This coloration is caused by a slight overlithiation (< 10^{-4} p.f.u.), associated with Ti^{3+} formation taking place at a potential of about 1.7-1.8 V vs. lithium metal. The corresponding moderate electronic conductivity in the colored zone may limit applicability of LLTO as an electrolyte, but is not caused by an irreversible decomposition reaction. The anodic oxidation reaction, on the other hand, is associated with a strong Li depletion in a very confined zone in the micrometer range, as shown by LA-ICP-MS measurements. OCV measurements after coloration indicate a voltage difference of about 2.4 V between oxidized and reduced sides of LLTO. The oxidative process is triggered by a voltage of about 4.2 V vs. Li metal and is most probably a true decomposition reaction. We suggest that oxygen evolution and oxygen vacancy formation rather than electron hole formation takes place at this electrode. This causes a strong Li_2O depletion in the LLTO perovskite phase near to the anode. The kinetics of this oxidation reaction is (at least partly) determined by the kinetics of combined oxide ion and Li-ion conduction and is thus rather sluggish. The slow anodic reaction also limits the velocity of the electrocoloration process. In terms of electrochemical stability, we can therefore conclude a stability window of about 2.4-2.5 V when using two ion blocking electrode but the most critical process is the anodic decomposition at high voltages vs. Li, which may hamper application of LLTO with high voltage cathode materials.

3 Point defect chemistry, electrolytic domain and mobility of electronic defects in lithium lanthanum titanate electrolytes during the early stage of reduction

This chapter largely corresponds to a manuscript to be submitted to a peer-reviewed journal (authors: J. Ring, A. Nenning and J. Fleig).

3.1 Abstract

Lithium lanthanum titanate (LLTO) is a Li ion conducting material with high ionic conductivity and potential application in Li-ion batteries. Upon reduction, excess Li can be inserted into vacant sites and LLTO becomes a mixed ion and electron conductor. This transition was investigated by electrochemical methods. The electronic conductivity of $Li_{0.29+\delta}La_{0.57}TiO_3$ was measured in dependence of the Li excess δ. An overlithiation offset of about $\delta = 4 \cdot 10^{-4}$ is required until significant electron conduction sets in and this is attributed to electron traps in the band gap, which first have to be filled before Ti^{3+} is formed. Above this offset, the conductivity increases linearly up to about $\delta = 3 \cdot 10^{-3}$. The corresponding electron mobility of LLTO results as 0.1 cm^2/Vs. The conductivity values are discussed in terms of the electrolytic window, which ends at about 2.05 V vs. Li metal. The dependence of the LLTO equilibrium voltage on the Li excess is described by a defect chemical model, which includes a concentration dependence of the standard chemical potential of individual Li ions. The Li chemical diffusion coefficient was investigated by a galvanostatic intermittent titration technique (GITT) as a function of the lithium chemical potential and compared with predictions based on the extracted thermodynamic data.

3.2 Introduction

$Li_{0.29+\delta}La_{0.57}TiO_3$ (LLTO) with $\delta = 0$ is a solid state Li ion conductor with an A-site deficient perovskite structure. Owing to its high Li ion bulk conductivity, it is an interesting electrolyte material for all solid state batteries[36,48,62–64]. However, it becomes electrochemically reduced at voltages lower than ca. 1.7 V vs. Li^0, which introduces mixed ionic and electronic conductivity (MIEC)[28]. Upon electrochemical reduction, Li ions are inserted into the vacant A-sites (0.14 per formula unit for $\delta = 0$) and electrons are injected, giving rise to electron conduction and dark coloration of the formerly colorless material. Partial coloration of LLTO can also be achieved without any external Li-source by mere stoichiometry polarization, as reported in a separate study. These changes in the conduction behavior (and color) of LLTO are problematic for its use as electrolyte, but may allow other applications, particularly as an anode material in Li based batteries, in electrochromic devices and for resistive switching applications.

In literature, the potential usage of LLTO as an anode in Li ion batteries was already tested, and while first results gave rather modest capacities and cycling performance[28,65,66], recent studies with slight optimizations revealed a reversible capacitance up to 260 mAh/g[67,68] and stable cycling over 10000 cycles[69] in a potential window of 0-1.7 V vs Li metal. This makes LLTO a useful anode candidate for applications where cycling performance is more important than very high energy densities. It was also shown that interstitial Li is incorporated into $Li_{0.5}La_{0.5}TiO_3$ below potentials of about 1 V vs. Li metal and that LLTO may have a better electrode performance than $Li_4Ti_5O_{12}$[29,37,68].

In this paper, we consider the transition from a Li-conducting electrolyte to a mixed conductor and thus to an anode material. First, we introduce a simple defect chemical model to describe this transition and the electrolytic domain boundary. Then we employ galvanostatic titration and impedance spectroscopy to determine the electronic conductivity, the ionic transference number and the Li chemical diffusion coefficient as a function of δ in $Li_{0.29+\delta}La_{0.57}TiO_3$. Owing to the absence of structural transformations during the Li insertion up to $\delta=0.14$, LLTO proves to be an excellent model material for such investigations. The studies also reveal the potential of LLTO as a high rate capable anode material.

3.3 Point defect chemistry of LLTO

As a basis for investigating the transition between ionic and mixed conducting LLTO and to interpret the subsequent measurements, we first discuss a simple defect chemical model describing Li insertion into LLTO. In perovskite-type LLTO the B-site is occupied by Ti^{4+} while the A-site hosts La^{3+}, Li^+ ions and a substantial amount of A-site vacancies. The nominal crystallographic charge at the A-site is 2+, so all A-site occupants in LLTO have nonzero defect charge. In Kroeger-Vink notation we have $La_A^{\cdot}$ and A-site vacancies (V_A''). Without electronic defects, the charge neutrality and A-site conservation is satisfied by the compositions according to $La_{0.666-x/3}Li_xTiO_3$, where x can vary from 0 to 0.48[24], and compositions with x≈0.29 (i.e. $Li_{0.29}La_{0.57}TiO_3$) have the highest Li ion conductivities[36,44], due to the large amount of A-site vacancies (0.14 per formula unit). LLTO with such a La content is now further considered.

In contrast to liquid electrolytes, also conduction band electron and valence band hole defects are present in LLTO. Due to its comparatively large bandgap of about 2.1 eV[68], the intrinsic charge carrier concentration and electronic conductivity of LLTO is quite low. However, conduction band electrons can be introduced by reduction. Those can be attributed to Ti ions (Ti^{3+}) and thus we denote them as Ti_{Ti}'. Such electrons have relatively high mobility[56] and can thus lead to an early breakdown of the electrolytic domain. For example, this can be observed after sintering of LLTO ceramics in reducing conditions[56], leading to oxygen loss at high temperature, according to the reaction

$$O_O^{\times} + 2Ti_{Ti}^{\times} \rightleftharpoons 2Ti_{Ti}' + V_O^{\cdot\cdot} + \frac{1}{2}O_2. \tag{3.1}$$
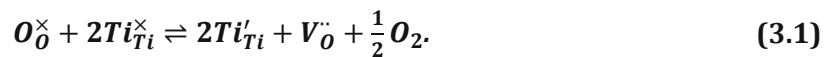
Electrochemical over-lithiation of LLTO through the filling of Li vacancies with Li ions and the corresponding reduction of Ti^{4+} to Ti^{3+} also leads to significant electron conduction. This process is analogous to the lithiation of an intercalation electrode material from an arbitrary Li source with Li chemical potential μ_{Li} and the corresponding equation can be written as

$$V_A'' + Ti_{Ti}^{\times} + Li \rightleftharpoons Li_A' + Ti_{Ti}' \tag{3.2}$$

When employing an electrochemical cell, the chemical potential of Li in LLTO is determined by the voltage of the LLTO electrode (U_{LLTO}) vs. a Li^0 electrode with chemical potential $\mu_{Li}^{\emptyset}$ according to

$$\boldsymbol{\mu_{Li} = \mu_{Li}^{\emptyset} + FU_{LLTO}}. \tag{3.3}$$

We can now describe the equilibrium of the electrochemical reduction reaction (3.2) as a function of the Li-excess $\delta = [Li_A'] - 0.29$ and $[Ti_{Ti}']$ with symbols [.] indicating fractions with respect to the formula unit. On the A-site, 57% of the sites are occupied by immobile La ions, leaving $[Li_A'] + [V_A''] = 0.43$ and thus $[V_A''] = 0.14$ for $\delta = 0$. Therefore, we obtain as the mass action law of reaction (3.2) with constant K_{red} according to

$$\boldsymbol{K_{red} = \frac{[Li_A'][Ti_{Ti}']}{[V_A''][Ti_{Ti}^{\times}]} = \frac{(0.29 + \delta)[Ti_{Ti}']}{(0.14 - \delta)(1 - [Ti_{Ti}'])} = \exp\left(-\frac{\Delta_R G_{red}^{\emptyset} + FU_{LLTO}}{RT}\right)}. \tag{3.4}$$

Symbol $\Delta_R G_{red}^{\emptyset}$ denotes the standard Gibbs free energy of reaction (3.2) with respect to metallic Li as Li source.

In the absence of any other ionic and electronic defects, e.g. no electronic traps in the band gap, electroneutrality requires that all excess Li-ions (beyond 0.29) are compensated by Ti_{Ti}', i.e. $[Ti_{Ti}'] = [Li_A'] - 0.29 = \delta$. This simplifies Equation (3.4) and the equilibrium voltage of a reduced LLTO sample vs. Li metal (U_{LLTO}) can be related to δ via

$$\boldsymbol{U_{LLTO} = -\frac{\Delta_R G_{red}^{\emptyset}}{F} - \frac{RT}{F} \ln\left(\frac{(0.29 + \delta)\delta}{(0.14 - \delta)(1 - \delta)}\right)}. \tag{3.5}$$

In our measurements we found that also trapped electrons are relevant and thus we have to stay with the more general Equation

$$\boldsymbol{U_{LLTO} = -\frac{\Delta_R G_{red}^{\emptyset}}{F} - \frac{RT}{F} \ln\left(\frac{(0.29 + \delta)[Ti_{Ti}']}{(0.14 - \delta)(1 - [Ti_{Ti}'])}\right)}. \tag{3.6}$$

Experimental studies[28] have shown that the characteristic redox peak for the reduction of LLTO is roughly at 1.5 V vs. Li metal, and that LLTO can be cycled like an electrode material in a potential window of 1.2-1.7 V vs. Li metal without the appearance of new phases. The electrolytic domain boundary can be defined as the Li chemical potential region in which the ionic transference number $t_{ion} > 0.99$[70]- which corresponds to an upper boundary of the electron conductivity σ_e of about $5 \cdot 10^{-6}$ S/cm for a room temperature ion conductivity σ_i of

$5 \cdot 10^{-4}$ S/cm (see Results). Owing to the supposedly high mobility of electrons[56], the boundary of the electrolytic domain is already reached for very weakly overlithiated LLTO (i.e. above 1.5 V and thus above the reduction potential of $Li_4Ti_5O_{12}$). In this range of very small δ, we can approximate that $[Li_A'] \approx 0.29$ and $[V_A''] \approx 0.14$, and titanium being mostly Ti^{4+}. Close to the electrolytic domain boundary, we can thus simplify the reduction equilibrium (Equation (3.4)) to

$$K_{red} \approx \frac{0.29}{0.14}[Ti_{Ti}'] \,. \tag{3.7}$$

The electronic conductivity of LLTO can be expressed by

$$\sigma_e = \frac{F \cdot u_e}{V_m} \cdot [Ti_{Ti}'] \,, \tag{3.8}$$

where u_e is the electron mobility and V_m the molar volume of LLTO. At the electrolytic domain boundary (db), we have $\sigma_e \approx 0.01 \, \sigma_i$ and the critical $[Ti_{Ti}']_{db}$ is thus

$$[Ti_{Ti}']_{db} = \frac{0.01\sigma_i \cdot V_M(LLTO)}{u_e F} \,. \tag{3.9}$$

The corresponding voltage vs. Li metal can be approximated by

$$U_{db} = -\frac{\Delta G_{red}^\emptyset}{F} + \frac{RT}{F}\ln\left(\frac{0.29 \, [Ti_{Ti}']_{db}}{0.14}\right). \tag{3.10}$$

Accordingly, the limiting voltage of the electrolytic domain depends on the free enthalpy of reduction and the electron mobility. Consequently, reducibility and electron mobility both decide on the applicability of LLTO as an electrolyte or as a mixed conductor with possibly high ion and electron conductivity[28]. In the "Results and Discussion" part, this defect model is refined by including defect interaction and electronic traps. Those are required to explain the experimental results.

3.4 Experimental

Polycrystalline LLTO-sheets (0.5 mm thick) with nominal stoichiometry $Li_{0.29}La_{0.57}TiO_3$ were used throughout this work (Toho Titanium Co., Ltd., Japan). Rectangular samples, with

typical dimensions 5x12 mm^2, were prepared by cleaving. Two Pt stripe electrodes (200 nm thick, 2 mm wide) were deposited onto the sample surface by magnetron sputtering (Baltec Med 020) at room temperature. Inside a glovebox, the sample was transferred into a customized measuring cell. Inside the cell, the electrodes on the sample were contacted by platinum needles and the entire sample was submerged into a commercial, organic based (LiPF$_6$ in EC/DMC 50:50, battery grade) Li-electrolyte (Sigma-Aldrich). A stripe of Li-metal (Goodfellow, battery grade) was submerged into the electrolyte as a counter electrode and Li-source.

For the electrochemical characterization, two different electrode configurations were employed, as illustrated in Figure 11. First, the sample was reduced in small stoichiometry steps up to a total δ-value of 0.012, which corresponds to a filling of about 9% of the originally 0.14 vacant A-sites. The electrical conductivity of LLTO was measured after each δ-change by electrochemical impedance spectroscopy (EIS). Then the sample was re-oxidized in the same manner back to its original, fully oxidized state. The measurements were carried out in cycles as follows:

- Galvanostatic reduction/oxidation in configuration A with a rate of C/100 for 514 seconds (1/7 hour), changing the stoichiometry in a single step by a δ-value of 2·10^{-4} (0.14/700). The two stripe electrodes on LLTO are short-circuited and act as one working electrode.
- Relaxation period, waiting for a stable OCV ($\frac{|dU|}{dt}$ < 0.1 mV per minute) (configuration A)
- EIS (configuration B)

This switching of the electrode configurations allows for a very precise manipulation of the stoichiometry and subsequent characterization of the LLTO sample. The electrochemical measurements were carried out by means of a SP-200 potentiostat with integrated impedance analyzer (Biologic). The Li excess δ in LLTO was determined from the integral charge in configuration A, according to

$$\delta = -\frac{Q \cdot m_{LLTO}}{F \cdot M_{LLTO}}, \qquad (3.11)$$

where m_{LLTO} is the mass of the sheet and M_{LLTO} is the molar mass of LLTO.
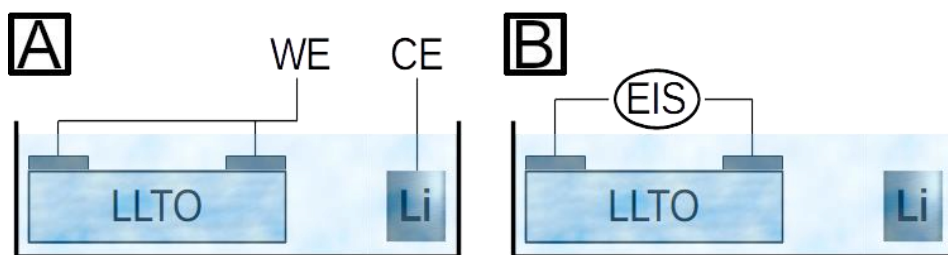
Figure 11: Schematic representation of the electrode configurations used for galvanostatic reduction/oxidation (A) and EIS (B).

Please note that depending on the total conductivity of LLTO, either charge transport in LLTO or in the organic electrolyte determine the EIS measurements in configuration B. As long as the ionic conductivity prevails conduction in LLTO, configuration B is dominated by the better conductive organic electrolyte. However, already for small δ values, LLTO has a high electronic conductivity (see Results) and configuration B is applicable for the δ-dependent LLTO characterization by EIS.

3.5 Results and discussion

3.5.1 Galvanostatic titration and electronic conductivity

In order to precisely determine the reduction potential and the electronic conductivity of LLTO as a function of the lithium chemical potential, galvanostatic titration curves (U vs. δ) of a dense LLTO sheet were determined as described in the Experimental section (configuration A). After each rest step, an impedance spectrum was measured between two Pt electrodes on the LLTO sheet (configuration B). First, we examine the titration curves of reduction and oxidation. Before the first lithiation, the equilibrium voltage of the LLTO sheet is ca. 3 V. Already the first lithiation step ($\delta = 2\cdot10^{-4}$) drastically decreases this value down to ca. 1.9 V vs. Li metal.

Through a window in the titration cell, the optical changes of the LLTO sheet during reduction could be monitored (s. Figure 12). It is clearly visible that a dark coloration front propagates from the two electrodes towards the center of the LLTO sheet during the first lithiation steps. Upon further reduction, the darkening gets more pronounced and also electronic conduction becomes measurable by impedance spectroscopy (see below). In accordance with other studies[28,31,56] we conclude that the darkening reflects the formation of Ti'_{Ti} due to Li insertion and thus of electrons in the conduction band.

The curve acquired in the range δ < 0.012 is largely free from hysteresis (s. Figure 13). Only below

δ = $2 \cdot 10^{-3}$, the values of reduction and oxidation differ significantly. The sample is thus considered to be well equilibrated after each reduction/oxidation step, at least above δ = $2 \cdot 10^{-3}$. The hysteresis towards δ = 0 is most probably caused by lithiation inhomogeneities due to the low electronic conductivity in this range (cf. also color fronts in Figure 12B). Those can be different during oxidation and reduction[71]. The steep voltage increase towards δ = 0 is in good agreement with the defect chemical model and it is reasonable to assume that the faradaic efficiency of the charge/discharge is close to unity.
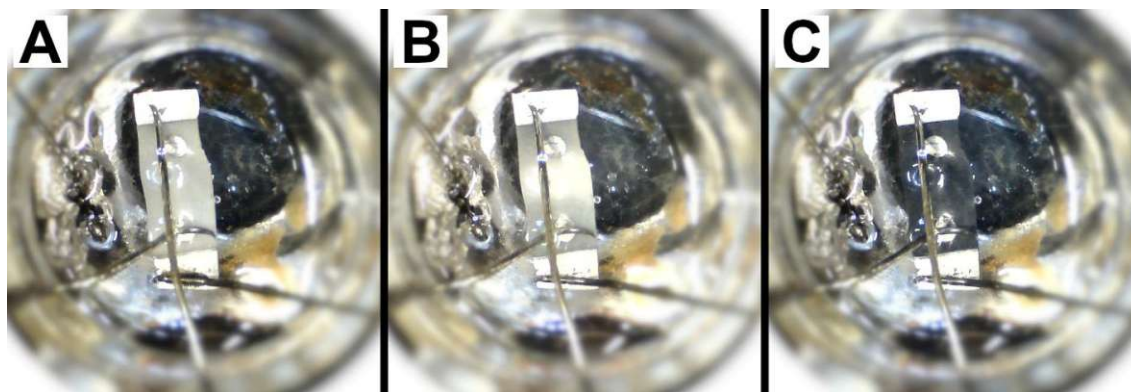
Figure 12: Photographs of the LLTO sample with Pt stripe electrodes. Panel (A) shows the pristine sample inside the air-tight measuring chamber. The two stripe electrodes were short-circuited and act as one working electrode for electrochemical reduction. Upon reduction a coloration front emerges at both Pt stripes, as can be seen in panel (B) for δ=$4 \cdot 10^{-4}$. Panel (C) shows the sample at δ=$1.2 \cdot 10^{-2}$.

Impedance spectra were collected in configuration B for all levels of δ. The impedance spectrum of the pristine sample (s. Figure 14a, δ = 0) shows a high frequency intercept and a steep linear rise towards low frequencies, which is typical for ion conductors with ion blocking electrodes. In our specific situation, i.e. in the cell with organic electrolyte (configuration B), the high-frequency offset of the pristine sample represents the combined Li conduction of the LLTO sheet and the much more conductive liquid $LiPF_6$ electrolyte. Thus, it is not representative for the LLTO ionic conductivity. The latter was determined in separate across plane impedance measurements outside the cell (not shown), with electrodes on the two large sides of a sample; this lead to a total ionic conductivity of about $5 \cdot 10^{-4}$ S/cm.
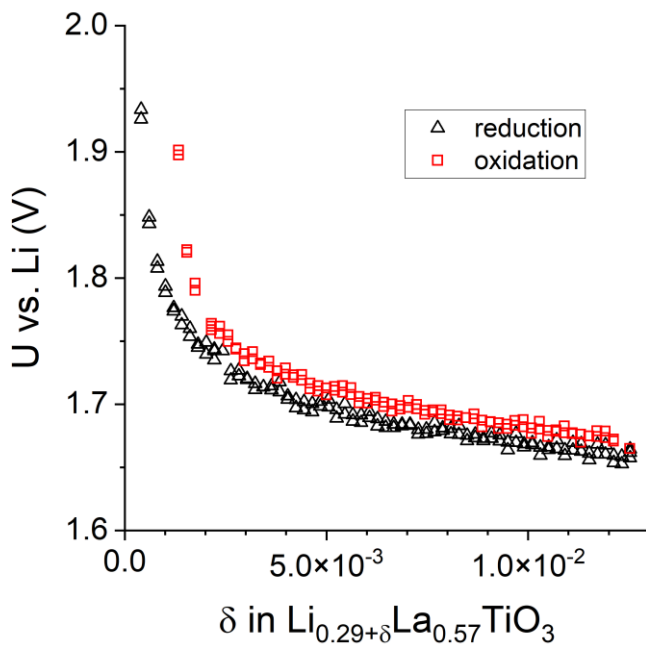
Figure 13: Galvanostatic titration curve, with reduction (black triangles) and oxidation (red squares). The reduction and subsequent oxidation curves coincide, except for the last few data points of the oxidation. The latter is attributed to inhomogeneous oxidation of the sample, caused by insufficient electron conductivity when approaching the intrinsic stoichiometry.

The impedance spectra of LLTO samples in configuration B change drastically as soon as LLTO becomes slightly reduced (s. Figure 14). This can be mainly attributed to an increase of electron conductivity of LLTO, since the Li ion conductivity of the LLTO does not change significantly with increasing Li-content[28] and the organic electrolyte does not conduct electrons. It is shown in Figure 14, that already for very small degrees of reduction ($\delta = 8 \cdot 10^{-4}$), the impedance spectrum virtually reaches the x-axis at low frequencies. A distorted arc is then found towards high frequencies, followed by a high frequency intercept. The high frequency intercept includes conduction across both the organic electrolyte (via ions) and LLTO (via electrons) and is not further considered. The low frequency intercept, i.e. the DC resistance, however, only includes electron flux in LLTO and allows calculation of the LLTO electronic conductivity. This DC resistance shrinks drastically with further reduction, and accordingly also the relevance of the organic electrolyte at higher frequencies and thus the size of the distorted medium frequency arc. Consequently, direct electronic current between the Li ion blocking Pt electrodes dominates most of the impedance spectra.
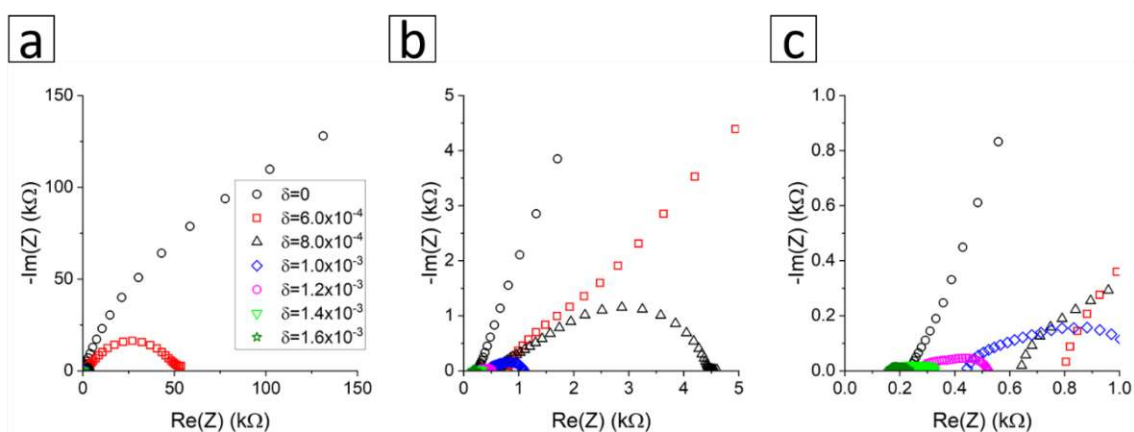
Figure 14: Nyquist plots of the impedance response recorded at various stoichiometries, including the pristine sample ($\delta=0$). Panels (b) and (c) are zoomed versions of panel (a). The black triangles correspond to a stoichiometry of $\delta=8 \cdot 10^{-4}$ and mark the first impedance spectrum characteristic for a mixed conductor with the DC resistance reflecting electron conduction. Further reduction does not change the qualitative characteristics but further decreases the overall impedance response.

The electronic resistance R_e was used to calculate the electronic conductivity σ_e from the sample geometry, assuming one dimensional charge transport, i.e. using the sample width and thickness (5 mm, 0.5 mm) and the electrode distance (10 mm). The resulting values of σ_e are plotted as a function of δ in Figure 15. Further reduction clearly leads to higher electron conductivity and the relationship between electron conductivity and concentration is linear at lower concentrations. Remarkably, the electronic conductivity has a nonzero intercept at a δ-value of approximately $7 \cdot 10^{-4}$. We assume that this offset is caused by electrons which are trapped in deep electronic states in the band gap, thus resulting in no significant contribution to electron conduction.

So-called trap states are a common phenomenon in semiconductors and it is plausible that also in LLTO such states exist, caused by various kinds of defects (e.g. oxygen vacancies or transition metal impurities). As long as the Fermi level is in the range of these trap states, only very few electrons (Ti'_{Ti}) are mobile. Only when all trap states are filled, further electrons are largely injected into the conduction band, giving rise to substantial electronic conductivity. Accordingly, we may subtract the supposed trap state density (i.e. the x-axis intercept of $\delta_{trap} \approx 7 \cdot 10^{-4}$, corresponding to a trap concentration of $\approx 1.2 \cdot 10^{19}$ cm^{-3}) from the total electron concentration in order to obtain a scale of the Ti^{3+} = Ti'_{Ti} concentration, s. Figure 15.
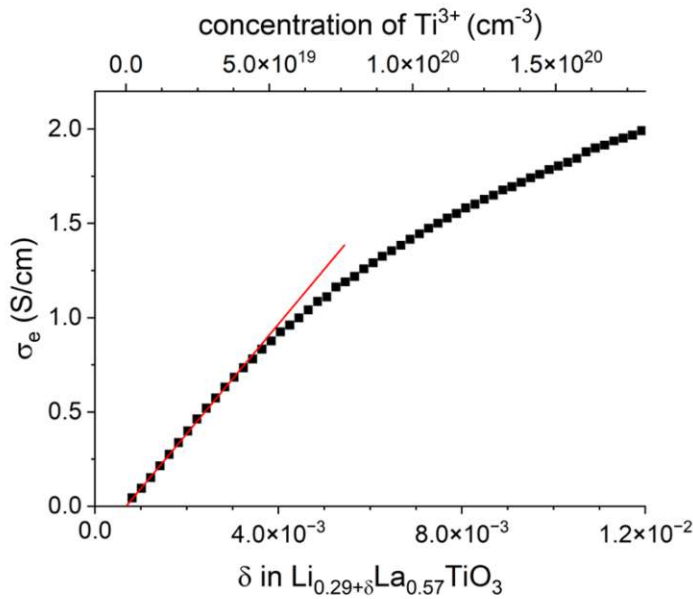
Figure 15: Electronic conductivity of the LLTO as a function of stoichiometry or free electron (Ti^{3+} = Ti'_{Ti}) concentration, respectively. The red line shows the fitting result of the linear part, from which the electron mobility can be approximated.

From the slope of the linear part, an electron mobility u$_e$ can be calculated by means of

$$u_e = \frac{d\sigma_e}{d[Ti'_{Ti}])} \cdot \frac{1}{F} \cdot V_M \qquad (3.12)$$

and a value of about 0.11 cm^2/Vs results. This is significantly lower than the electron mobility of donor-doped perovskites such as Nb-doped SrTiO$_3$ (6 cm^2/Vs)[72] We attribute this difference to the much higher local disorder in LLTO, due to the mixed A-site ions, which likely increases the concentration of electron scattering centers and promotes polaronic self-confinement of the electronic carriers. When LLTO is further reduced, the slope of the $\sigma_e(\delta)$ curve flattens, starting at $[Ti'_{Ti}]$ concentrations of about 3·10^{-3}. This may be caused by a further lowering of the mobility due to increasingly strong interactions between the defects.

3.5.2 Thermodynamics of Li insertion into LLTO

For a more complete picture of the Li insertion into LLTO, we may extend the analysis beyond the range of our own highly resolved data in a limited δ-range by also considering literature values[28] until all vacant A-sites are filled (i.e. δ = 0.14). The corresponding data are shown in Figure 16. At higher Li excess concentrations, the U(δ) curve changes from a logarithmic to an almost linear regime. The simple defect chemical model (Equation (3.5)), black dotted line in Figure 16, only poorly describes the equilibrium voltage. This is largely not due neglecting trap states but caused by defect interaction. Activities rather than concentrations should thus be used.
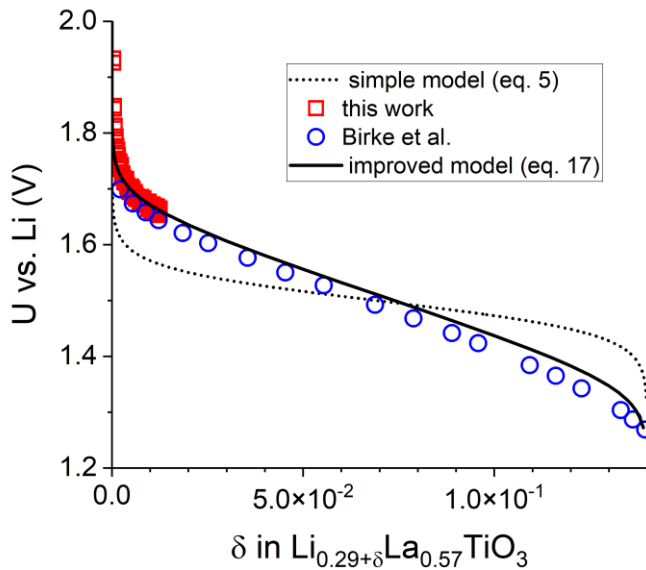
Figure 16: Experimental equilibrium voltage of LLTO vs. Li metal as function of δ from this study (red squares) and Birke et al. [28] (blue circles). The solid black line indicates the modified model according to Equation (3.5), whereas the dotted line corresponds to Equation (3.17).

Precise structural refinements by XRD[73] and NMR[74] as well as TEM measurements[75] revealed that the A-site cations do not have a perfectly random distribution, but rather form alternating Li-rich and La-rich layers along the doubled c-axis of the tetragonal perovskite structure. Consequently, the energy levels of A-sites are not exactly identical but may vary,

depending on the configuration of the surrounding nearest neighbors. Many different neighboring Li, La and vacancy configurations are thus possible, and each has different energy levels for a Li ion. Therefore, the chemical potential of Li ions depends not only on the configurational entropy (considered in our simplified model), but also on the energy levels of different A-sites in the disordered LLTO structure (not considered so far). In the simple model behind Equation (3.5) the Li ion chemical potential including site restriction is expressed by

$$\mu_{Li^+} = \mu_{Li^+}^0 + RTln\left(\frac{[Li'_A]}{[V''_A]}\right) = \mu_{Li^+}^0 + RTln\left(\frac{0.29+\delta}{0.14-\delta}\right). \tag{3.13}$$

When correcting the individual Gibbs free energy of Li ions $\mu_{Li^+}^0$ (i.e. the chemical potential without configurational term) by a linearized approach, we can write instead

$$\mu_{Li^+} = \mu_{Li^+}^0 + a\delta + RTln\left(\frac{0.29+\delta}{0.14-\delta}\right). \tag{3.14}$$

Implementing this into Equation (3.5) we get

$$U_{LLTO} = -\frac{\Delta_R G_{red}^{\emptyset} - a\delta}{F} - \frac{RT}{F}\ln\left(\frac{(0.29+\delta)[Ti'_{Ti}]}{(0.14-\delta)(1-[Ti'_{Ti}])}\right). \tag{3.15}$$

For overlithiation values δ larger than the trap concentration δ_{trap} we may approximate the Ti^{3+} fraction by

$$[Ti'_{Ti}] \approx \delta - \delta_{trap} \tag{3.16}$$

and thus get

$$U_{LLTO} = -\frac{\Delta_R G_{red}^{\emptyset} - a\delta}{F} - \frac{RT}{F}\ln\left(\frac{(0.29+\delta)(\delta-\delta_{trap})}{(0.14-\delta)(1-\delta+\delta_{trap})}\right). \tag{3.17}$$

With this equation, we can reproduce the experimental U(δ) curve very well, see Figure 16. From a fit of all experimental data (literature and our measurement) to Equation (3.17), we obtain $\Delta_R G_{red}^{\emptyset}$=-153.4 kJ/mol, and $a = -145\frac{kJ}{mol}$. A fitting of the experimental data from Birke et al.[28] solely gives almost the same values ($\Delta_R G_{red}^{\emptyset}$=-151.4 kJ/mol and $a = -145\frac{kJ}{mol}$, respectively). Notably, it is also possible that repulsive interaction between Ti^{3+} ions increases with increasing concentration, so our model is just a tentative phenomenological

characterization of the observed U-δ curves. Nonetheless, it allows for a simple, analytical description of the defect thermodynamics and in the following also of the chemical diffusion of Li ions.

3.5.3 Determination of the electrolytic domain boundary

We now have an analytical thermodynamic model, which describes Li insertion into LLTO. Moreover, we have data of the electron mobility and the electronic conductivity in the δ-range, where the electron conduction strongly exceeds the ionic one. However, we still have to discuss the electrolytic domain boundary U_{db}, which we defined by an electronic transference number of 0.01. Experimental data of the electronic conductivity are not available, but we can use our thermodynamic model to calculate electronic defect concentrations and thus electronic conductivities. More specific, we already derived equations for U_{db} and δ_{db} (Equations (3.10) and (3.9)) in the framework of our simplified defect model. Since we face very low δ-values at the electrolytic boundary, we can neglect defect interactions and do not have to switch to Equation (3.15). From our experimentally determined values of the electron mobility (u_e = 0.11 cm^2/Vs) and $\Delta_R G_{red}^{\emptyset}$ = -153.4 kJ/mol we obtain $[Ti'_{Ti}]_{db}$ = 1.7·10^{-8} and a limiting voltage U_{db} = 2.05 V. (Please note that the Li excess at the domain boundary is much higher than $[Ti'_{Ti}]_{db}$ and approximately given by $\delta_{trap} \approx 7 \cdot 10^{-4}$, see above.) Accordingly, the limiting voltage is substantially above the characteristic lithiation plateau of LLTO. This prevents usage of LLTO as an electrolyte for anode materials with reasonably low potentials, i.e. not only silicon or graphite anodes but also $Li_4Ti_5O_{12}$.

More general, we can calculate the Ti^{3+} concentration and thus the electronic conductivity and ionic transference number as a function of the voltage vs. Li metal at voltages, where measurement results are not available. For very low δ and $[Ti'_{Ti}]$, Equation (3.6) simplifies to

$$U_{LLTO} = -\frac{\Delta_R G_{red}^{\emptyset}}{F} - \frac{RT}{F}\ln\left(\frac{0.29[Ti'_{Ti}]}{0.14}\right) \tag{3.18}$$

i.e. we can express $[Ti'_{Ti}]$ in dependence of U_{LLTO} and get for the electronic conductivity

$$\sigma_e = \frac{0.14}{0.29} \cdot u_e \cdot \frac{F}{V_M} \cdot \exp\left(-\frac{\Delta_R G^{\emptyset}_{red} + FU_{LLTO}}{RT}\right). \tag{3.19}$$

Assuming a constant Li total conductivity of $5 \cdot 10^{-4}$ S/cm, also the Li transference number can thus easily be derived. The results of this approximative model are shown in Figure 17, together with our experimental data and extrapolated into the regime of very low electronic conductivity and thus significant ionic transference numbers. The linear range of the experimental σ_e data agrees well with the model described by Equation (3.19).

3.5.4 Li chemical diffusion coefficient of LLTO

It was already reported in literature that LLTO exhibits a high Li chemical diffusion coefficient in the mixed conductivity regime[28]. This is largely caused by the high ionic conductivity of LLTO. Combined with the absence of any phase transitions during lithiation up to $\delta = 0.14$, this is a highly interesting property with regard to applications of LLTO as anode in batteries or in electrochromic devices. Here, we consider the chemical diffusion coefficient by applying our novel U-δ model (Equation (3.15)) and by additional measurements. Experimentally, we use the galvanostatic intermittent titration technique (GITT). Time dependent voltages are shown exemplarily in Figure 18a.
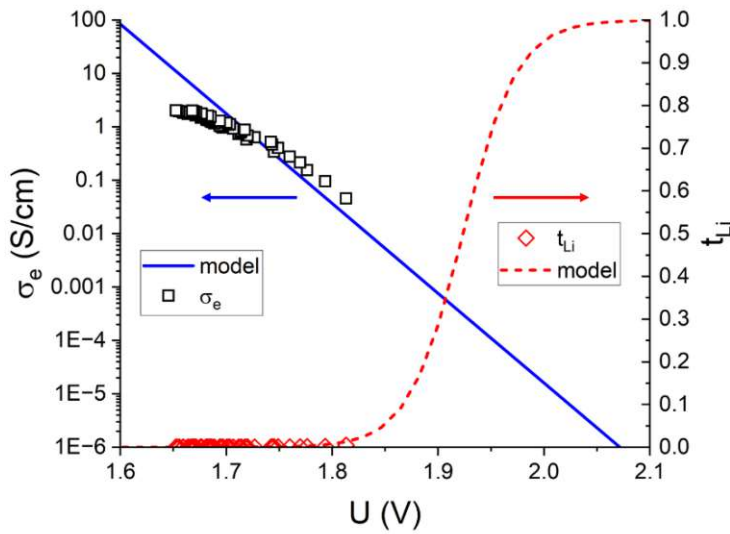
Figure 17: Left axis, showing electronic conductivity: Experimental data (black squares) and results from Equation (3.19) (blue solid line). Right axis, showing the ionic transference number: Experimental data (red diamonds) and results from our defect chemical model (dashed red line).

The galvanostatic curves were evaluated as suggested by Weppner et al[28], i.e. by using the equation

$$\widetilde{D}_{Li} = \frac{4}{\pi}\left(\frac{I_{DC}V_m}{FA_{surf}}\right)^2 \cdot \left(\frac{dU_{eq}}{d\delta}\right)^2 \cdot \left(\frac{dU}{d\sqrt{t}}\right)^{-2}. \tag{3.20}$$

The results are plotted in Figure 18b. For comparison, chemical diffusion coefficients from Ref. [28] are presented as well (black squares). Both data sets show an almost constant diffusion coefficient in a broad range of δ-values, even though absolute values differ by almost a factor of 10. Here, several non-idealities might come into play, e.g. a charge transfer resistance, or too long galvanostatic pulse duration, as critically reviewed in literature[76].

The Li diffusion coefficient can also be directly calculated from the partial electron and ion conductivities and the slope of the U(δ) curve according to [77,78]:

$$\widetilde{D}_{Li} = \left(\frac{1}{\sigma_e} + \frac{1}{\sigma_i}\right)^{-1} \cdot \frac{dU_{LLTO}}{d\delta} \cdot \frac{V_m}{F}. \tag{3.21}$$
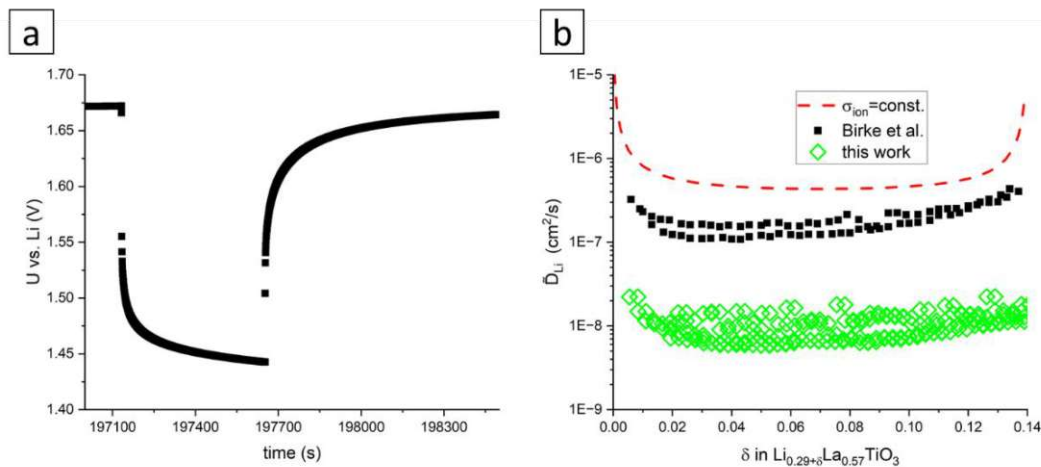
Figure 18: (a): Examplary voltage vs. time of a GITT step, showing the end of a relaxation period, a galvanostatic reduction period and another relaxation period. (b): Chemical diffusion coefficient of LLTO from the GITT measurements in this work and by Birke et al.[28]. For comparison the lines display calculated values based on the model of Equation (3.17) and ionic bulk or total conductivities.

For calculating $\frac{dU_{LLTO}}{d\delta}$ we can use our analytical model, i.e. Equation (3.17) with experimentally determined parameters. The electronic conductivity is orders of magnitude higher than the ionic conductivity for most degrees of reduction and can thus be neglected in Equation (3.21). The Li ion conductivity, on the other hand, is only known for $\delta = 0$. With higher Li occupancy, the conductivity might change, due to a decrease of the Li vacancy concentration, in combination with an altered (most likely higher) vacancy mobility at higher A-site occupation. Nevertheless, a constant ionic conductivity of $5 \cdot 10^{-4}$ S/cm was used to calculate the chemical Li-diffusion coefficient. In accordance with the measurements, a certain increase of the chemical diffusion coefficient towards $\delta = 0$ is predicted by the model, cf. Figure 8b. Also the rather constant value in a broad lithiated range is reproduced. However, the absolute value is significantly higher than the measured data. This may again indicate that GITT measurements are prone to some errors. Still, all obtained values are large compared to Li diffusion coefficients reported for typical cathode materials (e.g. $LiNi_{0.33}Mn_{0.33}Co_{0.33}$), which are typically in the order of 10^{-11} to 10^{-9} cm²/s [76], or for graphite anodes (10^{-12}-10^{-10} cm²/s) [79]. Accordingly, we can expect excellent rate

capability of LLTO when being used as an anode, which was recently confirmed experimentally.[68]

3.6 Conclusions

Even though lithium lanthanum titanate is largely known as a solid state electrolyte, it has a highly interesting mixed conductivity regime and may thus also serve as an electrode material in different electrochemical cells. In this study, we investigated details of the transition of LLTO from its electrolytic to its mixed conducting electrode-like domain. The voltage dependent composition and electronic conductivity was measured by a combination of galvanostatic titration vs. Li and impedance measurements. The domain boundary is already reached for a Ti^{3+} fraction in $Li_{0.29+\delta}La_{0.57}TiO_3$ as low as $1.7 \cdot 10^{-8}$, corresponding to a voltage vs. Li of 2.05 V. The corresponding Li excess, however, includes filling of electron traps in the band gap. Those can be deduced from the lithiation dependent electronic conductivity measurements and a value of $\delta_{trap} = 7 \cdot 10^{-4}$ is found. Only after filling these traps states, significant amounts of Ti^{4+} are reduced to Ti^{3+}.

An improved defect chemical model was developed for the Li insertion reaction, which includes a concentration dependent defect interaction term (i.e. activities). This model can describe the degree of lithiation as a function of the Li chemical potential, i.e. voltage vs. Li metal and yields the corresponding standard Gibbs free energy of the reaction with respect to Li metal, $\Delta_R G^{\emptyset}_{red} = -153$ kJ/mol. The electronic conductivity of LLTO increases linearly with increasing δ up to ca. $\delta = 3 \cdot 10^{-3}$ and an electron mobility of 0.11 cm^2/Vs can be derived. For stronger lithiation, defect interaction reduces the electron mobility and thus also the increase of electronic conductivity with δ. Moreover, the composition dependent Li chemical diffusion coefficient of LLTO was determined by GITT measurements and calculations based on the deduced thermodynamic data and conductivities. These data confirm that the Li chemical diffusion is orders of magnitude faster than in other typically used electrode materials, primarily because of the high Li ion conductivity.

4 On the electrochemical stability of the Li-electrolyte Li$_7$La$_3$Zr$_2$O$_{12}$

This chapter largely corresponds to a manuscript to be submitted to a peer-reviewed journal (authors: J. Ring, A. Bumberger, M. Kubicek, H. Hutter, T. Schachinger, V. Vonk, S. Volkov, A. Nenning and J. Fleig).

4.1 Introduction

Cubic Li$_7$La$_3$Zr$_2$O$_{12}$ (LLZO) based garnet electrolytes are promising candidates for solid state batteries[12,13,80,81], due to their high ionic conductivity and stability towards Li metal anodes[82]. The stability of LLZO towards high voltage cathodes, however, is less clear. According to DFT calculations[1,22], the thermodynamic stability window of LLZO ranges only up to 3-3.3 V vs. Li metal, whereas experimental studies with ion blocking electrodes reported a stability window up to 5-6 V vs. Li metal[12]. The practically usable voltage range of LLZO electrolytes and the mechanisms causing decomposition are thus important unresolved question.

A recent study has shown that LLZO undergoes electrochemical decomposition when a voltage of ca. 4.1-4.3 V vs. Li metal is applied to an inert Au-electrode at 300 °C [23]. This decomposition takes place via oxygen evolution and Li depletion, possibly partly within the garnet phase but also by forming La$_2$Zr$_2$O$_7$ and La$_2$O$_3$. At the cathode, Li-salts, such as Li$_2$O, LiOH or Li$_2$CO$_3$ are formed, where the latter two products also involve H$_2$O, respectively CO$_2$ from the atmosphere. These studies clearly show the instability of LLZO at high potentials, but the detailed decomposition mechanism is still only partly understood, particularly with regard to mechanistic drivers, voltage/time and factors enhancing or inhibiting degradation.

For this, we conducted in-situ synchrotron XRD experiments to further elucidate the structural changes during degradation of LLZO. DC voltage was applied between small working electrodes and larger counter electrodes to observe time-resolved structural

changes caused by the electric field stress. Afterwards, ^{18}O isotope tracer exchange experiments with subsequent time of flight secondary ion mass spectrometry (ToF-SIMS) analysis was performed to gain information about possible changes of oxygen vacancy concentration. Furthermore, by means of transmission electron microscopy (TEM), energy dispersive X-ray analysis (EDX) and electron energy loss spectroscopy (EELS), more detailed structural and chemical information about the decomposed LLZO was obtained. These findings contribute to a better understanding of the electrochemical decomposition of LLZO and show that an amorphization is taking place before the formation of a crystalline $La_2Zr_2O_7$ phase.

4.2 Materials and methods

Polycrystalline pellets (10 mm diameter, 0.5 mm thick) of Ta-doped LLZO with the nominal stoichiometry $Li_{6.4}La_3Zr_{1.4}Ta_{0.6}O_{12}$ (Toshima Manufacturing Co.) were used in this study. All pellets were freshly polished to remove any reaction layers on the surface prior to electrode deposition. Li-blocking Au-electrodes were deposited by magnetron-sputtering on both sides of the cylindrical pellets. One side was completely covered with gold (~15 mm^2) whereas the opposite side was partially covered with a shadow mask to prepare several smaller electrodes (~0.4 mm^2 each). For all polarization experiments, these small electrodes were used as working electrodes and the larger ones as counter electrodes.

Ex-situ polarization experiments were done at temperatures from 25 °C to 289 °C in air and under nitrogen atmosphere with voltages ranging from 0.5 V to 3 V for several hours, prior to XRD characterization. All XRD experiments were carried out at the synchrotron DESY, beamline P08. Therein, a highly collimated (30x30 μm^2) X-ray spot with 15 keV was focused on a Au electrode in shallow incidence (5° angle of incidence) mode, which results in a mean X-ray penetration depth of 2 μm. Diffraction patterns were collected by movement of a 2-d detector (Pilatus100K, 195x487 pixels) along the Θ axis at constant angle of incidence. Beside crystallographic characterization of the pre-polarized samples, multiple in-situ XRD experiments were done at 300 °C in nitrogen atmosphere, applying direct voltages up to 3 V while simultaneously monitoring crystallographic changes by micro-focused XRD. The

samples were heated to 300 °C during these experiments to facilitate decomposition reaction rates in reasonable time frames, whereas the nitrogen atmosphere was used to avoid possible reactions with air (i.e. O_2, CO_2 or H_2O).

A cross sectional (going from the gold electrode into the LLZO underneath) TEM-sample was prepared via focused-ion-beam milling from an electrode of a sample, which was polarized with 2 V for 2 hours at 300 °C in synthetic air. Various TEM techniques, including STEM-EELS, were applied using a TFS/FEI TECNAI F20 microscope equipped with an X-FEG field emission source, a Gatan RIO 16 CMOS camera, an EDAX Apollo XLTW EDX detector and a Gatan GIF Tridiem spectrometer. All measurements were done at 200 kV.

After XRD experiments, a sample (polarized with 2 V and 3 V under nitrogen at room temperature) and another sample (polarized with 2 V and 3 V in synthetic air at 300 °C) were used for ^{18}O-tracer exchange experiments. Prior to tracer exchange, the gold micro-electrodes were scratched from the surface to fully expose the underlying LLZO to the $^{18}O_2(g)$. After a pre-annealing step in air at 350 °C for 20 hours, the sample chamber was evacuated and refilled with ^{18}O-tracer gas (97.1% isotope-enriched, CAMPRO) several times. Finally, the sample chamber was filled with $^{18}O_2$ 0.2 bar and heated to 350 °C. There the samples were kept at 0.2 bar for 1 hour to enable oxygen isotope exchange.

4.3 Results and discussion

4.3.1 In-situ XRD

Generally, diffractograms from in-situ and ex-situ (with prior polarization) experiments are congruent, i.e. the effect of polarization is identical, despite slight differences in experimental parameters (polarization time, atmosphere, temperature). Therefore, we concentrate on the in-situ results herein.
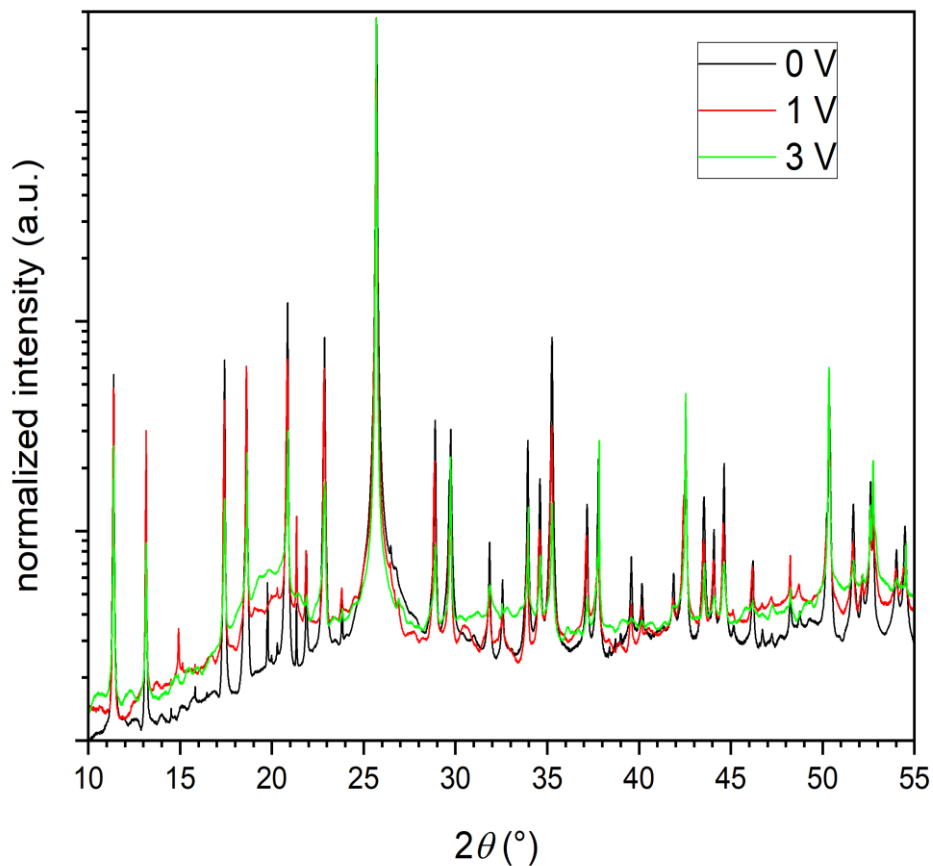
Figure 19: Diffractograms from the in-situ XRD measurements at 300 °C. Intensities were normalized to the intensity integral of the Au-(111) reflex (reflex at around 25.5 °). Beside the intense Au-(111) reflex and two minor Li_2CO_3 reflexes (s. SI for details), all significant reflexes can be assigned to the LLZO structure (space group Ia-3d)[6]. A diffuse and increasingly strong background signal at angles around 20° arises during polarization, suggesting partial amorphization of the material.

Figure 19 shows diffractograms obtained with x-rays focusing on a polarized Au electrode. The electrode was anodically polarized at 300 °C with 1-3 V for several hours. For better comparability with standard lab-based diffractograms, selected diffractograms were converted to show diffraction angles, as would be obtained using Cu-K$_\alpha$ X-ray source ()s. Figure 20). From an electrochemical point of view, this leads to a depletion of Li ions

beneath the electrode[23]. Moreover, a species has to be oxidized, most probably oxide ions by forming oxygen molecules[23]. This nominal Li_2O depletion may cause secondary phases[23]. In our experiments, all reflexes from the cubic LLZO[6] persist, whereas no significant new reflexes appear during polarization. Consequently, the formation of crystalline decomposition phases can be excluded. However, the intensity of most LLZO reflexes diminish, while their width increases. All diffractograms shown here, have been normalized to the intensity integral of the Au-(111) reflex, which is arguably unaffected by application of electric field-stress. With this normalization, it is reasonable to compare the reflex intensities. Moreover, an increasing, diffuse background signal at lower diffraction angels is apparent. In conjunction with the broadening and diminishment of the LLZO reflexes, this strongly suggest a decrease of crystallinity, or amorphization of the LLZO respectively. In contrast to these results, secondary phases were found in an earlier, similar study [23]. There, however, much longer polarization times were used (120 h). Accordingly, the total charge flow, i.e. Li depletion was more pronounced there. Furthermore, the longer polarization time may facilitate crystallization of secondary phases because the sample was heated to 300 °C, potentially providing enough thermal energy to overcome crystallization energy barriers. Possibly, there are two stages of decomposition: a first stage with amorphization of the garnet and a second one with true second phase formation of $La_2Zr_2O_7$ and La_2O_3. However, in both cases oxygen has to evolve during this anodic reaction.
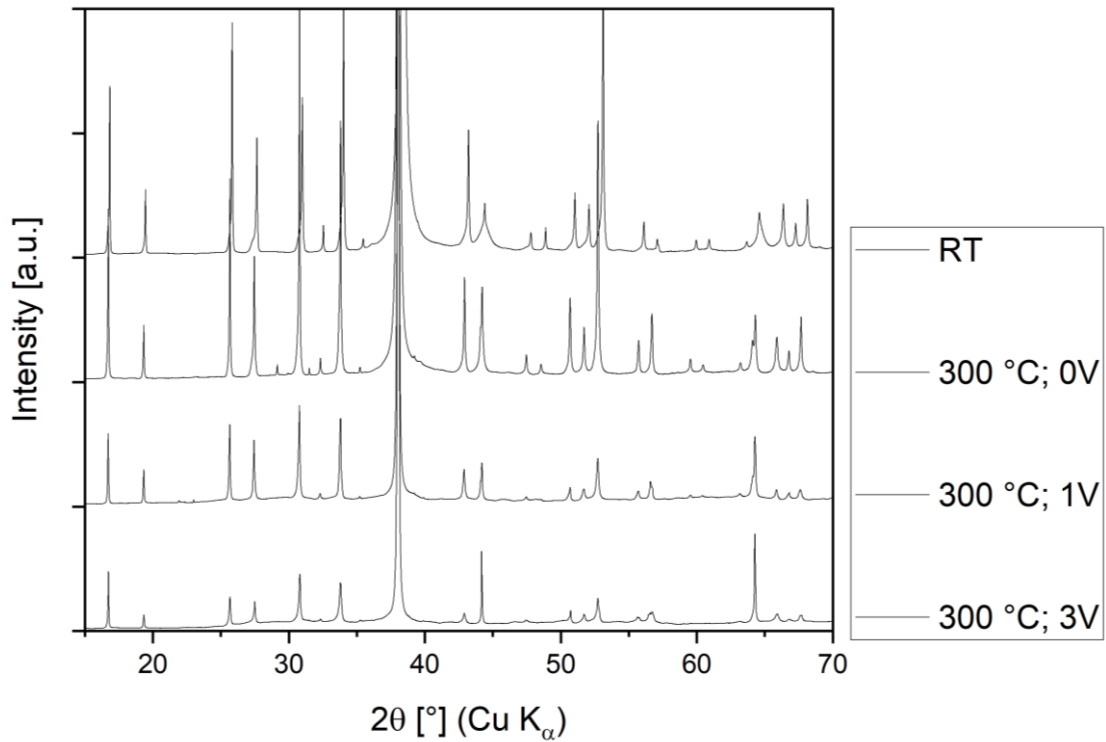
Figure 20: Diffractograms with diffraction angles converted to simulate results of a Cu-K$_\alpha$ X-ray source.

During heating of the sample to the experiment temperature of 300 °C, reflexes corresponding to Li_2CO_3 appear, indicating a crystallization of Li_2CO_3. Since LLZO is known to react with CO_2, forming lithium carbonates at the surface, it seems likely that lithium carbonates were already present between the Au-electrode and the bulk LLZO before the XRD experiments. However, at room temperature (s. Figure 21) there were no signs of crystalline Li_2CO_3, suggesting the carbonate layer was either amorphous, or not existent prior to heating. Interestingly, all reflexes attributed to Li_2CO_3 vanish during the field-stress experiments. This is most probably due to an electrochemical decomposition (oxidation) of Li_2CO_3 at the anode (positive electrode), by release of CO_2 (g) and O_2(g) and a drain of excess Li^+ ions towards the cathode (negative electrode). Additional amorphization of remaining Li_2CO_3 may also occur.
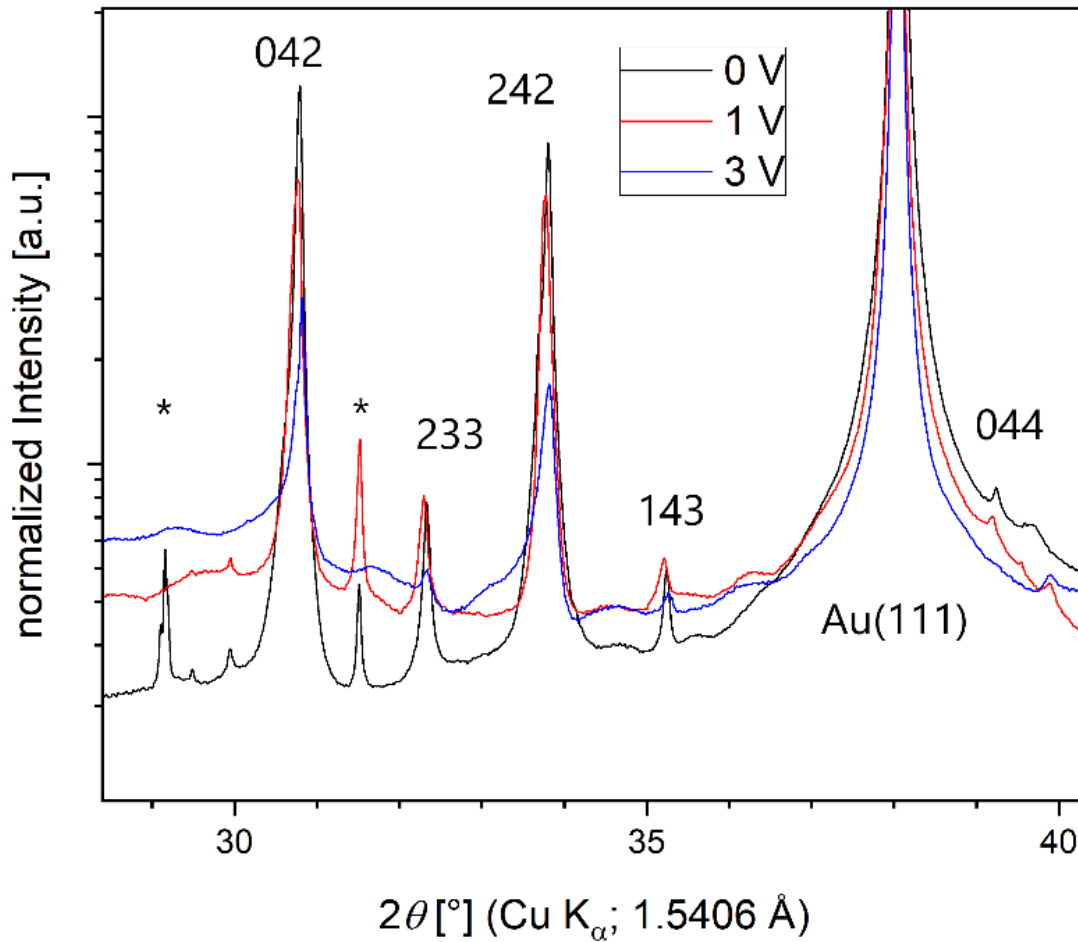
Figure 21: Diffractograms of a sample at 300 °C. Reflexes at 29.2° and 31.5°, marked with asterisks, correspond to Li_2CO_3 reflexes (111) and (002) respectively. The Li2CO3 reflexes appear as a result of heating and disappear during polarization.

4.3.2 TEM, STEM-EELS, STEM-EDX, SAED

Using a combination of STEM, EDX and EELS, the elemental composition was mapped across an area beneath a polarized electrode (2 V for 2 hours at 300 °C), going approximately 1.2 µm deep into the LLZO (s. Figure 22). The lateral distributions of the elements Li, La, Zr and O were of primary interest, but since Li did not yield significant signals with either technique, no meaningful information about the Li distribution is available. Beside La, Zr

and O, also C signals were detected in both EELS and EDX spectra. The carbon signals primarily originate from the surface region, spreading into the LLZO to a depth of approximately 200 nm. The very same region shows a considerably lower signal intensity of both La and Zr. Considering the well-known carbonate formation on LLZO surfaces and the EELS/EDX data, it is reasonable to assume this surface region consists of Li_2CO_3. However, seeing that selected area electron diffraction (SAED) does not show any signs of crystalline Li_2CO_3 phases, the carbonate phase must be mainly amorphous (s. SI). This agrees with the presented XRD data insofar, as the reflexes originating from crystalline Li_2CO_3 that are observable before, fade away upon polarization.

Signals from Zr and La are close to homogeneous across large parts of the surveyed region. The O signals, however, show a clear tendency when comparing the surface region to the deeper regions. Apart from the O-rich carbonate phase, the O content decreases considerably, when approaching the surface. Averaging the 2D-map of the O content into a 1D-graph shows this trend even more clearly. From thermodynamic data, oxygen loss is expected to occur when oxidative field-stress is applied[1]. As already mentioned, a concerted O and Li depletion at the positive electrode is most likely. However, the formation of crystalline decomposition phases seems to be absent, at least in this phase of decomposition. Rather LLZO seems to decompose into an oxygen-deficient amorphous phase.
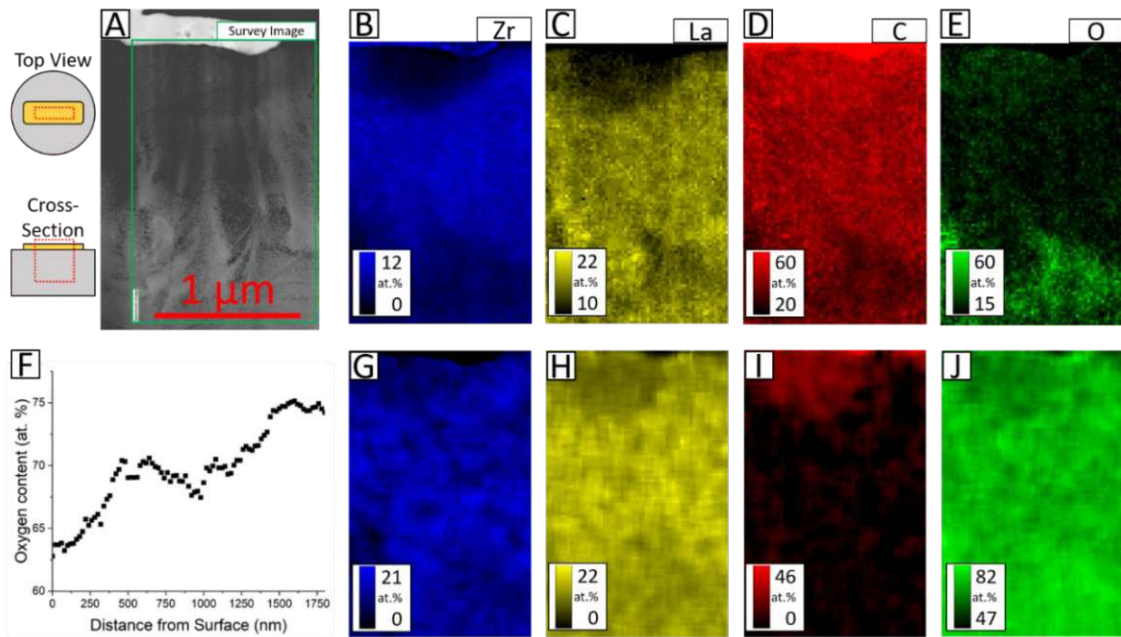
Figure 22: (A): Annular dark-field STEM-micrograph of the cross-sectional sample, showing multiple grains of LLZO with parts of the Au electrode on top. Most irregularities (branching patterns) are caused by sample preparation (i.e. focused ion beam milling), while some others (pores) might originate from material synthesis or field-stress experiments. The region of interest, which was examined spectroscopically, is highlighted with a green rectangle (beneath a Au electrode polarized by 2 V for 2 h at 300 °C). (B-E): STEM-EELS maps of Zr (blue), La (yellow), C (red), and O (green). (F): Oxygen concentration profile from an EDX line-scan, starting at the surface and going 1.8 μm deep into the sample. (G-J): STEM-EDX maps of Zr (blue), La (yellow), C (red), and O (green) from the same sample area as the STEM-EELS maps.

SAED experiments reinforce the assumption of amorphization even further (s. Figure 23). SAED patterns from near-surface (500-1000 nm deep) regions show little to no diffraction spots but rather a diffuse ring pattern, indicative of (partial) amorphization of these regions. Diffraction patterns from deeper regions (~2000 nm) clearly indicate crystalline LLZO and close to no amorphization. This trend agrees well with the stoichiometry variations observable from both EELS and EDX experiments.
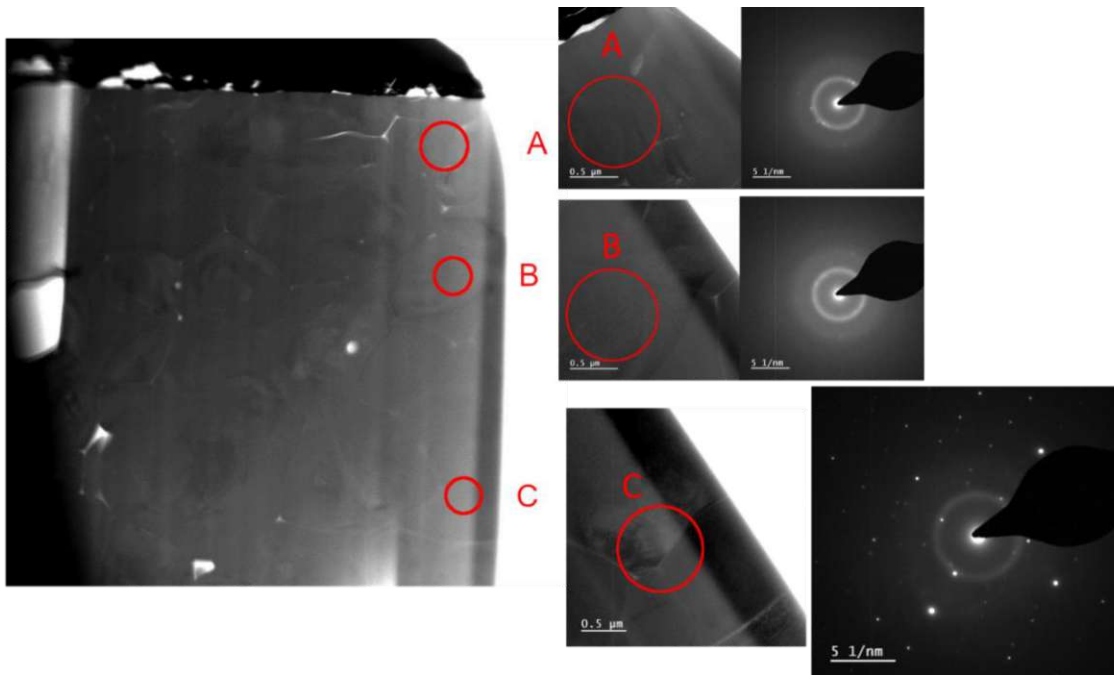
Figure 23: Bright-field TEM-micrographs and corresponding SAED-patterns. The SAED-patterns all show diffuse rings from diffraction at short-range ordered (amorphous) phases. Diffraction spots from crystalline LLZO become more pronounced and bright in areas further away from the surface (electrode).

4.3.3 ^{18}O Tracer exchange and TOF-SIMS

^{18}O-tracer exchange at 350 °C was performed on two samples, subjected to electric field-stress (2 V and 3 V) during the in-situ XRD experiments (s. Chapter "Materials and Methods"). Subsequent TOF-SIMS 3D-profiling at room temperature then reveals the frozen-in distribution of the O isotopes. Since both incorporation and diffusion of ^{18}O requires O vacancies in the LLZO lattice, an increased ^{18}O concentration is indicative of higher defect concentrations. Such an enhanced oxygen vacancy concentration in LLZO is realistic since positively charged oxygen vacancies counterbalance the Li$^+$ depletion, i.e. the negatively charged Li vacancies introduced at the positive electrode upon polarization.

Typical SIMS depth-profiles of ^{18}O tracer concentrations (obtained from a sample polarized with 2 V and 3 V) are shown in Figure 24. All probed regions clearly show significant

incorporation of ^{18}O into LLZO. It is noteworthy, that the profiles (including all profiles not shown here) do not converge towards the natural ^{18}O-isotope ratio of 0.205 %. The higher ^{18}O isotope of approximately 0.4 % even in ~2 μm depth, as well as a continuous slope for the pristine spot B curve indicate fast oxygen diffusion in the LLZO at 350°C. indicate that the samples have already been slightly ^{18}O-enriched prior to the tracer-exchange. We attribute this to the synthesis conditions of LLZO, i.e. sintering in an O_2-containting atmosphere [83,84]. Since bottled O_2 is manufactured via distillation of liquid air, a slight enrichment of ^{18}O is common.
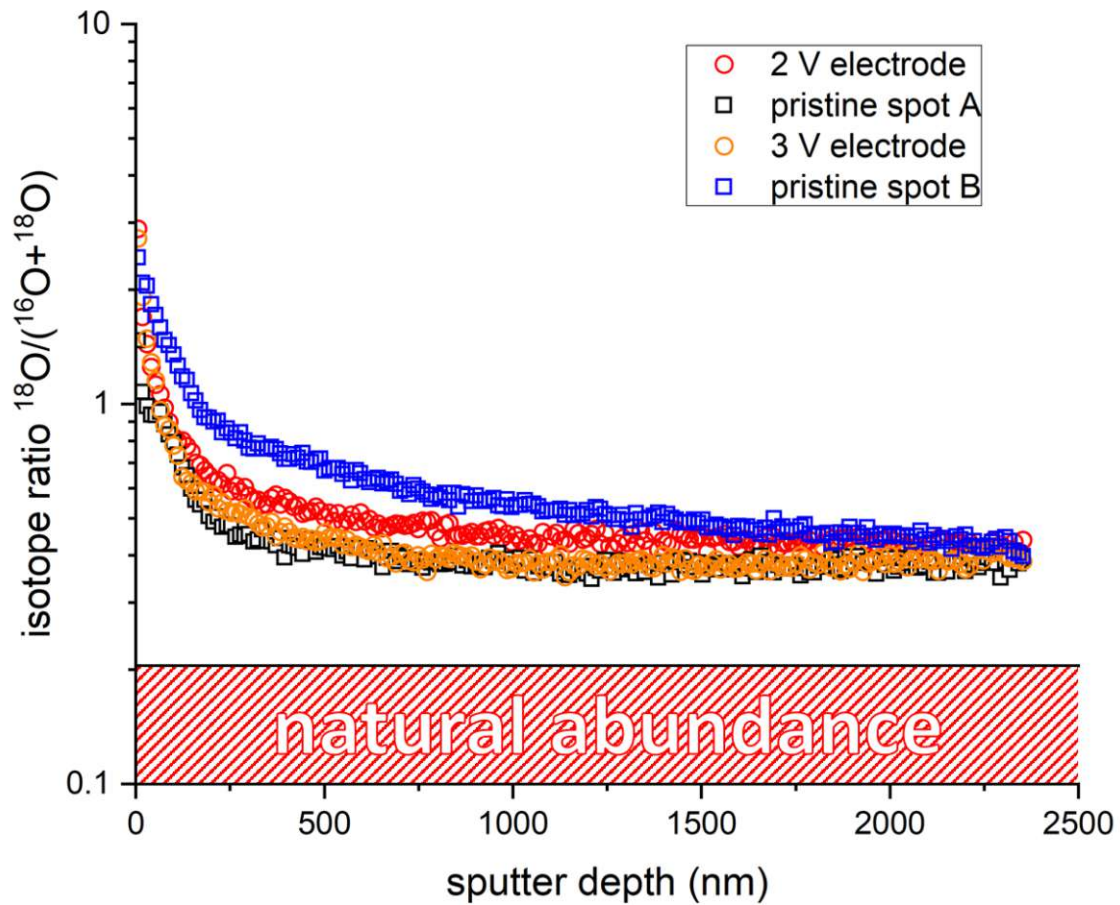
Figure 24: SIMS profiles from two pristine spots and two polarized (2 V and 3 V s. "Materials and Methods") spots of a single sample. Comparison of pristine spots (black and blue squares) show that regardless of field-stress experiments, the rates of incorporation and diffusion of ^{18}O, varies considerably. Sample parts, which were subjected to field-stress prior to tracer exchange (red and orange circles), remain within the scattering range of pristine sample parts.

Taking into account the increased ^{18}O concentration in LLZO prior to the tracer exchange, we still find (additional) ^{18}O enrichment inside the LLZO, as deep as 2000 nm from the surface. This indicates considerable O^{2-} mobility, consistent with previous studies[60]. However, the data found in this study cannot be explained or fitted by a simple incorporation and diffusion model. A near surface (~0-200 nm) region with slower diffusion and a region deeper in the crystal with faster oxygen diffusion can be distinguished, but no uniform tracer surface exchange rate (k*) or diffusion coefficients (D*) can be determined. Furthermore, comparing the data from polarized and pristine parts of

the sample (Figure 24), the difference between two pristine sample parts is more pronounced than the difference between pristine and field-stressed parts of the sample. Therefore, there variability of ^{18}O diffusion and incorporation kinetics is larger than the possible effect of electric field stress.

Essentially, the effect of oxidative field-stress on LLZO can be described as follows (s. Figure 25): Li^+-ions move towards the negative terminal (cathode) and O^{2-}-ions form $O_2(g)$ by releasing two electrons to the positive terminal (anode). The material at the anodic terminal is left with V_{Li}' and $V_O^{\bullet\bullet}$, which leads to a general degradation of the crystal structure, without complete structural collapse into more stable crystalline products, such as $La_2Zr_2O_7$ and La_2O_3. Arguably, kinetic barriers are the reason for this absence of crystalline phase formation.
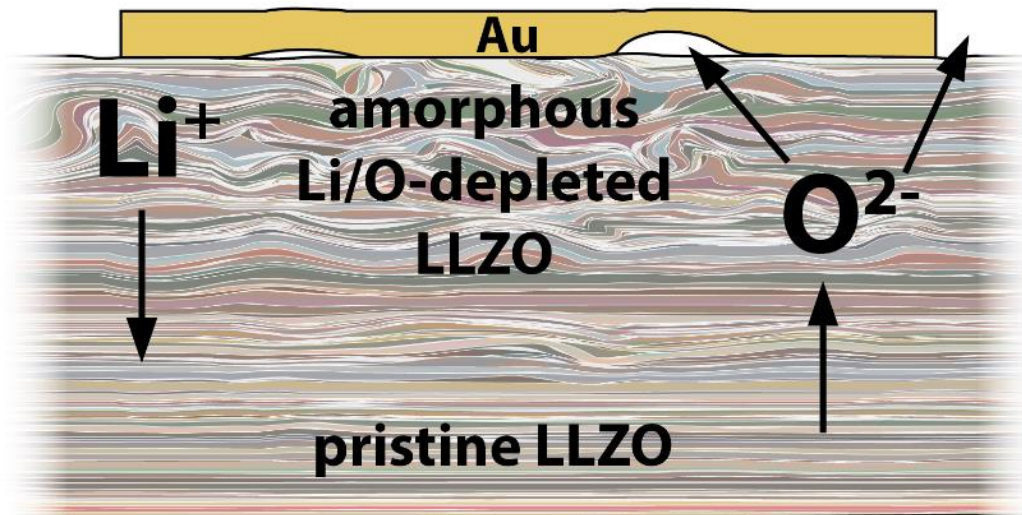
Figure 25: Schematic drawing of the suggested degradation mechanism.

4.4 Conclusion

The combination of techniques (XRD, STEM-EELS, SIMS), applied within this work, elucidate the effect of electric field stress on the structural and chemical properties of LLZO. Results

from micro-focused synchrotron XRD experiments (both in-situ and ex-situ) do not indicate formation of any crystalline decomposition products due to electric field stress. However, the crystallinity of the pristine LLZO does decrease upon field stress. From general observations (gas bubble formation) and thermodynamic data, a decomposition reaction involving oxygen evolution seems reasonable. Indeed, results from both STEM-EELS and SIMS suggest oxygen loss caused by the electric field stress. The degree of oxygen depletion clearly increases when approaching the surface. Furthermore, the results suggest no substantial change of La or Zr stoichiometry, as can be expected considering crystal structural aspects.

5 Incorporation and diffusion of Co in LLZO

5.1 Abstract

The stability of LLZO against cathode materials is a crucial factor for its potential use as an electrolyte for solid state batteries. Especially the formation of interface layers with low ionic conductivity between the electrolyte and electrode materials can impede the practical usability[33,85–89]. In this study we found that LCO thin films on LLZO single crystals undergo a solid state reaction at temperatures as low as 600 °C, resulting in incorporation of significant amounts of Co into LLZO. Co diffuses several micrometers through the LLZO within hours at elevated temperatures. Numerous samples were prepared and subjected to heat treatments (600-700 °C) for up to 48 hours. Subsequently, SIMS analysis was performed, revealing lateral and spatial chemical information. Depth profiles of Co concentrations show considerable Co incorporation and diffusion into and within LLZO. The relationship between annealing temperature and Co diffusivity was investigated, showing faster Co diffusion at higher temperatures.

5.2 Introduction

Solid-state batteries (SSBs) are considered as a key technology for the development of affordable and versatile electrical vehicles with extended driving ranges and improved safety. The main advantage originates from the adoption of a solid electrolytes instead of a flammable organic liquid. Moreover, solid electrolytes may allow the integration of Li metal enabling ultimately high energy densities. However, to reach the promised performance of solid-state batteries suitable solid electrolytes needs to be developed. Oxide-based Li-ion conductors, such as $Li_7La_3Zr_2O_{12}$ and variants (LLZO)[80,90,91], belong to the most promising candidates, due to their unique feature of combining electrochemical stability with rather high Li-ion conductivities (up to 1.3 mS/cm). Further advantages of LLZO are its processibility in air and improved safety at high operating temperatures compared to other solid electrolytes[92–94].

Despite the promising prerequisites of LLZO, its integration into a battery is associated with the formation of complex solid-to-solid interfaces that arise as the main bottlenecks to achieve high power density, rate capacity, and capacity retention of SSBs, which impede their ultimate commercial usage. Whereas for the Li-LLZO interface significant improvements have been achieved, the cathode side still suffers from technical challenges such as poor contact between the LLZO and the cathode or contact loss during cycling due to volume changes within the cathode[35,95–97]. A stable interface contact is a key requirement for high initial discharge capacities. This, however, requires high temperature processing. For sufficient bonding between LLZO and $LiCoO_2$ (LCO), temperatures between 600 to 1050 °C are required.

The high temperatures may result in mutual diffusion and interfacial reactions between the solid electrolytes and the electrode, generally leading to degradation via the formation of an ionically blocking layer. For example, the state-of-the-art cell composed of a composite cathode based on LLZO, LCO and a sintering additive has been shown to suffer from very high interfacial resistance (270 Ω cm^2 at 100 °C), which is predominantly attributed to degradation processes at the high processing temperature of 700 °C[98]. Such values are too high to achieve a target cycling at 1C with more than 90 % efficiency; values as low as 40 Ω cm^2 are required[99].

In addition to the formation of undesired phases related to the decomposition of LLZO, already the sole incorporation of a transition metal into the garnet structure could have significant structural and electrochemical consequences. Considering the potential implications of Co on LLZO, in-depth studies are needed to understand the role of Co in the degradation processes at high temperature and to develop contingency strategies for safe processing of SSBs. For this purpose, we conducted a series of experiments with LCO thin films deposited onto LLZO single crystals. The samples were subjected to heat treatments (600-700 °C) for up to 24 hours. Subsequently, the spatial distribution of elements were determined by time of flight secondary ion mass spectrometry (ToF-SIMS) analysis, revealing the depth profiles of Co-concentration in LLZO.

5.3 Experimental section

Single crystalline $Li_{6.4}Ga_{0.2}La_3Zr_2O_{12}$ garnets were synthesized out of a melt using the Czochralski method by Stefan Ganschow[100] (Leibniz-Institut für Kristallzüchtung, Berlin, Germany), whose contribution is gratefully acknowledged. LCO thin films (ca. 105 nm) were deposited onto freshly polished surfaces of LLZO single crystals by magnetron sputtering at room temperature. More details on the sputter device are given in the next chapter. Afterwards, the samples were annealed in air at temperatures between 600 °C – 700 °C for 24 or 48 hours. The first indication of a possible incorporation of Co into LLZO due to annealing of LCO thin films on LLZO was the formation of a persistent yellow coloration of the underlying LLZO after annealing for 4 hours at 600 °C. Since the yellow color was retained after grinding off the brownish LCO film and hundreds of micrometers of the LLZO substrate, it was evident, that the coloration had spread through large portions of the crystal. Figure 26 shows the different appearance of pristine LLZO, LCO coated LLZO and LLZO after annealing and grinding.

Figure 26: Pristine LLZO (left), sample after annealing with a LCO thin film on top and parts of LLZO removed (middle), and with annealed LCO thin film (right).

After annealing, TOF-SIMS depth profiling of various samples was performed at room temperature by Markus Kubicek (TU Wien, Austria) at the SIMS instrument of Prof. H. Hutter. Their contribution is gratefully acknowledged. Diffusion profile measurements were performed on a TOF.SIMS 5 (ION-TOF, Germany) instrument. 25 keV Bi^+ primary ions were used in spectrometry mode. Areas of 100×100 μm^2 were investigated using a raster of 256×256 measured points. Positive secondary ions and clusters were analyzed up to mass 164 u, and the intensities of all relevant secondary ions and clusters were analyzed simultaneously. Depth-profiling was performed with 2 keV O_2^+ ions (400×400 μm^2,

approximately 850 nA) *via* sequential ablation of the surface between measuring secondary ions in non-interlaced mode. A low energy electron flood gun (21 eV) was used for charge compensation. After TOF-SIMS analysis, the depth of the sputter craters was measured with a stylus profilometer (DekTakXT, Bruker, USA) to convert sputter time into depth.

5.4 Results and discussion

The SIMS depth-profiles of positive secondary ions of Co, Ga, Zr and La, obtained from a sample annealed at 650 °C, are exemplarily shown in Figure 27. Further depth-profiles of Co at various temperatures are shown in Figure 28. All these profiles can be divided into four regimes as indicated by gray lines in Figure 27: (1) A surface layer forming on top which is Li-rich, whereas all other cations shown here are depleted. In accordance with literature, we assume Li-containing salts (i.e. hydroxides and carbonates) as main constituents of this layer. (2) A Co-rich layer, originally pure sputtered $LiCoO_2$, which exhibits a strong gradient in Co as well as significant amounts of Ga, which were incorporated during annealing. (3) An interface layer with a strong decrease of both Co and Ga signals with depth, together with a strong increase of Zr and La signals. (4) Bulk LLZO characterized by a deep and declining profile of Co, indicating incorporation of Co several micrometers into the bulk.

While La and Zr reach constant concentrations at approximately 1000 nm from the interface, Co and Ga signals show opposite trends. The obtained data strongly suggest an interdiffusion or substitution process between the Co-rich LCO layer and the Ga-doped LLZO substrate, exchanging Co and Ga. The fact, that Co^{3+} and Ga^{3+} have the same charge and similar ionic radii (Co^{3+}: 61 (high-spin) pm; Ga^{3+}: 62 pm)[101] further supports the hypothesis of Co/Ga exchange. Furthermore, since Co^{3+} replaces Ga^{3+}, which occupies Li-sites in the garnet[102], considerable mobility and therefore propagation of Co^{3+} in LLZO appears reasonable.
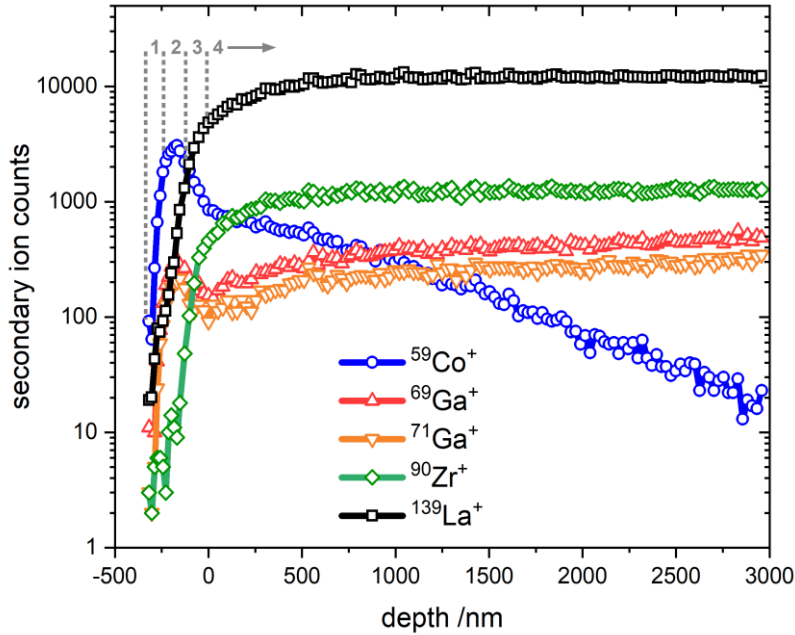
Figure 27: SIMS depth-profiles of positive secondary ions of Co, Ga, Zr and La. The LCO|LLZO sample was annealed at 650 °C for 24 h under air.

Three exemplary normalized Co-profiles of samples annealed at different temperatures (600, 650 and 700 °C, respectively) are shown in Figure 28. Diffusion coefficients of Co (insets in Figure 28) were estimated by fitting the bulk part ("region (4)") of the profiles to a solution of Fick's law of diffusion[103]. The obtained values (up to $1.1 \cdot 10^{-13}$ cm^2/s) are several orders of magnitude higher than reported diffusion coefficients of other transition metals in garnets[104]. Given these unexpectedly high values and the fact, that effects like preferential sputtering and surface roughness likely influence the Co-concentration profiles obtained herein, the diffusion coefficients can merely be considered as upper limits of Co-diffusivity.
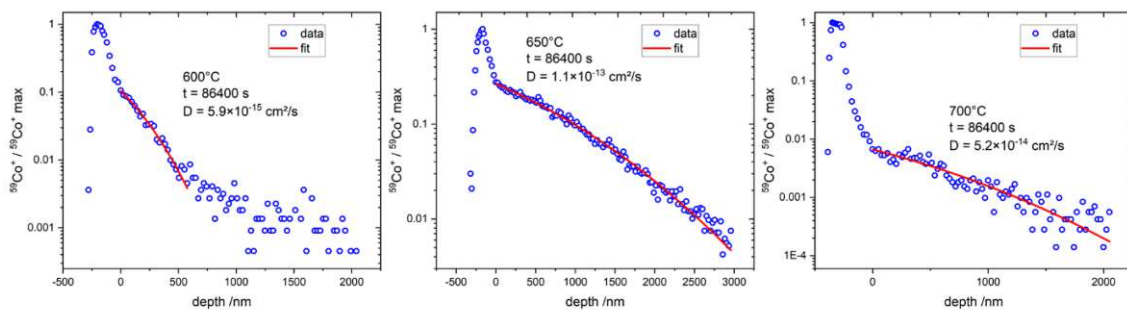
Figure 28: Normalized Co-concentration profiles of samples annealed at 600, 650 respectively 700 °C for 24 hours. Regions used for fitting of regime 4 (described in the text) to solutions of Fick´s law of diffusion are indicated as red lines.

A further set of samples was investigated with smoother surfaces, and after annealing for 48 hours at 600-675°C. The respective profiles parts are shown in Figure 29a. Here, only the bulk regions (regime 4) were considered and the profiles were normalized to the highest Co-concentration within the respective region. All samples show very similar profiles and surprisingly, the data sets of two samples with identical heat treatments (600 °C for 24 h) show more difference than data sets at different temperatures, suggesting either (i): Co-diffusion kinetics are barely dependent on temperature, or more likely (ii): the Co-concentration profiles do not reflect actual diffusion processes. The latter option appears even more likely when considering Figure 29b. Here, the estimated diffusion coefficients of the profiles in Figure 29a are plotted against the inverse annealing temperature (Arrhenius plot) to estimate the activation energy of a possibly thermally activated process.

The activation energy, calculated by linear fitting of the Arrhenius plot ($D \propto \exp(-\frac{E_a}{kT})$), is almost 0 eV, which is unreasonably low compared to activation energy values of other transition metals in garnets[104]. We thus conclude, that the Co-concentration profiles obtained herein cannot be attributed to mere diffusion but rather are products of superposition of various possible effects, as discussed earlier. Again, the extracted values may only serve as an upper boundary for the interdiffusion coefficient and further investigations are necessary.
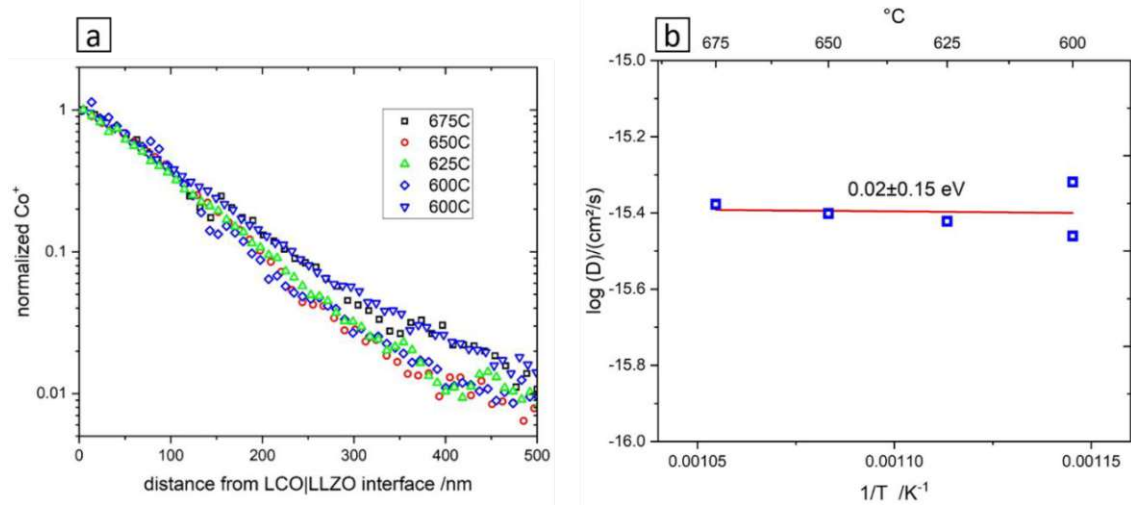
Figure 29: The Co-concentration profiles of different samples are shown in (a). Estimated diffusion coefficients of the respective profiles are compared in an Arrhenius-plot in (b). Data suggest that diffusion during annealing only plays a minor role for the measured profiles.

5.5 Conclusions

We found that significant amounts Co diffuse from LCO thin films into single crystalline LLZO at temperatures as low as 600 °C within 24 hours. The data suggest, that predominantly an exchange between Co and the Ga-dopant occurs, with Co profiles reaching ~1-3 μm into the bulk LLZO. However, based on the similarity of the profiles found after different annealing temperatures, we do not expect them to reflect true interdiffusion profiles that were only generated during the annealing. Rather they are subject to other broadening effects, most probably caused by sample roughness.

6 Designing, manufacturing and optimization of a reactive-gas radio-frequency sputtering device

The following chapter, being more of technical than academic nature, is focused on the sputtering device, which was constructed during the first year of this work. Despite the fact, that most results presented in this thesis (everything except Ch. 5), did not involve the sputtering device at all, a brief description of the sputtering device (including its manufacturing, optimization and operation) is justifiable, if only because of the extensive expenditure of time. The purpose, this chapter serves, is two-fold: (1): to give the reader an impression of the laborious process of producing a fully operational sputtering station and (2): to document technical details about the device, primarily for the sake of (future) co-workers within the working group. At this point, the significant contributions of my co-workers, (i.e. T. Huber and A. Bumberger), must be given credit. A detailed description of the standard parts employed here, as well as rigorous reports on manual manufacturing of custom parts, does not seem reasonable for a doctoral thesis, and is therefore omitted. Since detailed explanation of the physical fundamentals of sputtering processes would be far beyond the scope of this chapter, the reader is referred to parts of the vast literature about this subject [105–108].

6.1 Basic device structure

A schematic overview of the sputter device is shown in Figure 30. The vacuum chamber is the core of the device, serving the purpose to establish and maintain atmospheres required for sputtering processes. The chamber is mainly constructed with standard vacuum parts, made from stainless steel with conflate flanges (CF) as connections between the elements. For the sake of better access to the inside of the chamber, a cylindrical glass recipient (outer diameter 170 mm, 9 mm thick glass, and 200 mm tall) is used as a spacer between the basis and the top of the vacuum chamber. Since glass cannot be joined with CF flanges, the two interfaces between the recipient and the steel parts are connected via quick release ISO-KF

flanges, using elastomeric O-rings of appropriate dimensions. This design offers two major benefits: The inside of the chamber remains visible during operation and the inside of the chamber is easily accessible when the recipient is removed. This is especially convenient for construction and repair measures inside the chamber, which would hardly be possible with a more enclosed design. Despite the fact, that KF flanges are more prone to leakage, the sputtering chamber shows acceptable tightness and base pressures of less than 10^{-4} mbar are achievable.

The chamber pressure is monitored via two pressure cells (Oerlikon Leybold Vacuum, PTR 90 and Leybold, Ceravac CTR 100 N) to ensure reliable measurements over a broad pressure range (10^{-6}-10^3 mbar). The turbo molecular pump (referred to as "TMP", Leybold Turbovac 250iX) with a max speed of 72000 revolutions per minute, is connected to the bottom of the chamber via a manual gate valve (VAT, 11.1 HV gate valve). Alternatively, the chamber can be pumped via a bypass, which directly connects the chamber to the rotary vane pump, which also serves as a backing pump for the TMP.

The top flange mainly serves the purpose of holding the sputter gun (Gencoa, SW50-3G(A)-WMF) in place at an adjustable distance to the sample. Further, a mechanical feedthrough is employed to enable a manual shutter, which is used to cover the target during pre-sputtering procedures. Another small flange can be used to attach a pyrometer to the top, which can then be easily tuned, looking through a small window in the top flange. A pyrometer is necessary to correlate the temperature of the heater (as measured via a type K thermocouple) and the sample surface temperature. The sputter gun is connected to the RF-power supply unit (Seren, R301 RF Power supply) and an external water cooling cycle. Gases (i.e. Ar, O_2 and N_2) are injected into the chamber directly through the sputtering gun. The inlet is connected to the permanent gas piping via flexible, stainless steel tubes, which allow free movement of the top flange. The permanent piping leads through two mass flow controllers (referred to as "MFC", Tylan, FC-260 and Tylan, FC-2900M) with maximum flow rates of 50 sccm, respectively 10 sccm. With two different MFCs, one for Ar and one for O_2 or N_2, a broad range of gas mixtures (Ar/O_2 or Ar/N_2) can be generated. O_2 and N_2 serve as active reagents in reactive sputtering processes, which are common in the synthesis of compounds containing oxygen and/or nitrogen atoms[109–111].

The sample holder unit, which is permanently fixed inside the chamber also serves as a sample heater. The temperature of the resistive heater is monitored via a thermocouple (type K) and adjusted manually by control of the DC power supply (Voltcraft, PPS-16005). Electric wiring is fed through a special flange at the side of the chamber. Since the thermocouple can only provide temperature information from inside the heater, the actual sample surface temperature may differ significantly. Therefore, a laborious calibration procedure was carried out using a pyrometer to check the actual surface temperature. The design and fabrication of the sample holder unit was intricate and cumbersome. After many adaptations, however, good and reliable sample temperature control was achieved. In the following section, technical details about the sample heater are shown.
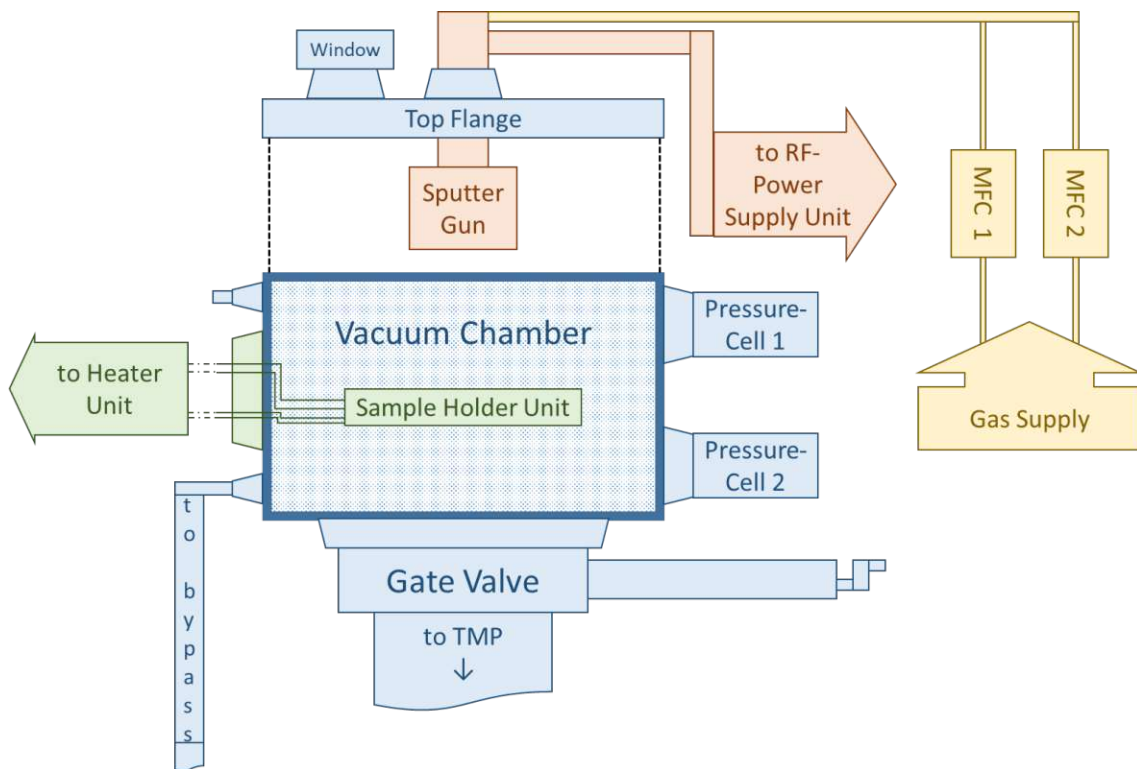
Figure 30: Schematic overview of the constructed sputtering device, including the vacuum management (blue elements), sputter gun (red elements), gas control (yellow elements) and the heated sample holder (green elements).

6.2 Technical details

The sample holder presented here (s. Figure 31), is the latest version from a series of resistive heating stages. Since the chamber is under very low pressure during operation ($\sim 10^{-2}$ mbar) heat is primarily transferred via radiation. This poses a challenge for heater design, since it is not trivial to provide sufficient heat transfer towards the sample while minimizing undesired heat transfer to the surrounding parts.
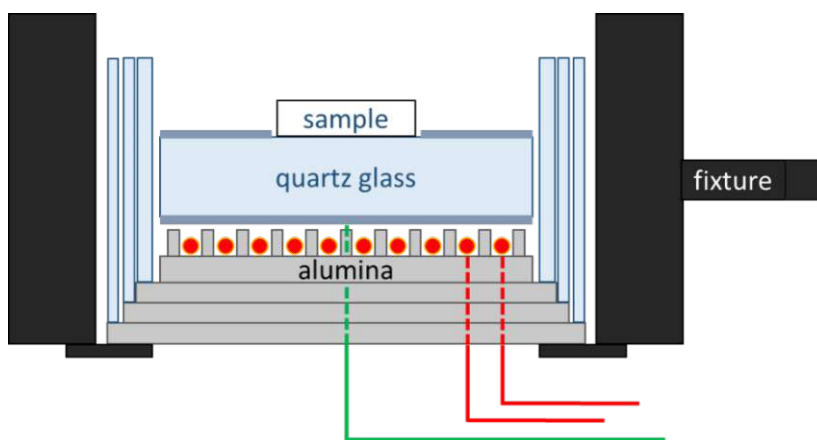
Figure 31: Schematic of the sample holder. A type K thermocouple (green lines) is employed to measure the local temperature inside the heater. Heat is generated resistively through Pt wires (red lines) by a DC power source. Atop the heating wires, a thin piece of quartz glass separates the sample from the heat source while providing optimal heat transfer towards the sample. Thermal shielding towards the bottom is ensured by multiple corundum plates stacked on top of each other.

The heating wires are laid into a special corundum piece (s. Figure 32), which provides mechanical stability. The piece was manufactured by machining of green alumina and subsequent sintering at 1250 °C. Electric wiring is fed through holes the bottom of the corundum piece. Since radiation is the main mechanism for heat transfer in vacuum environments, the heat generated in the Pt wire has to be directed towards the sample via radiation. For this purpose, a thin piece of quartz glass is laid on top of the wire as a separator, since quartz glass offers high transparency for infrared radiation. However, the high transparency of the quartz glass slab posed a problem, since radiation could pass

through in all directions. As a result, most heat radiation dissipated into the sputtering chamber, leaving the sample with insufficient heating power. This was improved by coating the back surface of the slab (s. Figure 33). Herein, the bottom surface of the slab was fully covered with lanthanum strontium ferrite while the top surface was left blank. With this improvement, the heat radiation was significantly channeled towards the sample, providing adequate heating power and sample surface temperatures, as a result. All wires lead from the heating stage were encapsulated with pieces of corundum pipes to ensure electric isolation while retaining thermal stability.
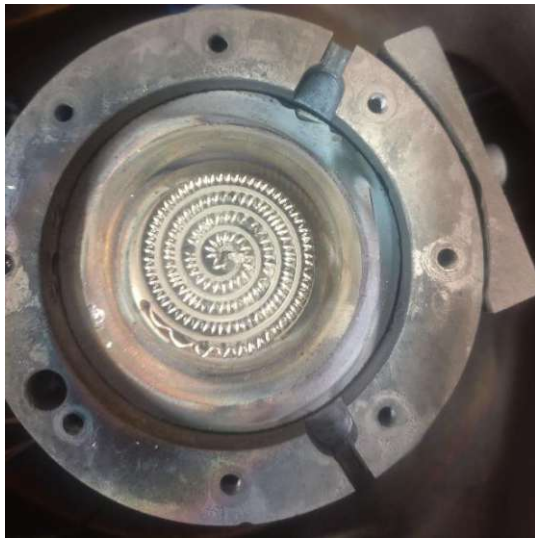
Figure 32: Detail of the heating stage, showing the Pt heating wire laid into the corundum piece. A type K thermocouple is fed through a hole in the middle.
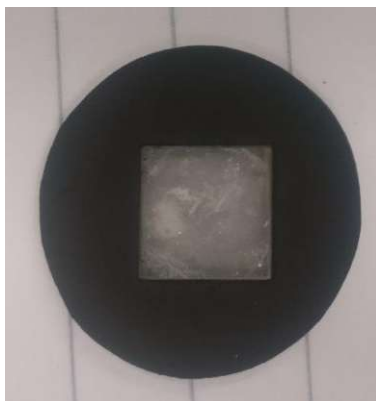
Figure 33: Quartz glass slab, acting as a mechanical separator and heat radiator. At the sample position, the original glass surface is visible, whereas the surroundings are covered with various oxides.

Electric wiring (including heating and thermocouples) from inside the chamber is fed through a special flange at the side of the chamber. The flange was manufactured by embedding the electric elements into high-temperature 2-component epoxy resin (Loctite, EA 9497). For this procedure, a 3D-printed, polylactic acid (PLA) place holder was used to keep all components at the desired positions. Despite the inability of 3D-printed PLA to provide gas-tight sealing, the flange has sufficient tightness, since the entire PLA surface was embedded in the epoxy resin.
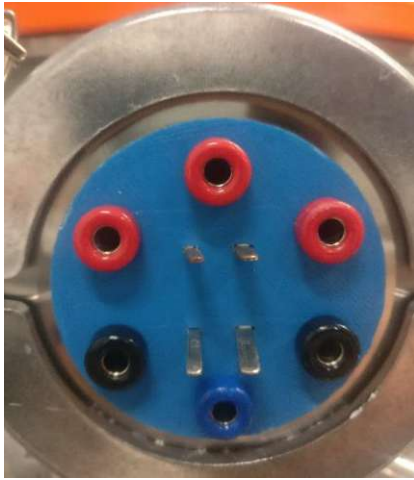
Figure 34: Electric feed through of various kinds, including thermocouples type K (middle, bottom) and type S (middle, top).

6.3 Operational parameters

The operation and maintenance of the sputtering presented herein involves numerous tasks and many work hours. Furthermore, the optimization of sputtering parameters (i.e. substrate temperature, chamber pressure, gas composition, target-substrate distance, etc.) for various materials, such as $LiCoO_2$ (LCO), $LiMn_2O_4$ (LMO) or $SrRuO_3$ (SRO), is laborious and was carried out in large parts by my co-worker, A. Bumberger and various students at the time (Nicole Rosza, Florian Kubik, Matthias Kogler, Claudia Steinbach) who are given due credit for their contributions.

In the following, some exemplary sputtering parameters are shown, which have been optimized for best thin film quality (i.e. crystallinity, stoichiometry, surface smoothness, phase purity). Detailed description of the qualitative and quantitative analysis of the materials, is omitted in regard of the scope of this chapter.

Table 3: Typical sputtering parameters of various materials.

Material	Gas composition	Pressure (mbar)	RF-Power (W)	$T_{Substrate}$ (°C)	$T_{Thermocouple}$ (°C)	Heating Power (W)
LCO	75% Ar 25 % O_2	$2.5 \cdot 10^{-2}$	60	500	667-688	24
LMO	75% Ar 25 % O_2	$2.5 \cdot 10^{-2}$	60	550	738-740	31
SRO	75% Ar 25 % O_2	$2.5 \cdot 10^{-2}$	60	650	859-888	48

6.4 Picture gallery

In this section, selected photographs of the sputtering device are shown (s. Figure 35-Figure 45), providing more technical details and a more direct view of the apparatus.
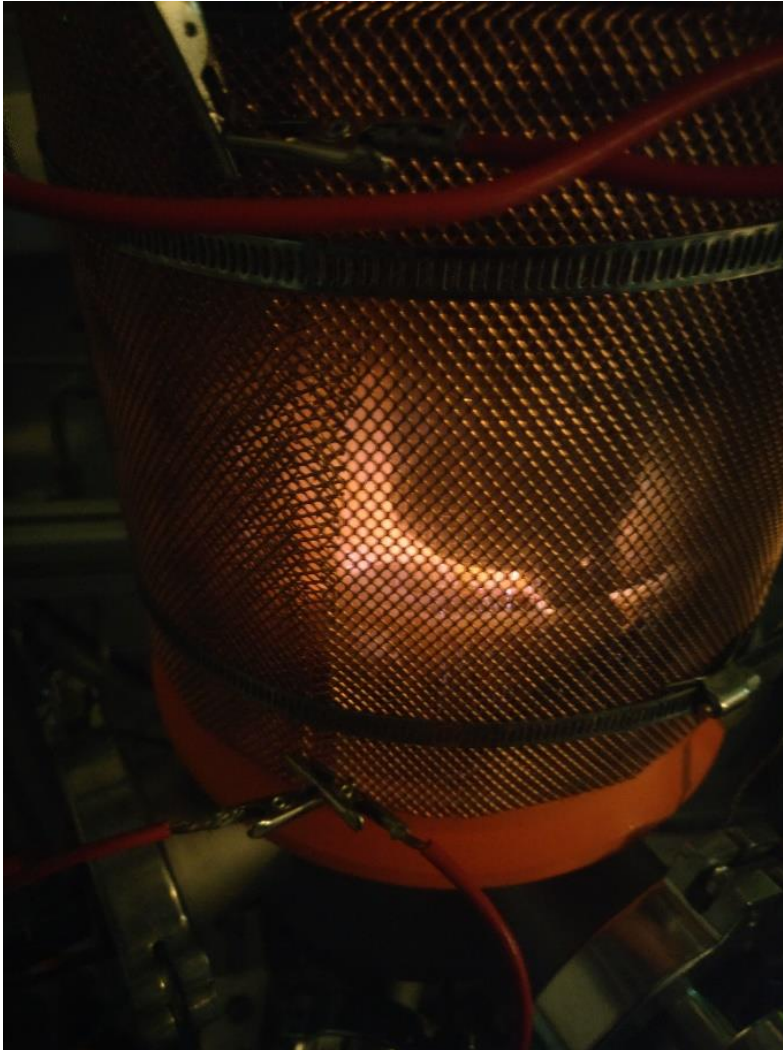
Figure 35: Sputter chamber, glowing from the inside as a result of heating. The electric shielding, employing a copper mesh around the recipient and various clamps, to ensure complete electric shielding of the entire chamber, is of great importance for ignition and stabilization of a well-defined sputtering plasma.

Figure 36: Glass recipient, surrounded by a polymer safety shield and a copper mesh for electric shielding.
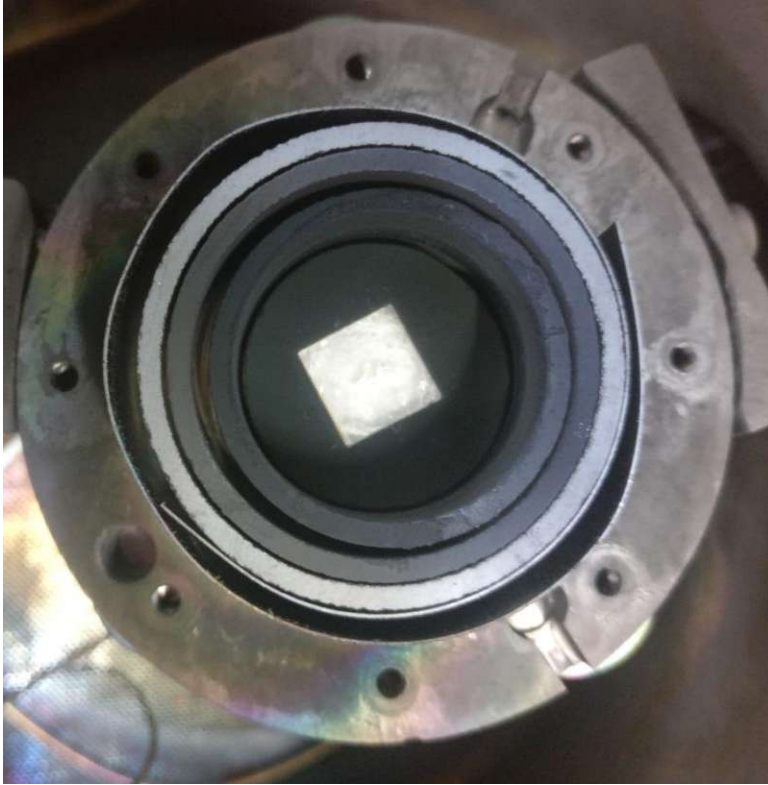
Figure 37: Detail of the fully assembled sample heating stage.

Figure 38: Vacuum backline, showing the TMP and the rotary vane pump, connected by a T-piece. By opening of a bypass valve (outside of picture) the chamber can be evacuated by the backing pump directly, without passing the TMP. This minimizes the risk of particles falling into the TMP when evacuating at atmospheric pressure.
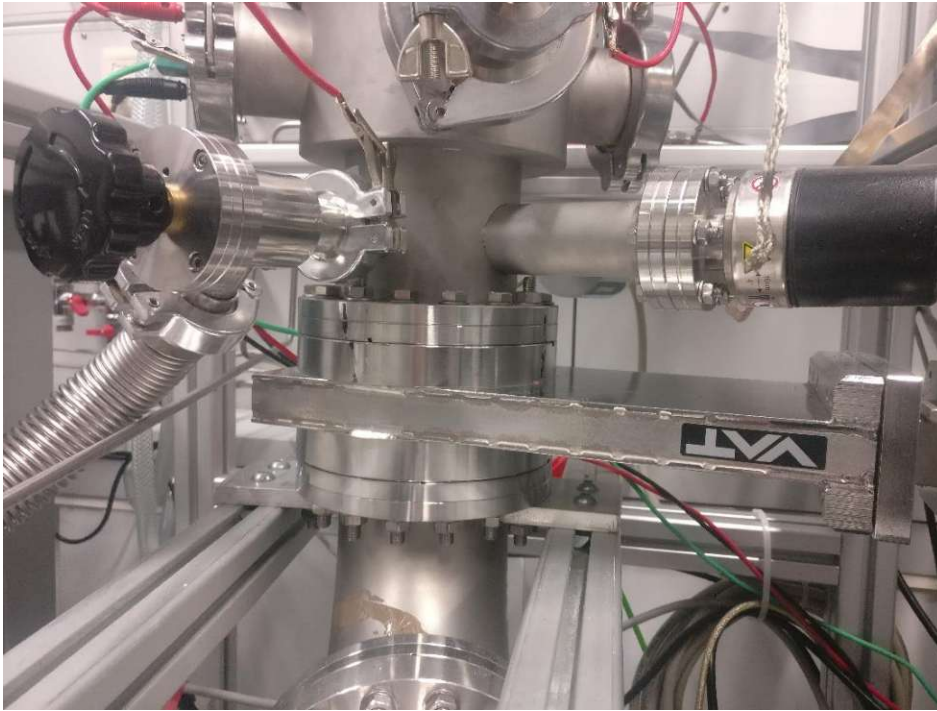
Figure 39: Bypass valve (left) and gate valve (bottom) and a pressure sensor (right), located at the bottom of the vacuum chamber.

Figure 40: Top of the shaft of the sputter gun, fed through the top flange. Clear polymer tubing for water cooling, stainless steel gas tubing and the electric connection to the RF-Power supply (brown cable) are visible.
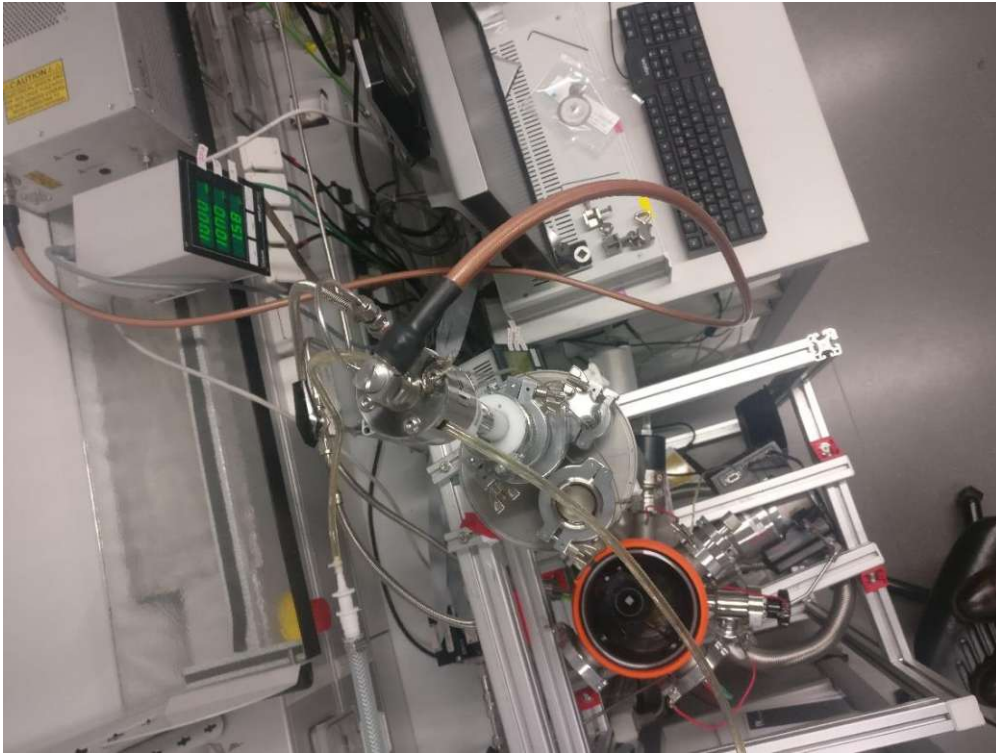
Figure 41: Top view of the setup, showing the top flange, the sample chamber, framing and the control station.

Figure 42: Detail of the top flange, showing a window, the gun feed through as well as the mechanical feed through for turning the shutter inside.

Figure 43: Top flange and sputter gun with opened shutter.

Figure 44: Top view of the sample chamber.
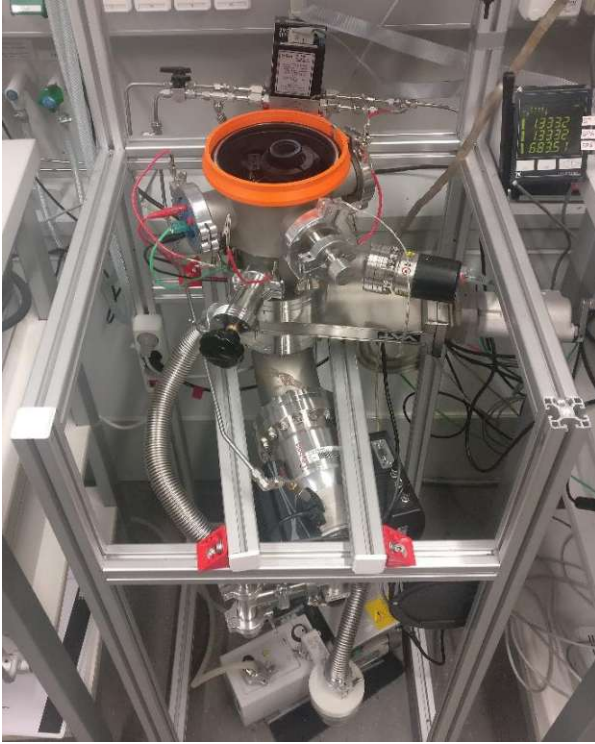
Figure 45: Side view of the sample chamber with MFCs in the back and display unit for the pressure sensors.

Summary

In this work, several new insights into the electrochemical stability of Li ion conducting LLZO and LLTO solid electrolytes were gained. New experimental and theoretical approaches and results were presented.

The electrochemical stability window and the decomposition mechanisms of LLTO were investigated by a combination of electrochemical (EIS and DC techniques) and analytical (LA-ICP-MS) experiments. Above a voltage of about 2.4-2.5 V between two ion blocking electrodes a coloration front starts moving from the reduction side (cathode) towards the anode. This coloration is caused by a slight overlithiation (< 10^{-4} p.f.u.), associated with Ti^{3+} formation taking place at a potential of about 1.7-1.8 V vs. lithium metal. The corresponding moderate electronic conductivity in the colored zone may limit the applicability of LLTO as an electrolyte, but is not caused by an irreversible decomposition reaction. The rise of electronic conductivity in LLTO as a consequence reduction was investigated quantitatively by incrementally reducing LLTO using an external Li supply and subsequent EIS analysis. It was found, that the electrolytic domain boundary (electronic transference number of 0.01) is already reached for a Ti^{3+} fraction in $Li_{0.29+\delta}La_{0.57}TiO_3$ as low as $1.7 \cdot 10^{-8}$, corresponding to a voltage vs. Li of 2.05 V. The corresponding Li excess, however, also includes a filling of electron traps in the band gap. Those can be deduced from the lithiation dependent electronic conductivity measurements and a value of $\delta_{trap} = 7 \cdot 10^{-4}$ is found. Only after filling these traps states, significant amounts of Ti^{4+} are reduced to Ti^{3+}. Furthermore, an improved defect chemical model was developed for the Li insertion reaction, which includes a concentration dependent defect interaction term (i.e. activities). This model can describe the degree of lithiation as a function of the Li chemical potential, i.e. voltage vs. Li metal and yields the corresponding standard Gibbs free energy of the reaction with respect to Li metal, $\Delta_R G^{\emptyset}_{red}$ = -153 kJ/mol. The electronic conductivity of LLTO increases linearly with increasing δ up to ca. $\delta = 3 \cdot 10^{-3}$ and an electron mobility of 0.11 cm^2/Vs can be derived. For stronger lithiation, defect interaction reduces the electron mobility and thus also the increase of electronic conductivity with δ.

The electrochemical stability of LLZO was investigated in two ways: First, using a combination of analytical techniques (XRD, STEM-EELS, SIMS), the effect of electric field stress on the structural and chemical properties of LLZO was elucidated. In contrast to expectations based on literature, results from micro-focused synchrotron XRD experiments (both in-situ and ex-situ) do not indicate formation of any crystalline decomposition products due to electric field stress. However, the crystallinity of the pristine LLZO does decrease upon field stress. From general observations (gas bubble formation) and thermodynamic data, a decomposition reaction involving oxygen evolution seems reasonable. Indeed, results from both STEM-EELS and SIMS suggest oxygen loss caused by the electric field stress. The degree of oxygen depletion clearly increases when approaching the surface. Furthermore, the results suggest no substantial change of La or Zr stoichiometry. Secondly, the stability of Ga-doped LLZO in contact with LCO was investigated by SIMS. It was shown, that Co exchanges with Ga at temperatures above 600 °C. As a consequence, significant amounts of Co were found as deep as 1000 nm inside the LLZO bulk after an annealing period of 24 hours at 600 °C. It is quite probable, that the incorporated Co is detrimental for the electrochemical properties of LLZO. For an exact quantification of the exchange and diffusion rates of Co in(to) LLZO, further studies with smooth LLZO samples are required. For the purpose of thin-film deposition of LCO on LLZO, a sputtering device was designed and put into operation. Technical details of novel components were shown, possibly contributing to the functionality of specialized sputtering devices with similar demands.

References

(1) Zhu, Y.; He, X.; Mo, Y. Origin of Outstanding Stability in the Lithium Solid Electrolyte Materials: Insights from Thermodynamic Analyses Based on First-Principles Calculations. *ACS Appl. Mater. Interfaces* **2015**, *7* (42), 23685–23693. https://doi.org/10.1021/acsami.5b07517.

(2) Xu, H.; Yu, Y.; Wang, Z.; Shao, G. First Principle Material Genome Approach for All Solid-State Batteries. **2019**, 18.

(3) Rettenwander, D.; Redhammer, G.; Preishuber-Pflügl, F.; Cheng, L.; Miara, L.; Wagner, R.; Welzl, A.; Suard, E.; Doeff, M. M.; Wilkening, M.; Fleig, J.; Amthauer, G. Structural and Electrochemical Consequences of Al and Ga Cosubstitution in $Li_7La_3Zr_2O_{12}$ Solid Electrolytes. *Chem. Mater.* **2016**, *28* (7), 2384–2392. https://doi.org/10.1021/acs.chemmater.6b00579.

(4) Wolfenstine, J.; Ratchford, J.; Rangasamy, E.; Sakamoto, J.; Allen, J. L. Synthesis and High Li-Ion Conductivity of Ga-Stabilized Cubic $Li_7La_3Zr_2O_{12}$. *Mater. Chem. Phys.* **2012**, *134* (2–3), 571–575. https://doi.org/10.1016/j.matchemphys.2012.03.054.

(5) Posch, P.; Lunghammer, S.; Berendts, S.; Ganschow, S.; Redhammer, G. J.; Wilkening, A.; Lerch, M.; Gadermaier, B.; Rettenwander, D.; Wilkening, H. M. R. Ion Dynamics in Al-Stabilized $Li_7La_3Zr_2O_{12}$ Single Crystals – Macroscopic Transport and the Elementary Steps of Ion Hopping. *Energy Storage Mater.* **2020**, *24*, 220–228. https://doi.org/10.1016/j.ensm.2019.08.017.

(6) Geiger, C. A.; Alekseev, E.; Lazic, B.; Fisch, M.; Armbruster, T.; Langner, R.; Fechtelkord, M.; Kim, N.; Pettke, T.; Weppner, W. Crystal Chemistry and Stability of "$Li_7La_3Zr_2O_{12}$" Garnet: A Fast Lithium-Ion Conductor. *Inorg. Chem.* **2011**, *50* (3), 1089–1097. https://doi.org/10.1021/ic101914e.

(7) Rettenwander, D.; Geiger, C. A.; Amthauer, G. Synthesis and Crystal Chemistry of the Fast Li-Ion Conductor $Li_7La_3Zr_2O_{12}$ Doped with Fe. *Inorg. Chem.* **2013**, *52* (14), 8005–8009. https://doi.org/10.1021/ic400589u.

(8) Allen, J. L.; Wolfenstine, J.; Rangasamy, E.; Sakamoto, J. Effect of Substitution (Ta, Al, Ga) on the Conductivity of $Li_7La_3Zr_2O_{12}$. *J. Power Sources* **2012**, *206*, 315–319. https://doi.org/10.1016/j.jpowsour.2012.01.131.

(9) Wolfenstine, J.; Sakamoto, J.; Allen, J. L. Electron Microscopy Characterization of Hot-Pressed Al Substituted $Li_7La_3Zr_2O_{12}$. *J. Mater. Sci.* **2012**, *47* (10), 4428–4431. https://doi.org/10.1007/s10853-012-6300-y.

(10) Buschmann, H.; Berendts, S.; Mogwitz, B.; Janek, J. Lithium Metal Electrode Kinetics and Ionic Conductivity of the Solid Lithium Ion Conductors "$Li_7La_3Zr_2O_{12}$" and $Li_{7-x}La_3Zr_{2-x}Ta_xO_{12}$ with Garnet-Type Structure. *J. Power Sources* **2012**, *206*, 236–244. https://doi.org/10.1016/j.jpowsour.2012.01.094.

(11) Li, Y.; Wang, C.-A.; Xie, H.; Cheng, J.; Goodenough, J. B. High Lithium Ion Conduction in Garnet-Type $Li_6La_3ZrTaO_{12}$. *Electrochem. Commun.* **2011**, *13* (12), 1289–1292. https://doi.org/10.1016/j.elecom.2011.07.008.

(12) Ohta, S.; Kobayashi, T.; Asaoka, T. High Lithium Ionic Conductivity in the Garnet-Type Oxide $Li_{7-x}La_3(Zr_{2-x}, Nb_x)O_{12}$ (X=0–2). *J. Power Sources* **2011**, *196* (6), 3342–3345. https://doi.org/10.1016/j.jpowsour.2010.11.089.

(13) Rangasamy, E.; Wolfenstine, J.; Sakamoto, J. The Role of Al and Li Concentration on the Formation of Cubic Garnet Solid Electrolyte of Nominal Composition $Li_7La_3Zr_2O_{12}$. *Solid State Ion.* **2012**, *206*, 28–32. https://doi.org/10.1016/j.ssi.2011.10.022.

(14) Krauskopf, T.; Dippel, R.; Hartmann, H.; Peppler, K.; Mogwitz, B.; Richter, F. H.; Zeier, W. G.; Janek, J. Lithium-Metal Growth Kinetics on LLZO Garnet-Type Solid Electrolytes. *Joule* **2019**, *3* (8), 2030–2049. https://doi.org/10.1016/j.joule.2019.06.013.

(15) Connell, J. G.; Fuchs, T.; Hartmann, H.; Krauskopf, T.; Zhu, Y.; Sann, J.; Garcia-Mendez, R.; Sakamoto, J.; Tepavcevic, S.; Janek, J. Kinetic versus Thermodynamic Stability of LLZO in Contact with Lithium Metal. *Chem. Mater.* **2020**, *32* (23), 10207–10215. https://doi.org/10.1021/acs.chemmater.0c03869.

(16) Ma, C.; Cheng, Y.; Yin, K.; Luo, J.; Sharafi, A.; Sakamoto, J.; Li, J.; More, K. L.; Dudney, N. J.; Chi, M. Interfacial Stability of Li Metal–Solid Electrolyte Elucidated via in Situ Electron Microscopy. *Nano Lett.* **2016**, *16* (11), 7030–7036. https://doi.org/10.1021/acs.nanolett.6b03223.

(17) Su, J.; Huang, X.; Song, Z.; Xiu, T.; Badding, M. E.; Jin, J.; Wen, Z. Overcoming the Abnormal Grain Growth in Ga-Doped $Li_7La_3Zr_2O_{12}$ to Enhance the Electrochemical Stability against Li Metal. *Ceram. Int.* **2019**, *45* (12), 14991–14996. https://doi.org/10.1016/j.ceramint.2019.04.236.

(18) Li, J.; Wang, R. Recent Advances in the Interfacial Stability, Design and in Situ Characterization of Garnet-Type $Li_7La_3Zr_2O_{12}$ Solid-State Electrolytes Based Lithium Metal Batteries. *Ceram. Int.* **2021**, *47* (10), 13280–13290. https://doi.org/10.1016/j.ceramint.2021.02.034.

(19) Rettenwander, D.; Wagner, R.; Reyer, A.; Bonta, M.; Cheng, L.; Doeff, M. M.; Limbeck, A.; Wilkening, M.; Amthauer, G. Interface Instability of Fe-Stabilized $Li_7La_3Zr_2O_{12}$ versus Li Metal. *J. Phys. Chem. C* **2018**, *122* (7), 3780–3785. https://doi.org/10.1021/acs.jpcc.7b12387.

(20) Cai, M.; Jin, J.; Xiu, T.; Song, Z.; Badding, M. E.; Wen, Z. In-Situ Constructed Lithium-Salt Lithiophilic Layer Inducing Bi-Functional Interphase for Stable LLZO/Li Interface. *Energy Storage Mater.* **2022**, *47*, 61–69. https://doi.org/10.1016/j.ensm.2022.01.046.

(21) Sharafi, A.; Meyer, H. M.; Nanda, J.; Wolfenstine, J.; Sakamoto, J. Characterizing the Li–$Li_7La_3Zr_2O_{12}$ Interface Stability and Kinetics as a Function of Temperature and Current Density. *J. Power Sources* **2016**, *302*, 135–139. https://doi.org/10.1016/j.jpowsour.2015.10.053.

(22) Han, F.; Zhu, Y.; He, X.; Mo, Y.; Wang, C. Electrochemical Stability of $Li_1 GeP_2S_{12}$ and $Li_7La_3Zr_2O_{12}$ Solid Electrolytes. *Adv. Energy Mater.* **2016**, *6* (8), 1501590. https://doi.org/10.1002/aenm.201501590.

(23) Smetaczek, S.; Pycha, E.; Ring, J.; Siebenhofer, M.; Ganschow, S.; Berendts, S.; Nenning, A.; Kubicek, M.; Rettenwander, D.; Limbeck, A.; Fleig, J. Investigating the Electrochemical Stability of $Li_7La_3Zr_2O_{12}$ Solid Electrolytes Using Field Stress Experiments. *J. Mater. Chem. A* **2021**, *9* (27), 15226–15237. https://doi.org/10.1039/D1TA02983E.

(24) Stramare, S.; Thangadurai, V.; Weppner, W. Lithium Lanthanum Titanates: A Review. *Chem. Mater.* **2003**, *15* (21), 3974–3990. https://doi.org/10.1021/cm0300516.

(25) Qian, D.; Xu, B.; Cho, H.-M.; Hatsukade, T.; Carroll, K. J.; Meng, Y. S. Lithium Lanthanum Titanium Oxides: A Fast Ionic Conductive Coating for Lithium-Ion Battery Cathodes. *Chem Mater* **2012**, 8.

(26) Warburton, R. E.; Kim, J. J.; Patel, S.; Howard, J. D.; Curtiss, L. A.; Wolverton, C.; Buchholz, D. B.; Vaughey, J. T.; Fenter, P.; Fister, T. T.; Greeley, J. Tailoring Interfaces in Solid-State Batteries Using Interfacial Thermochemistry and Band Alignment. *Chem. Mater.* **2021**, *33* (21), 8447–8459. https://doi.org/10.1021/acs.chemmater.1c02803.

(27) Bertrand, M.; Rousselot, S.; Aymé-Perrot, D.; Dollé, M. Compatibility Assessment of Solid Ceramic Electrolytes and Active Materials Based on Thermal Dilatation for the Development of Solid-State Batteries. *Mater. Adv.* **2021**, *2* (9), 2989–2999. https://doi.org/10.1039/D0MA00743A.

(28) Birke, P.; Scharner, S.; Huggins, R. A.; Weppner, W. Electrolytic Stability Limit and Rapid Lithium Insertion in the Fast-Ion-Conducting $Li_{0.29}La_{0.57}TiO_3$ Perovskite-Type Compound. *J. Electrochem. Soc.* **1997**, *144* (6), L167–L169. https://doi.org/10.1149/1.1837713.

(29) Hua, C.; Fang, X.; Wang, Z.; Chen, L. Lithium Storage in Perovskite Lithium Lanthanum Titanate. *Electrochem. Commun.* **2013**, *32*, 5–8. https://doi.org/10.1016/j.elecom.2013.03.038.

(30) Zhang, L.; Zhang, X.; Tian, G.; Zhang, Q.; Knapp, M.; Ehrenberg, H.; Chen, G.; Shen, Z.; Yang, G.; Gu, L.; Du, F. Lithium Lanthanum Titanate Perovskite as an Anode for Lithium Ion Batteries. *Nat. Commun.* **2020**, *11* (1), 3490. https://doi.org/10.1038/s41467-020-17233-1.

(31) Wenzel, S.; Leichtweiss, T.; Krüger, D.; Sann, J.; Janek, J. Interphase Formation on Lithium Solid Electrolytes—An in Situ Approach to Study Interfacial Reactions by Photoelectron Spectroscopy. *Solid State Ion.* **2015**, *278*, 98–105. https://doi.org/10.1016/j.ssi.2015.06.001.

(32) Ho, C.; Raistrick, I. D.; Huggins, R. A. Application of A-C Techniques to the Study of Lithium Diffusion in Tungsten Trioxide Thin Films. *J. Electrochem. Soc.* **1980**, *127* (2), 343–350. https://doi.org/10.1149/1.2129668.

(33) Park, K.; Yu, B.-C.; Jung, J.-W.; Li, Y.; Zhou, W.; Gao, H.; Son, S.; Goodenough, J. B. Electrochemical Nature of the Cathode Interface for a Solid-State Lithium-Ion Battery: Interface between $LiCoO_2$ and Garnet-$Li_7La_3Zr_2O_{12}$. *Chem. Mater.* **2016**, *28* (21), 8051–8059. https://doi.org/10.1021/acs.chemmater.6b03870.

(34) Zarabian, M.; Bartolini, M.; Pereira-Almao, P.; Thangadurai, V. X-Ray Photoelectron Spectroscopy and AC Impedance Spectroscopy Studies of Li-La-Zr-O Solid Electrolyte

Thin Film/$LiCoO_2$ Cathode Interface for All-Solid-State Li Batteries. *J. Electrochem. Soc.* **2017**, *164* (6), A1133–A1139. https://doi.org/10.1149/2.0621706jes.

(35) Kim, K. H.; Iriyama, Y.; Yamamoto, K.; Kumazaki, S.; Asaka, T.; Tanabe, K.; Fisher, C. A. J.; Hirayama, T.; Murugan, R.; Ogumi, Z. Characterization of the Interface between $LiCoO_2$ and $Li_7La_3Zr_2O_{12}$ in an All-Solid-State Rechargeable Lithium Battery. *J. Power Sources* **2011**, *196* (2), 764–767. https://doi.org/10.1016/j.jpowsour.2010.07.073.

(36) Inaguma, Y.; Liquan, C.; Itoh, M.; Nakamura, T.; Uchida, T.; Ikuta, H.; Wakihara, M. High Ionic Conductivity in Lithium Lanthanum Titanate. *Solid State Commun.* **1993**, *86* (10), 689–693. https://doi.org/10.1016/0038-1098(93)90841-A.

(37) Bohnke, O. Mechanism of Ionic Conduction and Electrochemical Intercalation of Lithium into the Perovskite Lanthanum Lithium Titanate. *Solid State Ion.* **1996**, *91* (1–2), 21–31. https://doi.org/10.1016/S0167-2738(96)00434-1.

(38) Inaguma, Y. Lithium Ion Conductivity in the Perovskite-Type $LiTaO_3$-$SrTiO_3$ Solid Solution. *Solid State Ion.* **1995**, *79*, 91–97. https://doi.org/10.1016/0167-2738(95)00036-6.

(39) Shan, Y. J.; Chen, L.; Inaguma, Y.; Itoh, M.; Nakamura, T. Oxide Cathode with Perovskite Structure for Rechargeable Lithium Batteries. *J. Power Sources* **1995**, *54* (2), 397–402. https://doi.org/10.1016/0378-7753(94)02110-O.

(40) Lee, J.-S.; Yoo, K. S.; Kim, T. S.; Jung, H. J. Evaluation of the AC Response of Li-Electrolytic Perovskites $Li_{0.5}(Ln_xLa_{0.5-x})TiO_3$ (Ln = Nd, Gd) in Conjunction with Their Crystallographic and Microstructural Characteristics. *Solid State Ion.* **1997**, 12.

(41) Emery, J.; Buzare, J. Y.; Bohnke, O.; Fourquet, J. L. Lithium-7 NMR and Ionic Conductivity Studies of Lanthanum Lithium Titanate Electrolytes. *Solid State Ion.* **1997**, *99* (1–2), 41–51. https://doi.org/10.1016/S0167-2738(97)00202-6.

(42) Harada, Y. Order–Disorder of the A-Site Ions and Lithium Ion Conductivity in the Perovskite Solid Solution $La_{0.67-x}Li_{3x}TiO_3$ (x=0.11). *Solid State Ion.* **1999**, *121* (1–4), 245–251. https://doi.org/10.1016/S0167-2738(99)00043-0.

(43) Oguni, M.; Inaguma, Y.; Itoh, M.; Nakamura, T. Calorimetric and Electrical Studies on the Positional Disorder of Lithium Ions in Lithium Lanthanum Titanate. *Solid State Commun.* **1994**, *91* (8), 627–630. https://doi.org/10.1016/0038-1098(94)90560-6.

(44) Harada, Y.; Ishigaki, T.; Kawai, H.; Kuwano, J. Lithium Ion Conductivity of Polycrystalline Perovskite $La_{0.67-x}Li_{3x}TiO_3$ with Ordered and Disordered Arrangements of the A-Site Ions. *Solid State Ion.* **1998**, 7.

(45) Hirakoso, Y.; Harada, Y.; Kuwano, J.; Saito, Y.; Ishikawa, Y.; Eguchi, T. Lithium Ion Conduction in the Ordered Ans Disordered Phases of A-Site Deficient Perovskite $La_{0.56}Li_{0.33}TiO_3$. *Key Eng. Mater.* **1999**, *169–170*, 209–212. https://doi.org/10.4028/www.scientific.net/KEM.169-170.209.

(46) Gao, X.; Fisher, C. A. J.; Kimura, T.; Ikuhara, Y. H.; Moriwake, H.; Kuwabara, A.; Oki, H.; Tojigamori, T.; Huang, R.; Ikuhara, Y. Lithium Atom and A-Site Vacancy Distributions in Lanthanum Lithium Titanate. *Chem. Mater.* **2013**, *25* (9), 1607–1614. https://doi.org/10.1021/cm3041357.

(47) Li, Z.; Li, C.; Liu, X.; Cao, L.; Li, P.; Wei, R.; Li, X.; Guo, D.; Huang, K.-W.; Lai, Z. Continuous Electrical Pumping Membrane Process for Seawater Lithium Mining. *Energy Environ. Sci.* **2021**, *14* (5), 3152–3159. https://doi.org/10.1039/D1EE00354B.

(48) Inaguma, Y.; Nakashima, M. A Rechargeable Lithium–Air Battery Using a Lithium Ion-Conducting Lanthanum Lithium Titanate Ceramics as an Electrolyte Separator. *J. Power Sources* **2013**, *228*, 250–255. https://doi.org/10.1016/j.jpowsour.2012.11.098.

(49) Blanc, J.; Staebler, D. L. Electrocoloration in $SrTiO_3$: Vacancy Drift and Oxidation-Reduction of Transition Metals. *Phys. Rev. B* **1971**, *4* (10), 3548–3557. https://doi.org/10.1103/PhysRevB.4.3548.

(50) Waser, R.; Baiatu, T.; Härdtl, K.-H. Dc Electrical Degradation of Perovskite-Type Titanates: II, Single Crystals. *J. Am. Ceram. Soc.* **1990**, *73* (6), 1654–1662. https://doi.org/10.1111/j.1151-2916.1990.tb09810.x.

(51) Rodenbücher, C.; Szot, K.; Wrana, D.; Jany, B. R.; Krok, F.; Korte, C. Localized Electrochemical Redox Reactions in Yttria-Stabilized Zirconia Single Crystals. *J. Phys. Energy* **2020**, *2* (3), 034008. https://doi.org/10.1088/2515-7655/ab6b39.

(52) Yokota, I. On the Theory of Mixed Conduction with Special Reference to Conduction in Silver Sulfide Group Semiconductors. *J. Phys. Soc. Jpn.* **1961**, *16* (11), 2213–2223. https://doi.org/10.1143/JPSJ.16.2213.

(53) Miyatani, S. An Extension of Yokota's Diffusion Theory on Mixed Conduction to Larger Applied Voltages. *J. Phys. Soc. Jpn.* **1981**, *50* (5), 1595–1602. https://doi.org/10.1143/JPSJ.50.1595.

(54) Hebb, M. H. Electrical Conductivity of Silver Sulfide. *J. Chem. Phys.* **1952**, *20* (1), 185–190. https://doi.org/10.1063/1.1700165.

(55) Wagner, C. Galvanische Zellen Mit Festen Elektrolyten Mit Gemischter Stromleitung. *Z. Für Elektrochem. Berichte Bunsenges. Für Phys. Chem.* **1956**, *60* (1), 4–7. https://doi.org/10.1002/bbpc.19560600104.

(56) Wang, M. J.; Wolfenstine, J. B.; Sakamoto, J. Mixed Electronic and Ionic Conduction Properties of Lithium Lanthanum Titanate. *Adv. Funct. Mater.* **2020**, *30* (10), 1909140. https://doi.org/10.1002/adfm.201909140.

(57) Geng, D.; Ding, N.; Hor, T. S. A.; Chien, S. W.; Liu, Z.; Wuu, D.; Sun, X.; Zong, Y. From Lithium-Oxygen to Lithium-Air Batteries: Challenges and Opportunities. *Adv. Energy Mater.* **2016**, *6* (9), 1502164. https://doi.org/10.1002/aenm.201502164.

(58) Siebenhofer, M.; Baiutti, F.; de Dios Sirvent, J.; Huber, T. M.; Viernstein, A.; Smetaczek, S.; Herzig, C.; Liedke, M. O.; Butterling, M.; Wagner, A.; Hirschmann, E.; Limbeck, A.; Tarancon, A.; Fleig, J.; Kubicek, M. Exploring Point Defects and Trap States in Undoped $SrTiO_3$ Single Crystals. *J. Eur. Ceram. Soc.* **2022**, *42* (4), 1510–1521. https://doi.org/10.1016/j.jeurceramsoc.2021.10.010.

(59) Opitz, A. K.; Lutz, A.; Kubicek, M.; Kubel, F.; Hutter, H.; Fleig, J. Investigation of the Oxygen Exchange Mechanism on Pt|yttria Stabilized Zirconia at Intermediate Temperatures: Surface Path versus Bulk Path. *Electrochimica Acta* **2011**, *56* (27), 9727–9740. https://doi.org/10.1016/j.electacta.2011.07.112.

(60) Kubicek, M.; Wachter-Welzl, A.; Rettenwander, D.; Wagner, R.; Berendts, S.; Uecker, R.; Amthauer, G.; Hutter, H.; Fleig, J. Oxygen Vacancies in Fast Lithium-Ion Conducting Garnets. *Chem. Mater.* **2017**, *29* (17), 7189–7196. https://doi.org/10.1021/acs.chemmater.7b01281.

(61) Aguesse, F.; Roddatis, V.; Roqueta, J.; García, P.; Pergolesi, D.; Santiso, J.; Kilner, J. A. Microstructure and Ionic Conductivity of LLTO Thin Films: Influence of Different Substrates and Excess Lithium in the Target. *Solid State Ion.* **2015**, *272*, 1–8. https://doi.org/10.1016/j.ssi.2014.12.005.

(62) Jiang, Z.; Wang, S.; Chen, X.; Yang, W.; Yao, X.; Hu, X.; Han, Q.; Wang, H. Tape-Casting $Li_{0.34}La_{0.56}TiO_3$ Ceramic Electrolyte Films Permit High Energy Density of Lithium-Metal Batteries. *Adv. Mater.* **2020**, *32* (6), 1906221. https://doi.org/10.1002/adma.201906221.

(63) Trong, L. D.; Thao, T. T.; Dinh, N. N. Characterization of the Li-Ionic Conductivity of $La_{2/3-x}Li_{3x}TiO_3$ Ceramics Used for All-Solid-State Batteries. *Solid State Ion.* **2015**, *278*, 228–232. https://doi.org/10.1016/j.ssi.2015.05.027.

(64) Chen, C. Ionic Conductivity, Lithium Insertion and Extraction of Lanthanum Lithium Titanate. *Solid State Ion.* **2001**, *144* (1–2), 51–57. https://doi.org/10.1016/S0167-2738(01)00884-0.

(65) Nakayama, M.; Usui, T.; Uchimoto, Y.; Wakihara, M.; Yamamoto, M. Changes in Electronic Structure upon Lithium Insertion into the A-Site Deficient Perovskite Type Oxides $(Li,La)TiO_3$. *J. Phys. Chem. B* **2005**, *109* (9), 4135–4143. https://doi.org/10.1021/jp046062j.

(66) Hua, C.; Fang, X.; Wang, Z.; Chen, L. Lithium Storage in Perovskite Lithium Lanthanum Titanate. *Electrochem. Commun.* **2013**, *32*, 5–8. https://doi.org/10.1016/j.elecom.2013.03.038.

(67) Dai, K.; Wang, Q.; Xie, Y.; Shui, M.; Shu, J. Disordered Carbon Coating Free $Li_{0.2375}La_{0.5875}TiO_3$: A Superior Perovskite Anode Material for High Power Long-Life Lithium-Ion Batteries. *J. Mater. Sci.* **2022**, *57* (4), 2825–2838. https://doi.org/10.1007/s10853-021-06713-4.

(68) Zhang, L.; Zhang, X.; Tian, G.; Zhang, Q.; Knapp, M.; Ehrenberg, H.; Chen, G.; Shen, Z.; Yang, G.; Gu, L.; Du, F. Lithium Lanthanum Titanate Perovskite as an Anode for Lithium Ion Batteries. *Nat. Commun.* **2020**, *11* (1), 3490. https://doi.org/10.1038/s41467-020-17233-1.

(69) Wang, J.; Wang, M.; Xiao, J.; Dong, J.; Li, Y.; Zhang, L.; Si, J.; Pan, B.; Chen, C.; Chen, C. A Microstructure Engineered Perovskite Super Anode with Li-Storage Life of Exceeding 10,000 Cycles. *Nano Energy* **2022**, *94*, 106972. https://doi.org/10.1016/j.nanoen.2022.106972.

(70) Park, J.; Blumenthal, R. N. Electronic Transport in 8 Mole Percent Y_2O_3 - ZrO_2. *J. Electrochem. Soc.* **1989**, *136* (10), 2867–2876. https://doi.org/10.1149/1.2096302.

(71) Merryweather, A. J.; Jacquet, Q.; Emge, S. P.; Schnedermann, C.; Rao, A.; Grey, C. P. Operando Monitoring of Single-Particle Kinetic State-of-Charge Heterogeneities and

Cracking in High-Rate Li-Ion Anodes. *Nat. Mater.* **2022**, *21* (11), 1306–1313. https://doi.org/10.1038/s41563-022-01324-z.

(72) Ohta, S.; Nomura, T.; Ohta, H.; Koumoto, K. High-Temperature Carrier Transport and Thermoelectric Properties of Heavily La- or Nb-Doped $SrTiO_3$ Single Crystals. *J. Appl. Phys.* **2005**, *97* (3), 034106. https://doi.org/10.1063/1.1847723.

(73) Zinkevich, T.; Schwarz, B.; Braun, P.; Weber, A.; Ehrenberg, H.; Indris, S. Effect of Sintering Temperature on Li Diffusivity in $Li_{0.29}La_{0.57}TiO_3$: Local Hopping and Long-Range Transport. *Solid State Ion.* **2020**, *357*, 115486. https://doi.org/10.1016/j.ssi.2020.115486.

(74) Ibarra, J.; Várez, A.; León, C.; Santamaría, J.; Torres-Martínez, L. M.; Sanz, J. Influence of Composition on the Structure and Conductivity of the Fast Ionic Conductors $La_{2/3-x}Li_{3x}TiO_3$ (0.03≤x≤0.167). *Solid State Ion.* **2000**, *134* (3), 219–228. https://doi.org/10.1016/S0167-2738(00)00761-X.

(75) Moriwake, H.; Gao, X.; Kuwabara, A.; Fisher, C. A. J.; Kimura, T.; Ikuhara, Y. H.; Kohama, K.; Tojigamori, T.; Ikuhara, Y. Domain Boundaries and Their Influence on Li Migration in Solid-State Electrolyte (La,Li)TiO3. *J. Power Sources* **2015**, *276*, 203–207. https://doi.org/10.1016/j.jpowsour.2014.11.139.

(76) Kang, S. D.; Chueh, W. C. Galvanostatic Intermittent Titration Technique Reinvented: Part I. A Critical Review. *J. Electrochem. Soc.* **2021**, *168* (12), 120504. https://doi.org/10.1149/1945-7111/ac3940.

(77) Lai, W.; Haile, S. M. Impedance Spectroscopy as a Tool for Chemical and Electrochemical Analysis of Mixed Conductors: A Case Study of Ceria. *J. Am. Ceram. Soc.* **2005**, *88*, 2979–2997. https://doi.org/10.1111/j.1551-2916.2005.00740.x.

(78) Jamnik, J.; Maier, J. Generalised Equivalent Circuits for Mass and Charge Transport: Chemical Capacitance and Its Implications. *Phys. Chem. Chem. Phys.* **2001**, *3*, 1668–1678. https://doi.org/Doi 10.1039/B100180i.

(79) Dees, D. W.; Rodrigues, M.-T. F.; Kalaga, K.; Trask, S. E.; Shkrob, I. A.; Abraham, D. P.; Jansen, A. N. Apparent Increasing Lithium Diffusion Coefficient with Applied Current in Graphite. *J. Electrochem. Soc.* **2020**, *167* (12), 120528. https://doi.org/10.1149/1945-7111/abaf9f.

(80) Murugan, R.; Thangadurai, V.; Weppner, W. Fast Lithium Ion Conduction in Garnet-Type $Li_7La_3Zr_2O_{12}$. *Angew. Chem. Int. Ed.* **2007**, *46* (41), 7778–7781. https://doi.org/10.1002/anie.200701144.

(81) Li, Y.; Han, J.-T.; Wang, C.-A.; Xie, H.; Goodenough, J. B. Optimizing Li+ Conductivity in a Garnet Framework. *J. Mater. Chem.* **2012**, *22* (30), 15357. https://doi.org/10.1039/c2jm31413d.

(82) Kotobuki, M.; Kanamura, K.; Sato, Y.; Yoshida, T. Fabrication of All-Solid-State Lithium Battery with Lithium Metal Anode Using Al_2O_3-Added $Li_7La_3Zr_2O_{12}$ Solid Electrolyte. *J. Power Sources* **2011**, *196* (18), 7750–7754. https://doi.org/10.1016/j.jpowsour.2011.04.047.

(83) Raju, M. M.; Altayran, F.; Johnson, M.; Wang, D.; Zhang, Q. Crystal Structure and Preparation of $Li_7La_3Zr_2O_{12}$ (LLZO) Solid-State Electrolyte and Doping Impacts on the

Conductivity: An Overview. *Electrochem* **2021**, *2* (3), 390–414. https://doi.org/10.3390/electrochem2030026.

(84) Bernuy-Lopez, C.; Manalastas, W.; Lopez del Amo, J. M.; Aguadero, A.; Aguesse, F.; Kilner, J. A. Atmosphere Controlled Processing of Ga-Substituted Garnets for High Li-Ion Conductivity Ceramics. *Chem. Mater.* **2014**, *26* (12), 3610–3617. https://doi.org/10.1021/cm5008069.

(85) Delluva, A. A.; Dudoff, J.; Teeter, G.; Holewinski, A. Cathode Interface Compatibility of Amorphous $LiMn_2O_4$ (LMO) and $Li_7La_3Zr_2O_{12}$ (LLZO) Characterized with Thin-Film Solid State Electrochemical Cells. *ACS Appl. Mater. Interfaces* **2020**, acsami.0c03519. https://doi.org/10.1021/acsami.0c03519.

(86) Delluva, A. A.; Kulberg-Savercool, J.; Holewinski, A. Decomposition of Trace Li_2CO_3 During Charging Leads to Cathode Interface Degradation with the Solid Electrolyte LLZO. *Adv. Funct. Mater.* **2021**, *31* (34), 2103716. https://doi.org/10.1002/adfm.202103716.

(87) Bucci, G.; Swamy, T.; Chiang, Y.-M.; Carter, W. C. Modeling of Internal Mechanical Failure of All-Solid-State Batteries during Electrochemical Cycling, and Implications for Battery Design. *J. Mater. Chem. A* **2017**, *5* (36), 19422–19430. https://doi.org/10.1039/C7TA03199H.

(88) Han, F.; Yue, J.; Chen, C.; Zhao, N.; Fan, X.; Ma, Z.; Gao, T.; Wang, F.; Guo, X.; Wang, C. Interphase Engineering Enabled All-Ceramic Lithium Battery. *Joule* **2018**, *2* (3), 497–508. https://doi.org/10.1016/j.joule.2018.02.007.

(89) Falco, M.; Ferrari, S.; Appetecchi, G. B.; Gerbaldi, C. Managing Transport Properties in Composite Electrodes/Electrolytes for All-Solid-State Lithium-Based Batteries. *Mol. Syst. Des. Eng.* **2019**, *4* (4), 850–871. https://doi.org/10.1039/C9ME00050J.

(90) Thangadurai, V.; Weppner, W. $Li_6ALa_2Nb_2O_{12}$ (A=Ca, Sr, Ba): A New Class of Fast Lithium Ion Conductors with Garnet-Like Structure. *J. Am. Ceram. Soc.* **2005**, *88* (2), 411–418. https://doi.org/10.1111/j.1551-2916.2005.00060.x.

(91) Thangadurai, V.; Kaack, H.; Weppner, W. J. F. Novel Fast Lithium Ion Conduction in Garnet-Type $Li_5La_3M_2O_{12}$ (M = Nb, Ta). *J. Am. Ceram. Soc.* **2003**, *86* (3), 437–440. https://doi.org/10.1111/j.1151-2916.2003.tb03318.x.

(92) Bachman, J. C.; Muy, S.; Grimaud, A.; Chang, H.-H.; Pour, N.; Lux, S. F.; Paschos, O.; Maglia, F.; Lupart, S.; Lamp, P.; Giordano, L.; Shao-Horn, Y. Inorganic Solid-State Electrolytes for Lithium Batteries: Mechanisms and Properties Governing Ion Conduction. *Chem. Rev.* **2016**, *116* (1), 140–162. https://doi.org/10.1021/acs.chemrev.5b00563.

(93) Etacheri, V.; Marom, R.; Elazari, R.; Salitra, G.; Aurbach, D. Challenges in the Development of Advanced Li-Ion Batteries: A Review. *Energy Environ. Sci.* **2011**, *4* (9), 3243. https://doi.org/10.1039/c1ee01598b.

(94) Banerjee, A.; Wang, X.; Fang, C.; Wu, E. A.; Meng, Y. S. Interfaces and Interphases in All-Solid-State Batteries with Inorganic Solid Electrolytes. *Chem. Rev.* **2020**, *120* (14), 6878–6933. https://doi.org/10.1021/acs.chemrev.0c00101.

(95) Sakuda, A.; Hayashi, A.; Tatsumisago, M. Interfacial Observation between $LiCoO_2$ Electrode and $Li_2S–P_2S_5$ Solid Electrolytes of All-Solid-State Lithium Secondary Batteries Using Transmission Electron Microscopy †. *Chem. Mater.* **2010**, *22* (3), 949–956. https://doi.org/10.1021/cm901819c.

(96) Koerver, R.; Aygün, I.; Leichtweiß, T.; Dietrich, C.; Zhang, W.; Binder, J. O.; Hartmann, P.; Zeier, W. G.; Janek, J. Capacity Fade in Solid-State Batteries: Interphase Formation and Chemomechanical Processes in Nickel-Rich Layered Oxide Cathodes and Lithium Thiophosphate Solid Electrolytes. *Chem. Mater.* **2017**, *29* (13), 5574–5582. https://doi.org/10.1021/acs.chemmater.7b00931.

(97) Han, X.; Gong, Y.; Fu, K. (Kelvin); He, X.; Hitz, G. T.; Dai, J.; Pearse, A.; Liu, B.; Wang, H.; Rubloff, G.; Mo, Y.; Thangadurai, V.; Wachsman, E. D.; Hu, L. Negating Interfacial Impedance in Garnet-Based Solid-State Li Metal Batteries. *Nat. Mater.* **2017**, *16* (5), 572–579. https://doi.org/10.1038/nmat4821.

(98) Kim, K. J.; Rupp, J. L. M. All Ceramic Cathode Composite Design and Manufacturing towards Low Interfacial Resistance for Garnet-Based Solid-State Lithium Batteries. *Energy Environ. Sci.* **2020**, *13* (12), 4930–4945. https://doi.org/10.1039/D0EE02062A.

(99) Sastre, J.; Chen, X.; Aribia, A.; Tiwari, A. N.; Romanyuk, Y. E. Fast Charge Transfer across the $Li_7La_3Zr_2O_{12}$ Solid Electrolyte / $LiCoO_2$ Cathode Interface Enabled by an Interphase-Engineered All-Thin-Film Architecture. *ACS Appl. Mater. Interfaces* **2020**, acsami.0c09777. https://doi.org/10.1021/acsami.0c09777.

(100) Philipp, M.; Gadermaier, B.; Posch, P.; Hanzu, I.; Ganschow, S.; Meven, M.; Rettenwander, D.; Redhammer, G. J.; Wilkening, H. M. R. The Electronic Conductivity of Single Crystalline Ga-Stabilized Cubic $Li_7La_3Zr_2O_{12}$: A Technologically Relevant Parameter for All-Solid-State Batteries. *Adv. Mater. Interfaces* **2020**, *7* (16), 2000450. https://doi.org/10.1002/admi.202000450.

(101) Shannon, R. D. Revised Effective Ionic Radii and Systematic Studies of Interatomic Distances in Halides and Chalcogenides. *Acta Crystallogr. Sect. A* **1976**, *32* (5), 751–767. https://doi.org/10.1107/S0567739476001551.

(102) Rettenwander, D.; Welzl, A.; Cheng, L.; Fleig, J.; Musso, M.; Suard, E.; Doeff, M. M.; Redhammer, G. J.; Amthauer, G. Synthesis, Crystal Chemistry, and Electrochemical Properties of $Li_{7-2x}La_3Zr_{2-x}Mo_xO_{12}$ (x = 0.1–0.4): Stabilization of the Cubic Garnet Polymorph via Substitution of Zr^{4+} by Mo^{6+}. *Inorg. Chem.* **2015**, *54* (21), 10440–10449. https://doi.org/10.1021/acs.inorgchem.5b01895.

(103) Crank, J. *The Mathematics of Diffusion*, 2d ed.; Clarendon Press: Oxford, [Eng], 1975.

(104) Li, B.; Ge, J.; Zhang, B. Diffusion in Garnet: A Review. *Acta Geochim.* **2018**, *37* (1), 19–31. https://doi.org/10.1007/s11631-017-0187-x.

(105) Safi, I. Recent Aspects Concerning DC Reactive Magnetron Sputtering of Thin Films: A Review. *Surf. Coat. Technol.* **2000**, *127* (2–3), 203–218. https://doi.org/10.1016/S0257-8972(00)00566-1.

(106)   Kelly, P. J.; Arnell, R. D. Magnetron Sputtering: A Review of Recent Developments and Applications. *Vacuum* **2000**, *56* (3), 159–172. https://doi.org/10.1016/S0042-207X(99)00189-X.

(107)   Sarakinos, K.; Alami, J.; Konstantinidis, S. High Power Pulsed Magnetron Sputtering: A Review on Scientific and Engineering State of the Art. *Surf. Coat. Technol.* **2010**, *204* (11), 1661–1684. https://doi.org/10.1016/j.surfcoat.2009.11.013.

(108)   Gudmundsson, J. T. Physics and Technology of Magnetron Sputtering Discharges. *Plasma Sources Sci. Technol.* **2020**, *29* (11), 113001. https://doi.org/10.1088/1361-6595/abb7bd.

(109)   Berg, S.; Nyberg, T. Fundamental Understanding and Modeling of Reactive Sputtering Processes. *Thin Solid Films* **2005**, *476* (2), 215–230. https://doi.org/10.1016/j.tsf.2004.10.051.

(110)   Musil, J.; Baroch, P.; Vlček, J.; Nam, K. H.; Han, J. G. Reactive Magnetron Sputtering of Thin Films: Present Status and Trends. *Thin Solid Films* **2005**, *475* (1–2), 208–218. https://doi.org/10.1016/j.tsf.2004.07.041.

(111)   Sproul, W. D.; Christie, D. J.; Carter, D. C. Control of Reactive Sputtering Processes. *Thin Solid Films* **2005**, *491* (1–2), 1–17. https://doi.org/10.1016/j.tsf.2005.05.022.

List of Figures

Joseph Ring

List of Tables

Acknowledgements

First of all, I want to express me sincerest gratitude to Prof. Jürgen Fleig, who gave me the opportunity to work in his wonderful group. Beyond his invaluable guidance he gave me the freedom to explore and grow in my own way, not only as a researcher but also as a person. Furthermore, I want to thank him for the stimulating work atmosphere and the opportunity to attend the SSI-conference in the summer of 2022. With grateful appreciation, I want to acknowledge the help of Dr. Andreas Nenning, who reviewed my work tirelessly and spent countless hours on improving it. He made our endless discussions both educating and enjoyable. I also want to thank him for his ongoing effort on the publication of my works as a corresponding author.

I want to thank Dr. Tobias Huber, who shared so much of his vast knowledge on building special research equipment and gave me valuable practical experience. For the measurement and interpretation of SIMS data, I want to thank Dr. Markus Kubicek, who spent many hours to help my research. I want to thank Dr. Thomas Schachinger for his much appreciated theoretical and practical help on various TEM techniques. The contributions of Dr. Sergey Volkov and Dr. Vedran Vonk from DESY is also gratefully acknowledged.

Special thanks go out to my coworker Andreas Bumberger for being my companion on the long and sometimes bumpy road of Li-ion battery research. Many of our shared goals could not have been reached if not for his tireless effort and dedication. Further, I want to thank him for the cumbersome preparation of TEM samples. The work of our students, Nicole Rosza, Florian Kubik and Matthias Kogler is also gratefully acknowledged. I want to thank the entire working group for the welcoming work environment and joyful time. The fun and laughter we shared mean just as much to me as the many fruitful scientific discussions and will forever be remembered.

I want to thank my dear parents, for giving me all the strength and support for making all this possible. The valuable moral help of my friends and family is also much appreciated. Finally I want to express me deepest gratitude to Katharina, my most beloved star, who gave me light in dark places, when all other lights went out.